Astronomy & Astrophysics (Caucasus) 4, (2018)

ON DETERMINING SOME FEATURES OF SOLAR QUIESCENT PROMINENCES

A.G. Nikoghossian

Byurakan Astrophysical Observatory, Aragatsotn region, 378433, Armenia

E-mail: nikoghoss@yahoo.com

Abstract

The report is a brief overview of results obtained by the author with his collaborators in the theory of spectral line formation in atmospheres with a complex fine structure. The immediate motivation of the research work was due to interpretation of the EUV spectrum of solar quiescent prominences observed with SUMER spectrograph as a part of the SOHO space program. The report consists of two parts. The first briefly describes the methods proposed for solving the line-radiation transfer problems in multicomponent atmospheres with appropriate analytical and numerical solutions. We show that even in the simplest static model case of the radiating medium composed of physically different types of elements, the observed line profiles may differ drastically from those obtained for the medium with preliminarily averaged properties. Further, the more realistic and complicated situations of multicomponent atmosphere with randomly varying properties are considered with a particular attention to the effect of the velocity field. An important role of the relative mean square deviation {RelMSD} of the observed line intensities in the diagnostics of physical features of spatial and temporal variations of prominences is demonstrated. The second part of the report concerns the generalization of the classical method of determining the velocities of microturbulent motions in solar prominences to take account of the opacity of spectral lines. It allows estimating, along with microturbulent velocities, the opacity of the line radiating volumes and the kinetic temperature.

Keywords: ***solar prominences: formation of spectral lines: microturbulent velocity***

1. Introduction

The need to create a theory of radiative transfer in media with complicated fine structure subject to random variations has long been felt. As early as in the 1970's (Cram 1972) there was demonstrated that the observed profiles of chromospheric lines of ionized calcium cannot be explained in terms of the theory developed for homogeneous stationary media. The similar problems we evidently meet in interpreting other non-stationary phenomena in the solar atmosphere, such as chromospheric spicules, coronal streams, and polar plums. Problems involving the propagation of radiation in randomly inhomogeneous media appear also in other branches of astrophysics. Examples include the scattering of light on molecular clouds in the interstellar medium (Juvela 1997, Juvela and Padovan 2003) and the stochastic attenuation of galactic radiation as it travels over cosmologic distances (Madau 1995).

The calculation procedure of statistical properties of the radiation emerging from multicomponent LTE-atmosphere was presented by Lindsey (1987) and Jefferies and Lindsey (1988) for the interpretation of total solar eclipse observations in the far-infrared. These authors derived relations describing the evolution behavior of the mean value of the intensity and its variance along the radiation path.

The theory we developed for interpreting the observable emergence of complex structural pattern of media in the line spectrum may be regarded as a further generalization of the Ambartsumian layers adding method. The theory is simpler for the atmosphere in LTE: because of the absence of scattering, and hence the reflection from structural elements, the mean value of intensity emerging from any part of the multicomponent atmosphere remains unaltered when new components are added. This fact is essential in the sense that it simplifies the problem and allows establishing the recurrence relationship for both the mean intensity and variance so that the problem admits a simple closed-form solution. These results for the LTE atmospheres were generalized by Nikoghossian and co-authors (1997,1998), which makes it possible to reveal quantitative as well as qualitative discrepancies of the line intensities with respect to those formed in a homogeneous atmosphere with preliminarily averaged random characteristics. The further development of the theory given by Nikoghossian, Pojoga and Mouradian (1997) and Nikoghossian, Mouradian (2000) allowed one to formulate and solve the problem of spectral line-radiation also in the NLTE composite atmospheres.

On the other hand, one should take into account that the plasma in the prominences is known to participate in various kinds of motions what, of course, affect the observed spectral line profiles. Random thermal and turbulent motions in prominences with velocities of the order of 5-

10 km/s are superimposed on ascending (eruption) or descending (mass loss owing to its return to the chromosphere and photosphere) flows and large-scale hydrodynamic motions (Tandberg-Hanssen 1995). The radiative transfer in a line through a dynamically active medium of this sort leads to a great variety of line shapes which are distorted by the Doppler effect. Furthermore, the line profiles depend on a number of other parameters characterizing the emitting volume, so that quantitative interpretation of the observed spectra is a rather complicated problem in general. This more realistic problem making allowance for the dynamics of a radiating multicomponent medium was considered by Nikoghossian (2007). An important role in all the mentioned model problems belongs to the frequency-dependent relative mean square deviations (RelMSD) of the observed line intensities due to spatial and/or temporal variation of the number or physical properties and non-thermal motions of the fine structural elements. As it was shown, there is a well pronounced relationship between functional form of the RelMSD within a spectral line and the sources of the observed line intensity spatial/temporal fluctuations, so that the RelMSD can be regarded as an alternative powerful tool in interpreting the physical nature of processes occurring in the radiating medium. Note that our direct motivation of the developed theory was the interpretation of the rich observational material gained in frameworks of the Skylab and SOHO space missions for the EUV spectrum of prominences.

The final part of the report describes the method of evaluating the velocities of microturbulent motions in solar quiescent prominences which generalize the classical method taking into account the difference in opacities of the line radiating volumes. The method is applied to EUV observational data obtained with the SUMER spectrometer in the SOHO program. The estimated values of microturbulent velocities, opacities and kinetic temperature are in agreement with those obtained by other ways.

2. Lines profiles in stochastic multicomponent media

We start with treating the simplest model of the static LTE multicomponent medium composed of a certain number of structural elements of two sorts, each of which is characterized by its optical thickness τ_i, the power of the contained energy sources B_i and the probability p_i of appearance (i=1,2). The dependence on frequency within the spectral line is described by the Lorentsian profile of the absorption coefficient $a(x) = \exp(-x^2)$. We are interested in the statistical mean value of the observed intensity $\langle I(x) \rangle$, as well as the variation of the RelMSD in frequency

$\delta_n(x)$ within a spectral line, where N denotes the number of structural elements. The closed form analytical expressions for the mentioned quantities were obtained by Nikoghossian et al. (1999):

$$\langle I_N(x)\rangle = L_N(x)\langle I_1(x)\rangle,\ \delta_N(x) = \frac{M_N(x)}{L_N(x)}[1+\delta_1(x)] + 2\frac{K(x)A_N(x)}{< I_1(x) > L_N^2(x)} - 1,$$

where the following notations are introduced

$$L_N(x) = \frac{1-q^N(x)}{1-q(x)},\ M_N(x) = \frac{1-\beta^N(x)}{1-\beta(x)},\ A_N(x) = \frac{L_N(x)-M_N(x)}{q(x)-\beta(x)},$$

$$K(x) = < J_i(x)\exp[-\alpha(x)\tau_i] > .\ q(x) = < \exp[-\alpha(x)\tau_i] >,\ \beta(x) = < \exp[-2\alpha(x)\tau_i],$$

$$J_i(x) = B_i\alpha(x)\{1-\exp[-\alpha(x)\tau_i]\},\ (i=1,2)$$

According to definition, we have

$$< I_1(x) > = \sum_{i=1}^{2} p_i J_i(x),\ \delta_1(x) = \frac{1}{2 < I_1(x) >^2}\sum_{i=1}^{2} p_i \sum_{k=1}^{2} p_k \left[J_i(x) - J_k(x)\right]^2.$$

We see that for any number of components N, the degree of fluctuations is determined by four parameters q, β, δ_1 and $K/<I_1>$ (or by three parameters, when $p_1=p_2=1/2$), which are statistical characteristics of the emission and absorption of a single element of the medium.

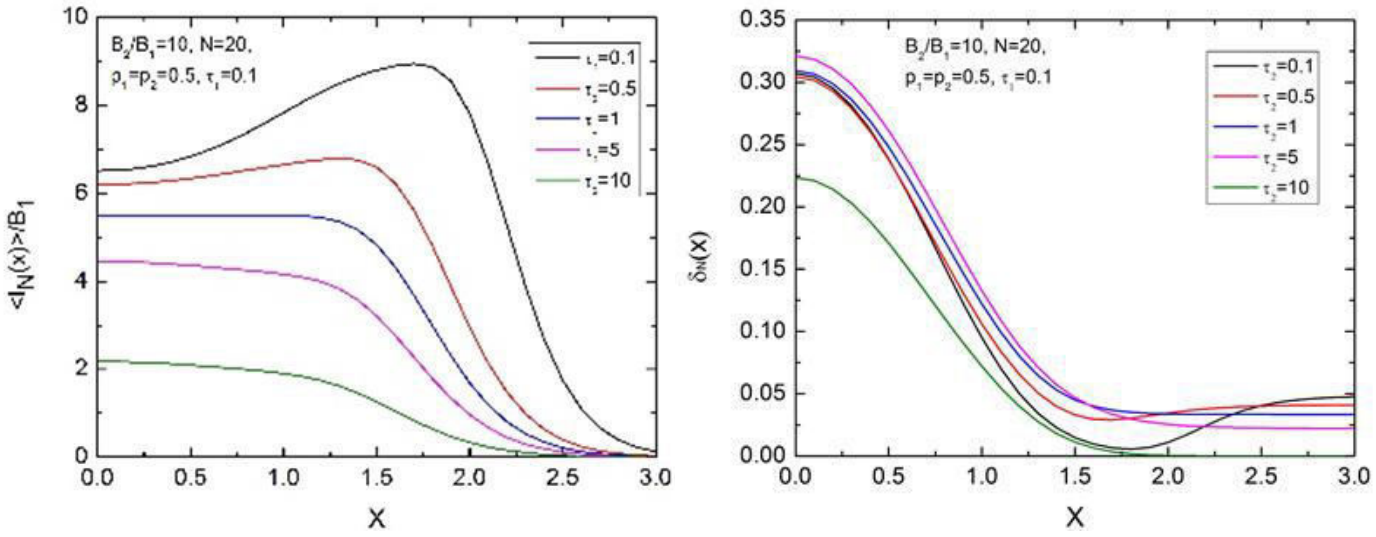

Fig.1 The statistical mean of the emitting intensities (left panel) and RelMSD (right panel) for different values of parameters. Here, a particlar attention is paid to the cases of different combinations of optical thicknesses of elements.

Fig.1 illustrates profiles of spectral lines and proper RelMSD when the number of structural elements is 20. In this model case, the elements differ each from other in the power of the internal energy sources. The opacities are choosen on the ground that hotter components must mainly be more opaque. The first effect that attracts attention is the double-peaked profile formed preferably when the difference between components is predominatly due to the value of the sources of internal energy. Note that such profiles are usually associated with the lines formed in a NLTE atmosphere as a result of the frequency redistribution. Now we see that multicomponent media may generate double-peaked profiles even in the abscense of radiation scattering. Another result concerns the frequency behaviour of the RelMSD in the wings of the line. We see that its value can either decrease or increase dependent on values of other parameters. A clear idea on this point can be obtained from Fig.2 below drawn for the NLTE atmosphere.

A further progress in the theory allowed to handle more general and complex models with greater sorts of components and greater number of possible realizations. More realistic models consider the correlations between realizations of different parameters in two adjacent components. The theory becomes much more complicated in the case of NLTE atmospheres (see Nikoghossian et al. (1999), Nikogossian and Mouradian (2000), Nikoghossian (2002). The most important conclusion is that the aforementioned features of RelMSD remain qualitatively valid in the NLTE media. Fig.2 shows the variation of the frequency-dependent RelMSD of the observing intensities in two mutually opposite situations of equal opacities $\tau_1 = \tau_2$ and $B_1 \neq B_2$ and the opposite case of different opacities and equal B_i.

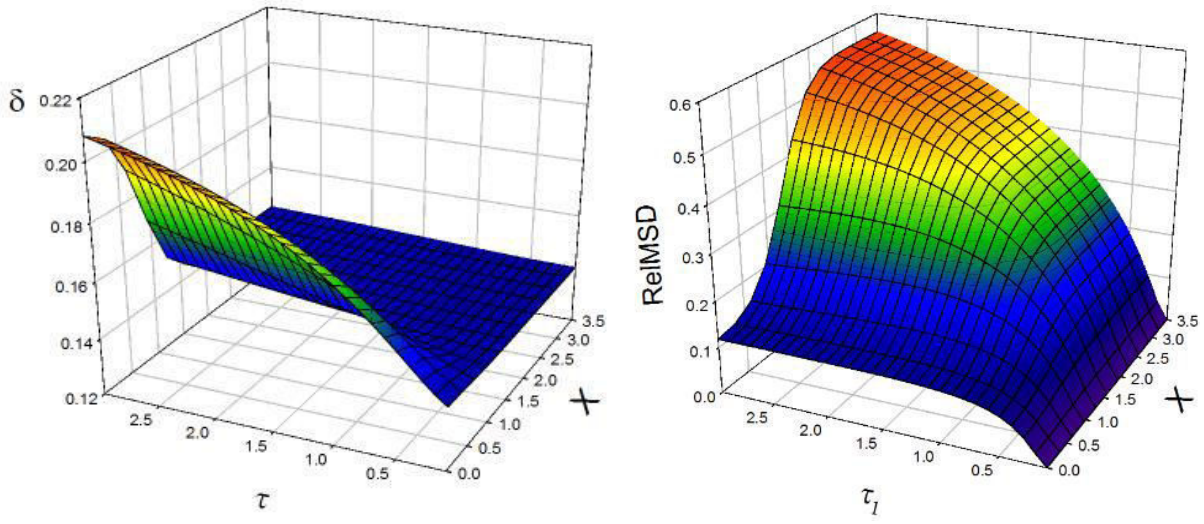

Fig.2. The RelMSD of intensity fluctuations in two models of the NLTE atmosphere. The calculations are done for $\lambda = 0.99$, where λ is the photon re-radiation coefficient in the multiple

scattering process. For simplicity's sake, the number of components are taken $N = 4$ and $p_1 = p_2$. The values of other parameters are $S = B_2 / B_1 = 7$, $\tau_1 = \tau_2 = \tau$ (left panel) and $S = 1$, $\tau_2 = 0.1$ (right panel).

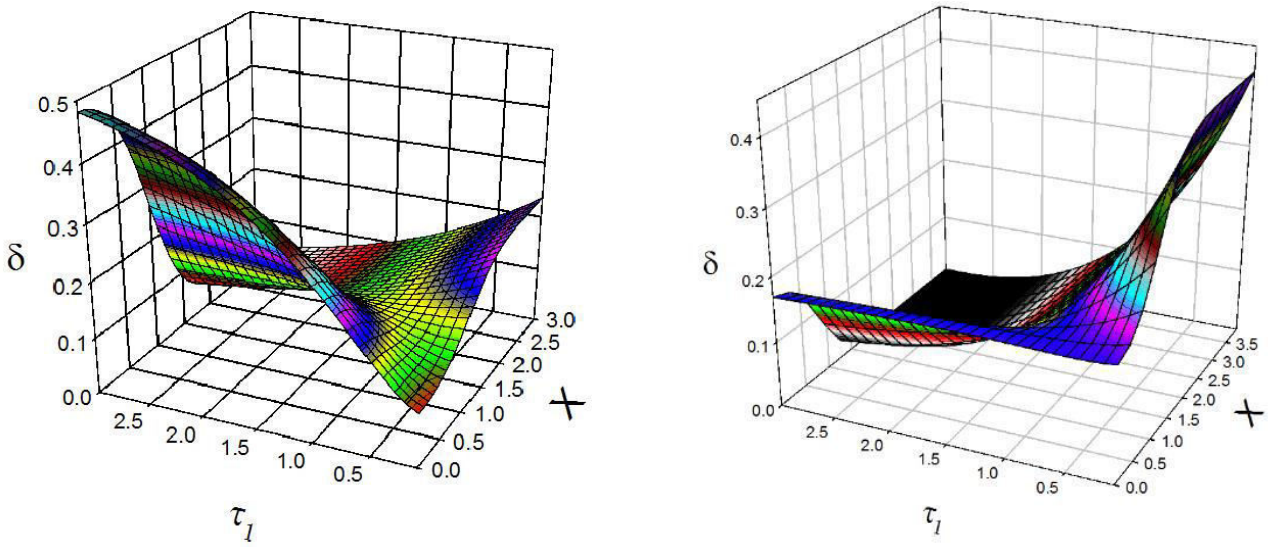

Fig.3. The RelMSD of intensity fluctuations in two models of the NLTE atmosphere for $N = 4$, $p_1 = p_2 = 1/2$, $S = B_2 / B_1 = 7$, $\tau_2 = 1$ and $\lambda = 0$ (LTE, left panel), $\lambda = 0,99$ (NLTE, right panel).

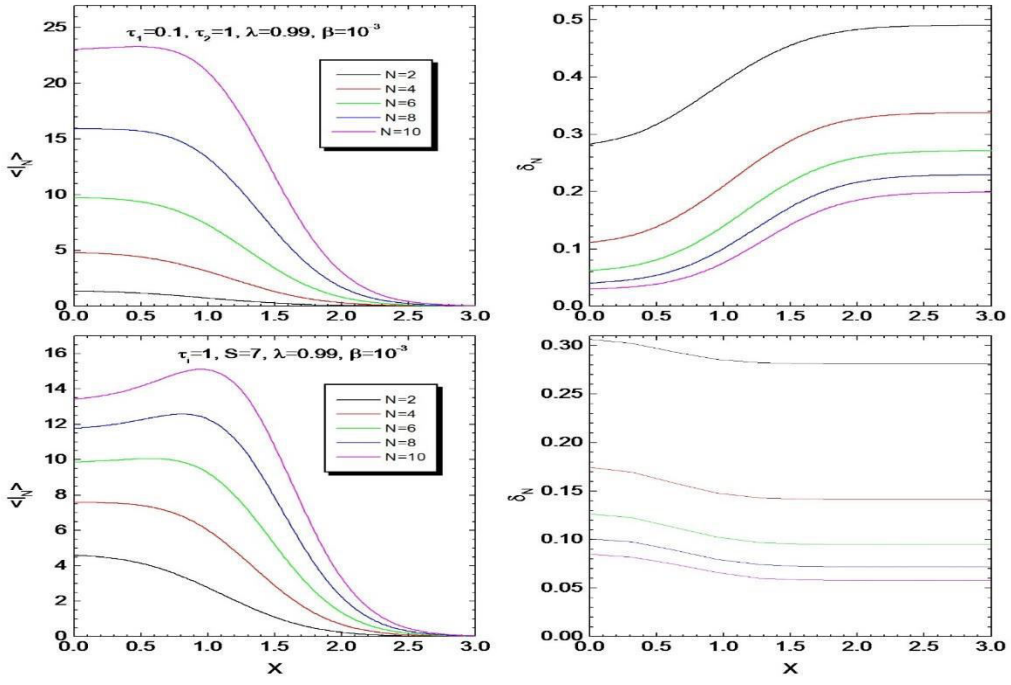

Fig.4. Dependence of averaged intensities radiating in a line and the proper RelMSD

on the number N of structural elements for indicated values of realized opacities, the power of internal energy sources and other parameters describing the elementary event of scattering (here β is the ratio of the absorption coefficient in continuum to that in the centre of the line).

Dependence of the RelMSD variation within a spectral line on multiple scattering is shown in Fig.3. We see that the center-to-wing behavior of this quantity in both cases qualitatively is the same. Besides, as would be expected, the difference between RelMSD in discussed two regimes of the line formation are more pronounced for greater values of optical thicknesses. Fig.4. illustrates the variation of averaged values of dimensionless intensities and proper RelMSD in frequency within a line. As might be expected, with increasing number of components, the values of RelMSD decrease over entire frequency range. As above, the behavior of the RelMSD in the far wings of the line in these two model cases is diametrically different. In a more general situation when the optical thickness in the line and the power of the energy sources take arbitrary non-equal values, the variation of the RelMSD towards the wings of a line becomes more complex (see Nikoghossian 2002, 2005). However, the obtained results remain valid if we admit that the opaque lines are formed in the hotter radiating volumes, which is often the case. Referring the reader to the mentioned works for details of this inference, we note that this is very important from the point of view of interpretation of the nature of the surface brightness fluctuations of any extended astronomical object with a randomly varying fine structure. Thus, this means that the variation of the RelMSD may be regarded as a diagnostic tool in revealing the physical state of the studied line radiating medium.

3. Lines profiles in a dynamically active multicomponent media

In the real stochastic atmospheres of astrophysical interest the velocity field is subject to random variations together with physical and geometrical characteristics of the medium. It is evident that such kind of velocity variations may strongly affect the observed line profiles.

Radiative transfer in a line through dynamically active medium results in a great variety of line shapes which are distorted by the Doppler effect. Furthermore, the line profiles depend on a number of other parameters characterizing the emitting volume, so that a quantitative interpretation of the observed spectra is a rather complicated problem in general. The problem of the spectral line formation in a stochastic multicomponent atmosphere in LTE was treated by Nikoghossian (2007). Motions considered in this paper imitate the large scale hydrodynamic motions usually observed in solar prominences. The effect of radiation on the velocity field is

neglected which is reasonable for the lines with low optical thickness. We considered a problem of determining the radiation emerging from a dynamically active atmosphere consisting of *N* structural elements whose physical characteristics are subject to random variations. It is assumed that the spatial process of realizing the components of a given type is Markovian, i.e., the realization of the physical properties of a given component depends only on the realization of these properties of the preceding component. Particular attention we pay to determination of the RelMSD of the observed line-radiation. The important feature of the method we propose is that in order to determine the mean intensity of the line radiation emerging from the atmosphere, $\langle I_N(x)\rangle$, one preliminarily find the auxiliary quantities $\langle I_N^{(i)}(x)\rangle$ characterizing the mean mathematical expectation of the intensity of the observed radiation provided that the *N*-th element belongs to the *i*-th type, so that

$$\langle I_N(x)\rangle = \frac{1}{n}\sum_{i=1}^{n}\langle I_N^{(i)}(x)\rangle .$$

In the case of Markov process $\langle I_N^{(i)}(x)\rangle$ are determined from recurrence relations

$$\langle I_N^{(i)}(x)\rangle = \sum_{k=1}^{n} q_{ik}\left[\langle I_N^{(i)}(x)\rangle \exp\left(-z^{(i)}\tau_i\right) + P_{N-1}^{k} J_i(x)\right],$$

where the following notations are introduced: the coefficients q_{ik} are elements of the Markov transition matrix, $z^{(i)} = \alpha\left(x-u^i\right)+\beta$ and $J_i(x) = B_i\left[1-\exp\left(-z^{(i)}\tau_i\right)\right]$. Further, $u^i = V_{hyd}^i / V_{th}$, where V_{th} is the mean thermal velocity and V_{hyd} is the line-of-sight component of hydrodynamic velocity.

Fig.5 shows typical examples of profiles and RelMSD calculated for purely stochastic case, when the atmosphere consists of only two types of structural elements. In addition to the profile of the average radiation intensity, $\langle I\rangle$, emerging from the medium, we present two other profiles $\langle I_1\rangle$ and $\langle I_2\rangle$ calculated given that the *N*-th element belongs, respectively, to the first and second types. To make the changes in the RelMSD clearer, *N* has been chosen to be comparatively small. In order to clarify the effect of the Markovian interaction between the components on the observed profiles and relative mean square deviations, we considered the case of a so-called doubly stochastic atmosphere. The profiles depicted in the right panel show

essential distortion of the line profiles caused by hydrodynamic motions. Another important result is that the distinctive feature of the RelMSD of the radiation in a line formed in a dynamically active stochastic atmosphere is local "spikes" (maxima) in the wings of the line. The theoretical results in this paper are compared with spectral observations of quiescent solar prominences obtained in the framework of the SOHO space mission.

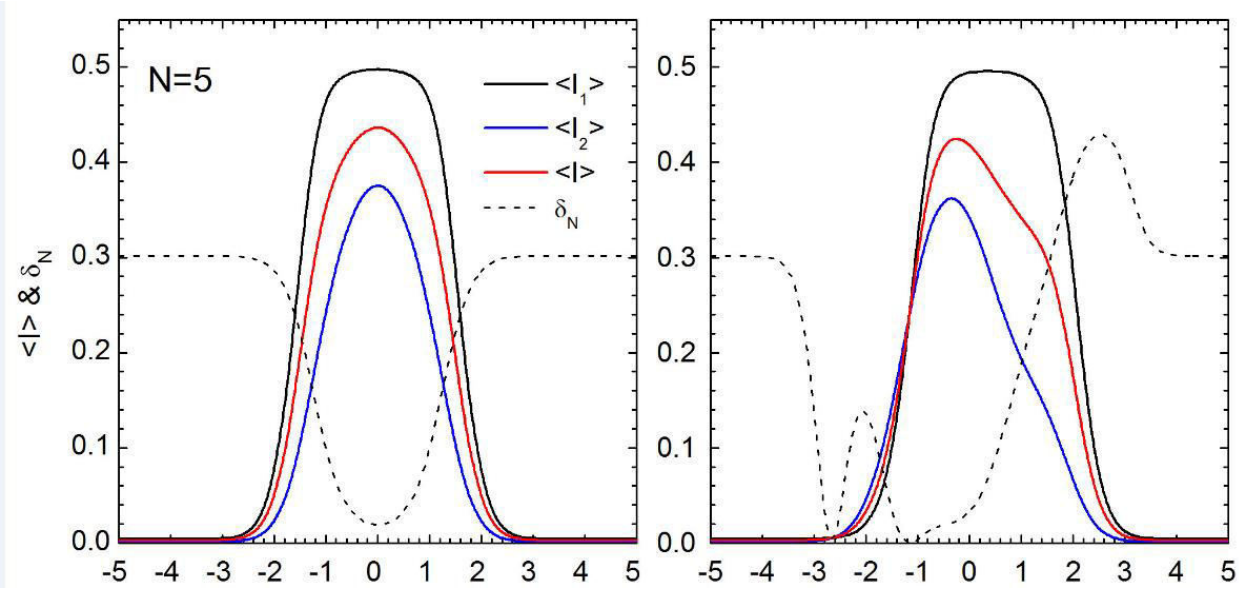

Fig.5. Theoretical profiles of a spectral line and the RelMSD for double stochastic static (left) and dynamically active (right) atmospheres. It is assumed that the latter consists of two types of structural elements with the following parameters: $B_1 = B_2 = 1$, $p_1 = p_2 = 0.5$, $\tau_1 = 2$, $\tau_2 = 0.2$, $\beta = 10^{-3}$, $u^{(1)} = 0.5$, $u^{(2)} = -0.5$, and $q_{11} = q_{22} = 0.9$, $q_{12} = q_{21} = 0.1$.

4. Observational data

In order to verify the theoretical results, we have used some observational data on spectral lines of solar quiescent prominences in the EUV domain of the spectrum obtained on August 10, 1999 using the SUMER spectrometer. We were interested in the fluctuations in the surface brightness of the prominences in several of strongest lines. With each observation, the spectrometer slit with its field of 1"×120" yields 120 line profiles so that their variation along the slit can be followed. These data are usually sufficient for determining the statistical averages of the radiation intensity and the corresponding RelMSD as functions of frequency within a line.

Fig.6 shows data on the relative mean intensity and RelMSD (broken curves) for several relatively strong EUV lines. We pointed out above that the RelMSD increasing to the line wings,

indicates the fact that the fluctuations in the surface brightness of the prominence are caused mainly by changes in optical thicknesses. We see also that the central depression in the frequency profile of the RelMSD is different for different lines and is correlated with the effective temperature at which they are formed. The "spikes" (local maxima) in the wings of the lines predicted by the above theory for non-thermal (hydrodynamic) motions are distinctly seen. One can also see that for lines with a high effective formation temperature (i.e., the lines formed primarily in the surrounding corona), such as OVI λλ1032 Å, λλ1037 Å, and NV λλ1242 Å, the magnitude of these spikes appears to be smaller than for the lines formed entirely within the prominence. The appearance of isolated single spikes is an indication that the velocities of the non-thermal motions are only slightly greater than the thermal speed, if they exceed it at all. We shall see in the next section that the observed lines profiles and proper RelMSD can be used to determine the relative contribution of turbulent motions, as well as the optical thickness of the radiating volume.

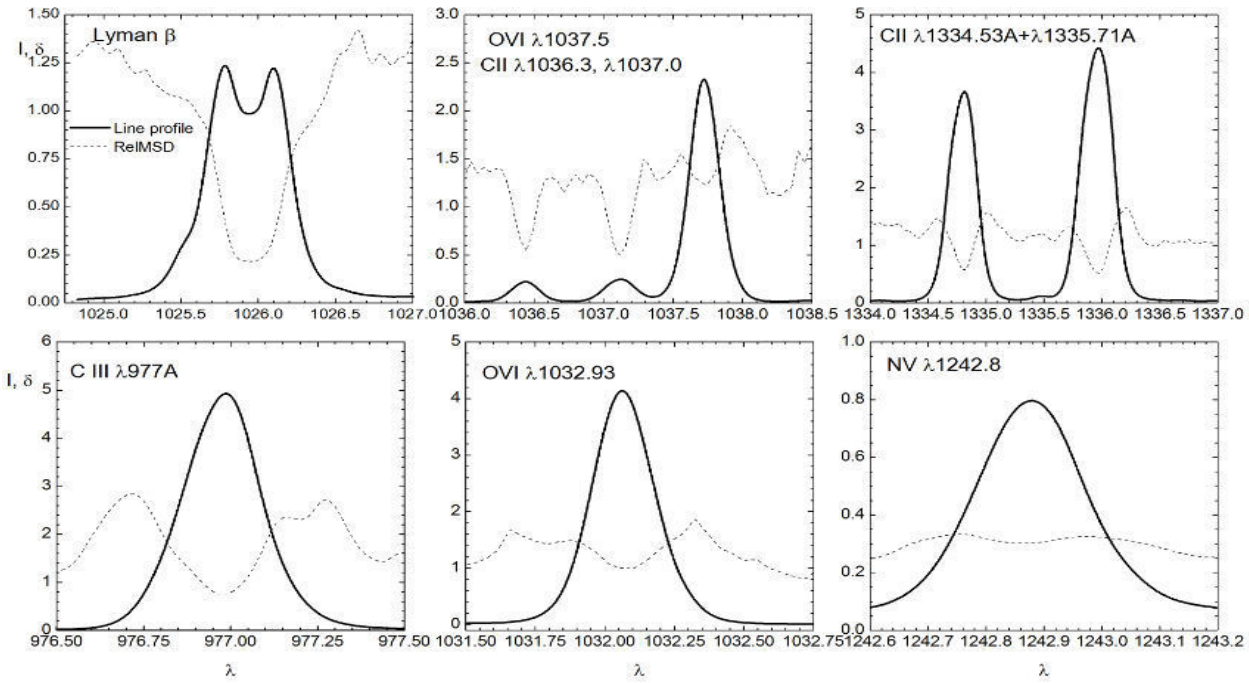

Fig.6. Statistical mean profiles (smooth curves) and the corresponding RelMSD (dotted curves) for a series of relatively strong EUV lines of a solar prominence observed on August 10, 1999, as part of the SOHO space mission.

5. Determination of microturbulent velocities and kinetic temperature of prominences

Microturbulent velocities of prominences are usually determined using optically thin lines (Tabdberg-Hanssen 1995) with profiles that can, with some degree of accuracy or other, be replaced by the profile of the absorption coefficient $\alpha(x)$. With Doppler broadening of the line,

$$\alpha(x) = \exp(-x^2). \tag{1}$$

The velocities of microturbulent motions are independent at an atomic level and line broadening is similar to that caused by thermal motions. In this case, we have

$$\Delta\nu_D = \frac{\nu_0}{c}\sqrt{V_{th}^2 + \xi_t^2}, \tag{2}$$

where ξ_t is the average velocity of microturbulent velocities. It is assumed that $I(x)/I(0) = \alpha(x)$ and, given Eq.(2), it is used to determine ξ_t. Since the kinetic temperature, which is determined by the average thermal speed, is previously unknown, one examines a pair of spectral lines belonging to different ions, but formed in roughly the same volume of the prominence. This makes it possible to find, separately, both ξ_t and the kinetic temperature of the plasma in a prominence, as well as the thermal and microturbulent velocities. This approach has a obvious deficiency due to that the profile of a spectral line can be replaced by a profile of the absorption coefficient only in the limiting case where the optical thickness τ_0 of the emitting volume is zero. Meanwhile, for many intense EUV lines this assumption may be rather crude, since information on the structure and optical thickness of the medium is lost. Errors of another sort may arise if only a Doppler profile is considered or the influence of continuum absorption is neglected.

At the same time, if we are examining a medium of optical thickness τ_0 with developed homogeneous turbulence, then, assuming that the source function *B* does not vary with depth, for the average intensity of the observed radiation we can write

$$I(\tau_0, x) = B\left[1 - \mathrm{e}^{-\alpha(x)\tau_0}\right]. \tag{3}$$

In this formula the effect of continuum absorption is neglected; this will be discussed below. It should also be noted that the use of Eq.(3) is not generally obvious in advance. In fact, it is valid when the dominant mechanism for formation of the spectral line is true absorption and emission. In other words, the role of multiple scattering at the frequencies of the line is neglected; this is obviously justified for many EUV spectral lines in prominences, except for the first members of the hydrogen Lyman series, for which the optical thickness of the medium is large. It is evident that this formula contains information on the radiating medium, so it is less crude than the above limiting case of an optically thin medium. We shall use this particular formula, even though the approach developed here can, in principle, be employed to examine more realistic models.

The main directly measured characteristics of a line that are of interest to us are $\Delta\lambda_{1/2}$ its full-width half-maximum and its integrated intensity in units of the intensity at the line center, $J_\lambda(\tau_0)$. For convenience, besides them we shall also use the analogous, but dimensionless, quantities $x_{1/2}$ and $W(\tau_0)$. The latter is defined by

$$W(\tau_0)=\frac{1}{1-e^{-\alpha(0)\tau_0}}\int_{-\infty}^{\infty}\left[1-e^{-\alpha(x)\tau_0}\right]dx. \tag{4}$$

These two pairs of quantities are evidently related by the formulas

$$\Delta\lambda_{1/2}=\frac{\lambda_0}{c}\sqrt{V_{th}^2+\xi_t^2}\,x_{1/2}(\tau_0),\quad J_\lambda(\tau_0)=\frac{\lambda_0}{c}\sqrt{V_{th}^2+\xi_t^2}\,W(\tau_0). \tag{5}$$

Thus, compared to the classical approach, an additional characteristic of a spectral line, $J_\lambda(\tau_0)$, is introduced. This makes it possible to employ an idea, analogous to that which lies at the basis of the ordinary approach, for additionally estimating the optical thickness of the medium in the line. In fact, observational knowledge of the pair $\Delta\lambda_{1/2}$ and $J_\lambda(\tau_0)$ for lines from two different ions originating in roughly the same region of a prominence offers the possibility, in principle, of determining the optical thickness $\tau_0^{(1)}$ and $\tau_0^{(2)}$ for these lines, as well as T and ξ_t. Note that, in the classical method based on replacing the profile of a spectral line with a profile of the absorption coefficient, $x_{1/2}=\sqrt{\ln 2}$ and $W=\sqrt{\pi}$. In the case we are examining, Eq. (3) yields

$$x_{1/2}(\tau_0)=\left[-\ln\left(-\frac{1}{\tau_0}\ln\frac{1+e^{-\tau_0}}{2}\right)\right]^{1/2}, \qquad (6)$$

while $W(\tau_0)$ is given by Eq. (4).

It is important to note that the ratio $J_\lambda(\tau_0)/\Delta\lambda_{1/2}(\tau_0)=W(\tau_0)/x_{1/2}(\tau_0)$ does not depend on either the kinetic temperature *T* or the turbulent velocity ξ_t. As we shall see below, it weakly depends on the fraction of absorption in the continuum. Thus, this formula can serve as a fairly good indicator of the optical thickness of the prominence emitting in a given spectral line. Numerical calculations show that over a quite wide range of variation in τ_0 from 0 to 2.5 the functions $x_{1/2}(\tau_0)$ and $W(\tau_0)$ can be approximated as follows:

$$x_{1/2}(x)=0.142\tau_0+0.838, \quad W(\tau_0)=0.251\tau_0+1.778. \qquad (7)$$

The errors resulting from the use of Eq.(5) are less than 0.1%. The free terms in Eqs.(7) correspond to the classical values $\sqrt{\ln 2}$ and $\sqrt{\pi}$ for $\tau_0=0$. The ratio $J_\lambda(\tau_0)/\Delta\lambda_{1/2}(\tau_0)=W(\tau_0)/x_{1/2}(\tau_0)$ is of greatest interest, as noted above; within the range of values of τ_0 we have chosen, this ratio can be approximated with high accuracy (<0.1%) by the second degree polynomial

$$W(\tau_0)/x_{1/2}(\tau_0)=2.1284-0.0761\tau_0+0.0134\tau_0^2. \qquad (8)$$

It follows from this formula that for the spectral line formation mechanism being examined here, the values of $J_\lambda(\tau_0)/\Delta\lambda_{1/2}(\tau_0)$ within this range of variation in τ_0 must be within the narrow interval 2.021-2.129. Nevertheless, some of the measured values of this ratio may in fact be somewhat higher than the upper limit of this interval. Thus, it is necessary to study the influence of various effects on the final result. For example, in Eq.(3), it is easy to account for the effects associated with absorption in the continuum. An alternative refinement is subject to replacement of the Doppler profile of absorption coefficient by the Voigt profile. The final approximate results, according to those by Nikoghossian (2010) are

$$x_{1/2}(\tau_0)=-0.0077\tau_0^2+0.1623\tau_0+0.8347, \qquad (9)$$

$$W(\tau_0)=-0.0079\tau_0^2+0.2738\tau_0+1.7877, \qquad (10)$$

$$W(\tau_0)/x_{1/2}(\tau_0) = -0.0034\tau_0^3 + 0.0349\tau_0 - 0.1104 + 2.1513\,. \qquad (11)$$

After the optical thickness of the medium is found in one or another line, one can use arguments analogous to those employed in the conventional method to determine the kinetic temperature and the microturbulent velocities. This means that, if the optical thicknesses have been found for two lines $\left(\tau_0^{(i)}, i = 1,2\right)$ belonging to different ions and presumably formed in roughly the same region of a prominence, then the theoretical relations (10) and (11) can be used to find $x_{1/2}^{(i)}$ and $W^{(i)}$. Knowledge of one of these for two lines means, in principle, that we can find the kinetic temperature of the radiating volume, along with the thermal and microturbulent velocities in it, i.e.

$$T = \frac{m_{\mathrm{H}}c^2}{2k}\left[\left(\frac{\Delta\lambda_{1/2}^{(1)}}{x_{1/2}^{(1)}\lambda_0^{(1)}}\right)^2 - \left(\frac{\Delta\lambda_{1/2}^{(2)}}{x_{1/2}^{(2)}\lambda_0^{(2)}}\right)^2\right] \Big/ \left(\frac{1}{\mu_1} - \frac{1}{\mu_2}\right), \qquad (12)$$

$$\xi_t = \left[\left(\frac{c\Delta\lambda_{1/2}^{(1)}}{x_{1/2}^{(1)}\lambda_0^{(1)}}\right)^2 - \frac{2kT}{m_{\mathrm{H}}\mu_1}\right]^{1/2}, \qquad (13)$$

where μ_i is the molecular masses of ions and m_{H} is the mass of the hydrogen atom. Eq.(13) differs from the standard formula (see Tandberg-Hanssen 1995) in having $x_{1/2}^{(i)}$ in the denominators of these expressions. As shown above, $x_{1/2}(\tau_0)$ is an increasing function. Then, it is easy to infer that the kinetic temperatures given by the classical formula must be higher than the actual values.

We have used observations of EUV lines made on October 8, 1999, by the SUMER spectrometer. Some of these data are listed along with our results in Table 1. The required line profiles were constructed by averaging data over 120 pixels covering the slit of the spectrograph for a fixed interval of wavelengths. Data from pixels that contained no information on the prominence were, however, eliminated. The best known and brightest lines were mostly chosen. In the case of comparatively weak lines, the absence of blends was of special interest.

TABLE 1. EUV Lines used in this paper and the results obtained from them

Ëèíèè (Δ)	$\log T_m$	μ	$\Delta\lambda_{1/2}$	$J_\lambda(\tau_0)$	$W/x_{1/2}$	τ_0	$x_{1/2}$	ξ_t
OI 935.193	<4.0	15.999	0.0794	0.1683	2.1185	0.132	0.8560	29.75
SI 1235.624	<4.0	32.06	0.0807	0.1714	2.1243	0.054	0.8434	23.21
SII 996.0	4.5	32.06	0.0849	0.1808	2.1345	0.160	0.8605	29.67
CII 1334.53	4.5	12.01	0.1325	0.2823	2.1338	0.167	0.8616	34.49
CII 1335.71	4.5	12.01	0.1512	0.3196	2.1226	0.284	0.8801	38.51
SIII 1077.13	4.7	32.06	0.0939	0.1998	2.1282	0.224	0.8706	29.98
NII 1089.99	4.7	14.007	0.0976	0.2061	2.1138	0.198	0.8665	30.89
CIII 977.02	4.9	12.01	0.1278	0.2728	2.1349	0.156	0.8598	45.50
SiIV 1393.78	4.9	28.086	0.1152	0.2451	2.1273	0.234	0.8722	28.34
NIII 991.579	5.0	14.007	0.1035	0.2202	2.1299	0.207	0.8680	35.91
SIV 1072.99	5.0	32.06	0.1001	0.2130	2.1288	0.218	0.8697	32.08
SVI 933.38	5.3	32.06	0.0926	0.1970	2.1367	0.138	0.8570	34.55
NV 1238.821	5.4	14.007	0.1123	0.2380	2.1294	0.212	0.8687	30.76
NV 1242.806	5.4	14.007	0.1094	0.2328	2.1379	0.126	0.8550	30.34
OIV 1401.16	5.4	15.999	0.1118	0.2379	2.1280	0.227	0.8711	26.95
OV 1218.393	5.5	15.999	0.1177	0.2504	2.1302	0.204	0.8675	32.86
NeV 1145.6	5.6	20.18	0.0851	0.1817	2.1489	0.021	0.8381	25.89
OVI 1031.924	5.6	15.999	0.1280	0.2720	2.1277	0.230	0.8716	42.16
OVI 1037.614	5.6	15.999	0.1217	0.2595	2.1348	0.157	0.8600	40.36

The spectral lines that were examined are listed in the table in the order of increasing kinetic temperature T_m at which they reach their maximum brightness. The first three columns list the name and wavelength of the line, the value of T_m, and molecular weight of the atom. Next are the measured $\Delta\lambda_{1/2}$(Å). and $J_\lambda(\tau_0)$. These values are used to determine $W(\tau_0)/x_{1/2}(\tau_0)$, the optical depth, and $x_{1/2}$. The last column lists the microturbulent velocities under the assumption that the line is formed at a temperature T_m. Even a quick glance at the table reveals that the values of $J_\lambda(\tau_0)/\Delta\lambda_{1/2}(\tau_0) = W(\tau_0)/x_{1/2}(\tau_0)$ lie within the interval derived above for a Voigt absorption line profile using Eq.(3). In addition, it is easy to see that they lie close to the upper limit of this interval. This confirms the validity of using Eq.(3) on these EUV lines and, second, indicates that these lines are optically thin. The optical thicknesses listed in the table are all less than 0.3. We shall discuss the meaning and significance of these results below, but for now we note that Eq.(13) gives extremely high values for the kinetic temperatures. Difficulty is encountered, even with the classical method, in determining microturbulent velocities is well known (Tandberg-Hanssen 1995). Although the values of T_m we obtained in a refined analysis are lower than those given by the classical approach, they still seem unreasonably high. Below we list some possible reasons for this below.The last column of the table lists the microturbulent velocities (km/s) assuming that the corresponding spectral lines are formed at the temperature where they reach their maximum intensity. We can see that the results vary by comparatively small amounts within 25-45 km/s. They generally lie between 30 and 40 km/s, without a significant dependence on T_m. Thus, the values obtained here appear to be close to the actual values.

6. Discussion

The idea of invoking fluctuations in the surface brightness of prominences as an additional source of information on the radiating volume described above shows that really important information can be extracted by studying the RelMSD of these changes as a function of frequency within a line. Theoretical studies have been compared with the data on changes in the profiles of EUV lines along the slit of the SUMER spectrograph in frameworks of the SOHO space program. Thus, it was shown that, with some exceptions, fluctuations in the surface brightness of prominences in different lines are caused by changes in the optical thickness and that the changes are smaller when the lines are formed at higher effective temperatures. The study of these

fluctuations is especially informative when large-scale or hydrodynamic motions are present in the medium. If the radiating volume participates in rising and falling motions, then the frequency dependence of the RelMSD is characterized by unique "bursts" (local maxima) in the wings of the lines. The magnitude of the latter depends on the velocity of the large scale motions. Observations show that the velocities of these motions correlate with the effective temperatures at which the lines are formed, and they are greater in relatively cold regions of prominences. In hot regions and in the prominence-corona transition zone, only thermal and turbulent motions mainly appear to influence the shape of the spectrum lines. Thus, the profiles of such lines as OVI λ 1032Å, λ 1037.5Å, NeV λ 1145.6Å , NV λ 1238.82Å , etc., can be used to determine the relative contribution of turbulent motions, as well as the optical thickness of radiating volume. The method we propose is extremely simple to use. Determined from observations the ratio $J_\lambda(\tau_0)/\Delta\lambda_{1/2}(\tau_0)$ occupies an important part in this method. This parameter serves as an indicator of the optical thickness of the medium which emits a given spectral line. It appeared that the measured values of this ratio, indeed, lie within the narrow, theoretically predicted range. This confirms the validity of using Eq.(4) for the line intensity. We have also found that all the chosen lines are optically thin and this may be viewed as an additional argument in favor of the assumption that there are no multiple scattering processes taking place in these lines. Once the optical thickness determined approximate formulas (10) and (11) can be used to find $x_{1/2}^{(i)}$, $W^{(i)}$, as well as T_m and ξ_t.

As in the classical method, here also difficulties arise in determining the kinetic temperatures. These are generally rather high. Given the importance of this question, we now discuss it in more details. We begin with pointing out that this problem belongs to the class of inverse and, therefore, incorrectly stated problems, where the precision of the observational data and the stability of the solutions with respect to errors in these data are of great importance. In our case, insufficient spectral resolution ($\Delta\lambda \approx 0.044$ Å) and the relative narrowness of the EUVlines are the major source of difficulty in determining the observed values of $J_\lambda(\tau_0)$ and $\Delta\lambda_{1/2}$. The errors owing to approximating the line profile with a Gaussian shape and in determining the continuum level have comparatively little effect on the final result.

Searches for the possible reasons for the discrepancy between the kinetic temperatures obtained here and the actual values must consider at least two important facts. First, large-scale motions within the prominences may also affect the spectral line profiles. This applies, first of all, to lines characterized by low T_m. The fact that large-scale motions have a significant effect on the

line profiles was noted in (Nikoghossian 2007). The second point concerns the customary assumption that the lines which reach maximum intensity at the same values of T_m are formed in roughly the same regions of a prominence. In fact, the intensities of these lines may have different dependences on kinetic temperature so that, in general, the regions in which they are formed may also differ. In conclusion, we note that the proposed method can, in principle, be refined to include, for example, a fine filamentary structure of the radiating medium. This, however, leads to the appearance of additional parameters which have to be determined and to more rigid specifications for the quality of the observed spectra.

References

Cram L.E., *Sol. Phys*., **22**, 375 (1972)

Jefferies J.T., Lindsey C., *Astrophys. J*. **335**, 372 (1988).

Juvela M., *Astron. Astrophys*., **322**, 943 (1997).

Juvela M., Padovan P., *Astron. Astrophys*., **397**, 201 (2001).

Lindsey C., 1987, *Astrophys. J*., **320**, 893

Madau P., *Astrophys. J.* **441**, 18 (1995).

Nikoghossian A.G., Pojoga S. and Mouradian Z., *Astron. Astrophys*.**325**, 813 (1997).

Nikoghossian A.G., Pojoga, S. and. Mouradian Z, *Astron. Astrophys*. **342**, 785 (1998).

Nikoghossian A.G., Mouradian Z., *Astron. Astrophys*. **360**, 1086 (2000).

Nikoghossian A.G., *Astrophysics,* **45**, 223 (2002).

Nikoghossian A.G., Aboudarham J. and Z. Mouradian, *Astrophysics* **48**, 253 (2005).

Nikoghossian A.G., *Astrophysics,* **50**, 94 (2007).

Tandberg-Hanssen E., *The Nature of Solar Prominences*, Kluver, Dordrecht (1995).

Vial J.-C., in: Webb D., Rust D., and Schmieder B., eds., New Perspectives on Solar Prominences, IAU Coll. 67, ASP, Conf. Series, vol. 150 (1998).

Astronomy & Astrophysics (Caucasus) 4, (2018)

A HYPOTHESIS ABOUT JUPITER'S GALILEAN SATELLITES

R. A. Chigladze, O. I. Kvaratskhelia, G.N. Kimeridze, R.Z. Ivanidze, , SH.G.Gigolashvili

Samtskhe-Javakheti State University,
E. Kharadze Abastumani Astrophysical Observatory, Ilia State University

E-mail: revazchigladze@ yahoo.com
kvara_otar@mail.ru
givikimeridze@gmail.com
r.ivanidze@gmail.com
sh.gigolashvili@gmail.com

Abstract

In the indicated work polarization properties of the light, reflected from Jupiter's satellites, are studied. Maximum difference is noticeable between polarization degrees of light, reflected from the front and rear hemispheres of the satellite. For the satellites, located relatively close to Jupiter (Io, Europe, Ganymede), the magnitude of polarization degree of light, reflected from the front hemisphere, is comparatively less than that the magnitude of polarization degree of light, reflected from the rear hemisphere, and vice versa for the satellite Callisto. In the presented paper an acceptable hypothesis is presented in order to explain the mentioned differences.

Keywords: Galilean satellites, polarization degree, front and rear hemispheres

1. Introduction.

It is possible to name only several scientific works (Dolffus.1975, Geake, Dollfus.1979, Veverka.1971, Botvinova, Kucherov.1980,Bolkvadze.1973,Bolkvadze et al. 1986) in which polarization properties of Jupiter's Galilean satellites are studied insufficiently.

Proceeding from the above stated since 1981 the author has set his mind on the investigation of polarization properties of Jupiter's Galilean satellites in the alpha angle of each phase and in ten different areas of visible spectrum (Chigladze.1984,1985,1987). The observed material was obtained at Abastumani Astrophysical Observatory on both 40-cm refractor and 125-cm reflector, to which the polarimeter ASEP-78 was attached during observations.

Due to the fact that consideration of the effect of Jupiter's surrounding background is rather complicated, we have not conducted Jupiter's observations from limb along 2-3 radii vision ray. It should also be mentioned here that a mean square error of one measurement during observation without filter does not exceed 0.05%. The observational method is described in the work in detail. (R.A.Chigladze 2001).

In general the magnitude of polarization degree of the light, reflected from the satellite's surface, must vary depending on α-phase angle, satellite orbital longitude L, wave length λ and observation period t, or $P = P(\alpha, L, \lambda, t)$.

2. Observations.

In the indicated work polarization properties of the light, reflected from Jupiter's satellites, are studied. Maximum difference is noticeable between the polarization degrees of the light, reflected from satellites' front and rear hemispheres. For the satellites, located relatively close to Jupiter (Io, Europe, Ganymede), the magnitude of polarization degree of light, reflected from the front hemisphere, is comparatively less than the magnitude of polarization degree of light, reflected from rear hemisphere, and vice versa for satellite Callisto. An acceptable hypothesis is presented in order to explain the mentioned differences.

Based on the processing of obtained material we deduce that:

The magnitude of polarization degree of the light, reflected from the front side ($L \approx 90^o$) of the satellite Io during observations without filter is in absolute magnitude by 0.15 – 0.20% less than the magnitude of the polarization degree of the light, reflected from the rear side ($L \approx 270^o$) when the phase angle $\alpha \approx 5^o$, while the magnitude of polarization degree of the light, reflected from satellite Io's rear hemisphere is equal to $P(\alpha) = P(5^o) = -0{,}38\%$ (Table 1).

Table 1

Io

Data	Telescope (cm)	α^o	L^o	P%
1981				
March				
0.909	40	4.9	100	-0.20
1982				
March				
27.960	125	5.6	270	-0.38
28.875	125	5.2	114	-0.21
1985				
July				
8.836	125	5.6	70	-0.18
1987				
September				
24.958	40	5.3	280	-0.39
25.948	40	5.2	123	-0.20

The magnitude of polarization degree of light, reflected from satellite Europe's front side during observations without filter is in absolute magnitude by 0.12% less than the magnitude of polarization degree of light, reflected from the rear side, when phase angle $\alpha \approx 3^o.5$, and the magnitude of polarization degree of light, reflected from satellite Europe's rear hemisphere, is equal to $P(\alpha) = P(3^o.5) = -0.25\%$ (Table 2).

Table 2

Europe

Data	Telescope (cm)	α^o	L^o	P%
1982				
May				
16.881	125	4.0	322	-0.24
21.911	125	4.9	113	-0.12
1984				
June				
7.801	40	4.6	263	-0.24
9.941	40	4.0	120	-0.15
1985				
July				
10.854	40	3.5	262	-0.25
1987				
September				
27.875	125	4.7	124	-0.13

The magnitude of polarization degree of the light, reflected from satellite Ganymede's front side during observations without filter in absolute magnitude is by 0.15 – 0.18% less than the magnitude of polarization degree of light, reflected from the rear, when phase angle $\alpha \approx 5^o$, while the magnitude of polarization degree of the light, reflected from satellite Ganymede's rear hemisphere, constitutes $P(\alpha) = P(5^o) = -0.40\%$ (Table 3).

Table 3

Ganymede

Data	Telescope (cm)	α^o	L^o	P%
1981				
March				
3.952	40	4.4	289	-0.42
1982				
May				
16.923	125	4.0	3.2	-0.18
18.896	125	4.4	131	-0.22
21.952	125	4.9	284	-0.40
1985				
July				
7.870	40	5.8	91	-0.15
10.813	40	5.3	239	-0.35
1987				
September				
25.844	125	5.2	95	-0.21
28.903	125	4.5	249	-0.36

The magnitude of polarization degree of light, reflected from satellite Callisto's front side during observations without filter in absolute magnitude is by 0.65% more than the magnitude of polarization degree of the light, reflected from the rear side, and constitutes 0.35% (Table 4).

Table 4

Callisto

Data	Telescope (cm)	α^o	L^o	P%
1982				
July				
12.946	125	10.6	89	-0.98
August				
15.790	40	10.1	97	-0.95
1984				
August				
29.849	40	10.1	268	-0.42
1985				
June				
12.818	40	9.4	295	-0.43
1988				
September				
12.917	40	11.3	277	-0.26
13.042	40	11.3	280	-0.29
22.024	40	10.6	93	-1.08

3. Analysis .

It is evident that the magnitude of polarization degree of the light, reflected from the front hemisphere of the first three satellites (Io, Europa, Ganymede), is less than the magnitude of polarization degree of the light, reflected from the rear hemisphere, while in the case of satellite Callisto it is vice versa. One of the possible hypotheses for explaining this phenomenon is the following: as is known there is a shower of a multitude of meteorites, moving both on circular and elliptic orbits. Showers of meteors, moving on elliptic orbits in the direction, coinciding with

that of the satellite direction, must be the reason of the above mentioned exposed difference. These showers are falling asymmetrically upon the satellites' front and rear hemispheres.

In order to facilitate our calculations let us review meteor showers, the pericenter of which is ~$6R_J$ close to the satellites' (specifically Io's) orbit, located near the planet, and the apocenter ≈ $26R_J$ close to satellite Callisto's orbit.

In such a case, as is well-known from celestial mechanics, velocity of a body's movement in perocenter and apocenter is calculated using the following formulae:

$V^2 = V^2_c\ (1+ e)/(1 - e)$ (in pericenter), $V^2 = V^2_c\ (1- e)/(1 +e)$ (in apocenter), where V_c is main velocity of an object, moving on the orbit, and e – orbit's excentricity.

On the one hand, it may be easily obtained that the velocity of meteoric bodies, having the above mentioned properties, will equal to V = 22.50 km/sec. in pericenter and V = 5.04 km/sec. in apocenter.

On the other hand, optimum velocities of Galilean satellites, moving on circular orbits, are: for Io 16.94 km/sec., Europa 13.43 km/sec., Ganymede 10.63 km/sec. and Callisto 8.01 km/sec.

Evidently, the indicated meteoric bodies are falling upon Io from the rear side ($V_{Flow}>V_{Io}$), while in the case of Gallisto ($V_{Cal} > V_{Flow}$) we have the opposite picture. Callisto is gathering on and overtaking meteor showers, which bombard it from the front side due to the fact that the majority of meteoric bodies are dark (have less albedo and a high polarization degree). Consequently the light, reflected from the satellite's indicated side corresponds to the higher polarization degree (Chigladze,2006,2012,2015,2018). As the mentioned effect lasts for billions of years, the satellite's front and rear sides differ from each other.

REFERENCES

Bolkvadze O, University of Helsinki, 1981. 73.

Bolkvadze, O.I.Kvaratskhelia, A.N.Korol, A.K.Maier L.A. Sigua R.A.Chigladze, Bull. Abastumani Astrophysikal Observatory, 1986. 61, 269.

Botvinova V., V.A . Kucherov, Astron-Astrophys , 1980.

Chigladze R, Astronomicheskii Tsirkulyar No.1320/APR16, 1984, p.4

Chigladze R, Bull.of the Academy of Sciences of Georgia, 1985. 118, 513.

Chigladze R, Proceedings of Tbilisi University, 1987. 270, 240.

Chigladze R,Poceedings of Akhaltsikhe Branch of Tbilisi State University. 2001. 2, 170.

Chigladze R, Dissertation. Abastumani, 2006. 186.

Chigladze R, Bull.Georgian National Sciences, 2012. 6 , 96.

Chigladze R**,**Electropolarimetric and Electrofotometric Investigation of Jupiter's Galilian Setellites". International Scientific Conference ,,Problems of Modern Astrophysics" Akhaltsikhe.2015.

Chigladze R.,M.Tateshvili. Results of Observations over Jupiter's Galilian Setellites, Astronomy & Astrophysics (Caucasus) 2018,3,23-29.

Dolffus A, Icarus., 1975. 25, 416.

Geake, K, A.Dollfus. Icarus., 1979. 343.

Veverka I, Icarus,1971. 14, 355.

Astronomy & Astrophysics (Caucasus) 4, (2018)

MOLECULAR HYDROGEN IN GIANT PLANETS: JUPITER AND SATURN

A.A.Atai[1] and E.R.Yuzbashov[2]

1. Shamakhy Astrophysical Observatory named after N.Tusi of Azerbaijan National Academy of Sciences
2. Institute of Physics of Azerbaijan National Academy of Sciences

E-mail: atai1951@yahoo.com

Abstract

The paper deals with the results of an investigation of the absorption spectra of molecular hydrogen in the visible region for Jupiter and Saturn. Based on the observational material of Jupiter and Saturn on the echelle spectrometer with a CCD receiver at the Cassegrain focus of the 2-m telescope of the ShAO, the weak quadrupole lines of molecular hydrogen of the band H_2 (4-0) in the visible region of the spectrum with the spectral resolutions of R = 14000 and R = 56000 were obtained. The upper limit of the intensity of S (2) line was determined in the spectra of Jupiter and Saturn. On the lines of bands H_2 (4-0), S (0) and S (1), certain parameters were determined in various details of the atmospheres of Jupiter and Saturn, which play an important role in understanding their energy balance. Namely, it was established that the pressure, temperature and amount of molecular hydrogen do not obey any monotony along the different parts of the Jovian disk along its meridian. This behavior of the pressure and temperature values at the depth of the formation of molecular hydrogen lines may be due to the release of energy in various parts of Jupiter disk caused by a weak spontaneous conversion of orthohydrogen to parahydrogen, occurring in the deep layers of Jupiter, as a thin layer above the liquid molecular hydrogen, even in the absence of a catalyst. It was established that the process of the conversion, occurring in different belts, zones and in different depths, has different speeds and spatial scales and depends on the temperature and the amount of orthohydrogen.

Key words: Jupiter, Saturn, quadrupole lines of molecular hydrogen, ortho- para-hydrogen

1. Introduction.

Accurate data on the chemical composition of the atmosphere of the giant planets is so important that without it, it is impossible to understand the process of cloud-formation and coloring of details on their disks. The "Juno" spacecraft, which is currently continuing its research of Jupiter, along with other tasks, determines the chemical composition of the atmosphere of the planet.

At the beginning of the 20th century, the absorption bands of molecular gases with small and medium dispersion in the spectra of large planets of the solar system were studied by Slipher (Slipher V.M., 1909; Slipher V.M., 1933) and for over 100 years the scientists have been trying to refine the chemical composition of the atmosphere of the planets in order to further follow the physical phenomena that occur in their atmospheres in a more precise manner.

A part of the observed bands Wildt R. (Wildt R., 1932) identified with the laboratory spectra of ammonia, and these bands have the maximum intensity in the spectrum of Jupiter, a few times weaker in the spectrum of Saturn. As for the spectra of the other two distant planets, they do not contain the bands of NH_3 in the optical (visible) range, but at λ = 8.22 mm, an ammonia band is detected for Uranus (Kuzmin A.D., Lasovsky B.Ya., 1971). Besides, the intensity of methane absorption bands (Adel A., Slipher V.M., 1934a; Adel A., Slipher V.M., 1934b), on the contrary, increases with the transition from Jupiter to Neptune.

The absence of gaseous ammonia and the abundance of methane for Uranus and Neptune can be explained by freezing ammonia, what is caused by the decrease in the amount of solar heat incident on their surface, due to the great remoteness of these planets.

Calculations of the molecular weight for the atmospheres of the giant planets obtained during the overlapping of stars by their disk give low values. For example, for the Jovian atmosphere, the value of $\mu = 3.3$ is obtained when the σ star is covered by Aries. Such a low value of μ can be explained by the fact that the upper layers of the atmosphere of this planet consist mainly of molecular hydrogen and helium. The existence of a smaller average density of Jupiter compared to even the Sun and the presence of hydrogen compounds suggest that the Jupiter atmosphere consists primarily of hydrogen.

Presently, it is established that hydrogen is the most abundant element in the universe. It accounts for about 92% of all atoms (8% are helium atoms, the fraction of all other elements taken together is less than 0.1%) (for Jupiter the ratio H_2/He by mass is 80:20, for Saturn, it is 89:11, for Uranus 88:12, and for Neptune 85:15) (L.V. Ksanfomaliti, 2012). Thus, hydrogen is the main constituent of the stars, the giant planets and interstellar gas.

If, as a result of the thermal motion, the hydrogen atoms get close to each other, then attractive forces arise and the atoms, under certain conditions, can combine to form hydrogen molecules. In such a more probable state, the molecules have a minimal potential energy.

Note that a direct spectral observation of molecular hydrogen is difficult. Electronic transitions are manifested in the ultraviolet region, which is opaque to the Earth's atmosphere and observations in this area can only be carried out using a spacecraft. Because of the absence of a dipole moment in homonuclear diatomic molecules, including molecular hydrogen, rotational-vibrational and rotational transitions are impossible. If we take into account that such molecules can have a quadrupole moment, the rotational-vibrational and rotational transitions associated with this moment can lead to a very weak emission or absorption of radiation in the visible and infrared regions.

In 1938, Gerhard Herzberg (Herzberg G., 1938) predicted that the quadrupole bands of molecular hydrogen H_2 should be detected in the spectra of the giant planets. He also showed (Herzberg G., 1952) that the weak, unidentified absorption line found by Kuiper (Kuiper G.P., *1949*) on the low-dispersion spectrum of Uranus and Neptune is undoubtedly the S (0) (3-0) line of the second overtone-induced H_2 band. It took another 10 years for Kiess C.C., Corliss C.H. and Kiess H.K (Kiess C.C., Corliss C.H. and Kiess H.K., 1960), when, it became possible to detect three lines of the rotational-vibrational overtone (3-0) at about 8,200 Å, and Spinrad H., Trafton L. (Spinrad H., Trafton L.M., 1963) discovered two more lines of H_2 (4-0) overtone, near 6400Å in the spectrum of Jupiter. Later, the lines of both bands of molecular hydrogen were found in the spectra of all giant planets: H_2 (4-0) overtone was most useful for quantitative studies of the planetary atmospheres. Its usefulness is that the extremely small value of their intensity makes it possible to assert that the lines H_2 (4-0) are not saturated, even in the spectra of H_2 from deep atmospheres.

Therefore, the spectrophotometric studies of quadrupole absorption lines of molecular hydrogen, which is the main mass of the giant planets, is an important problem, and these studies will reveal the essence of many phenomena that occur in their atmospheres and are reflected in the dynamics of clouds observed on the disks of the planets.

This paper studies the absorption of molecular hydrogen in the visible region of the spectrum of Jupiter and Saturn. The induced absorption band of S(4-0) molecular hydrogen H_2 has a central wavelength of near λ6420Å and two lines are observed in it – λ6367.76Å и λ6435.03Å. The second absorption line of molecular hydrogen in the Jupiter spectrum at λ6435.03Å blends with the NH_3 ammonia line and therefore, it is difficult to observe them separately at a low resolution. These studies also include studies of the molecular lines S(0), S(1) (in the 4-0 band) of absorption in the reflected spectrum of the giant planets.

2. Absorption spectra of molecular H_2 in the S(4-0) band for Jupiter and Saturn.

In 2014-2016, the spectra of Jupiter and Saturn were obtained with a 2-meter telescope of the ShAO with different spectral resolutions: R = 14000 and R = 56000. The spectra with resolution R = 14000 were obtained with the aid of an echelle spectrometer with a CCD camera (580x530 pixels, an element size 24x18 μm) installed in Cassegrain's Focus. Spectra with a resolution of R = 56000 were obtained using a fiber-optic echelle spectrograph (SHAFES). As a light detector, we used an American CCD camera with a 4K × 4K matrix of elements with a cell size of 15x15 μm. This and other spectrometers installed on a 2-m telescope are described in greater details in the works of K.M. Mikailov *et al.,* (Mikailov Kh.M., et al., 2005; Mikailov Kh.M., and et al., 2017).

Of the two lines of molecular hydrogen H_2 that are in the visible region of the spectrum of Jupiter – λ 6367.76Å and λ 6435.03Å in the H_2 (4-0) band, one (second) blends with NH_3 λ 6435.30Å ammonia line (Fig.1).

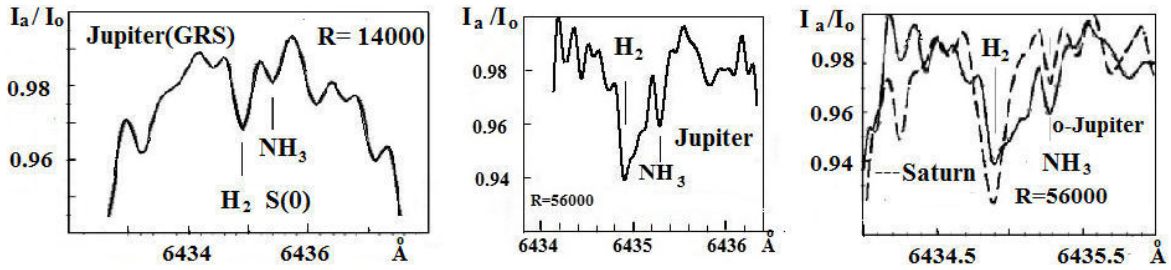

Fig.1. The absorption lines of molecular hydrogen in the band (4-0) λ 6435.03Å and ammonia NH_3 λ 6435.30Å in the spectra of Jupiter and Saturn: a) R = 14000, b) R = 56000 (Jupiter), c) both lines in the spectra of Jupiter and Saturn.

In the spectrum of Jupiter, the line of molecular ammonia NH_3 λ 6435.30Å (Fig.1.a, R = 14000) does not show up and is seen as an ordinary depression. And Figure 1.b shows the absorption line in the same spectral region of Jupiter, obtained with spectral resolution R = 56000 in the central part of the planet's disk: at a high spectral resolution, splitting of the lines into λ6435.30Å and λ6435.03Å. Of particular importance is the spectra of Jupiter and Saturn (Fig.1.c), obtained with a spectral resolution (R = 56000), along which it is possible to determine the intensities of those two lines of molecular hydrogen and ammonia. The figure shows a clear absorption in the line NH_3 λ6435.30Å and in the extended line H_2 λ6435.03Å: the intensity of the ammonia line on Saturn is much weaker than on Jupiter.

Observing Jupiter on the 2-m telescope with a spectral resolution of R = 56000 allowed us to reveal another term associated with the weak quadrupole transition of molecular hydrogen - H_2 (4-0) S (2). A report on the detection of an absorption line at λ 6313.4 Å was first published in (Encrenaz T. and Owen T., 1973), and later in (Smith W.H. and et al., 1989). It should be noted that Encrenaz *et al.* (Encrenaz T. and Owen T., 1973) previously estimated the upper limit of absorption in the H_2 (4- 0) S (2) line. The H_2 (4-0) S (2) line in the Saturn spectrum was revealed during our observations. According to Smith's estimates (Smith W.H. and et al., 1989), the intensity of the H_2 (4-0) S (2) line in the Jupiter spectrum is ~1.8 mÅ, that is in compliance with our measurements. During the processing of the observational material of the profile of the H_2 (4-0) S (2) line in the Saturn spectrum, we determined its intensity, which, according to our measurements, turned out to be ~ 5 mÅ (Fig.2a) and b)).

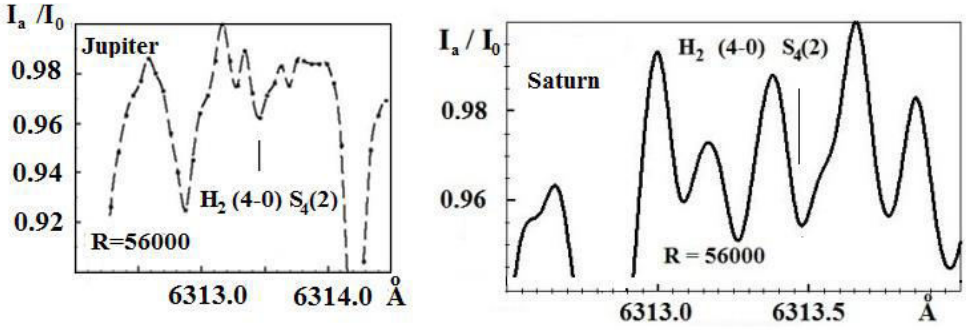

a) b)

Fig.2. The H_2 (4-0) S (2) line profile in the spectra of Jupiter (left) and Saturn (right), obtained with a spectral resolution of R = 56,000.

In the spectral region, in which the absorption line S (1) λ 6367.76Å located, there is also a weak telluric line λ 6368.46 Å. In determining the equivalent width and correcting the Doppler shifts, the corresponding lines of the solar spectrum were taken into account as a comparison. In 2014, the spectrum was taken along the meridian in the direction of the north in two regions of the Saturn disk - in the center and polar regions (Fig. 3).

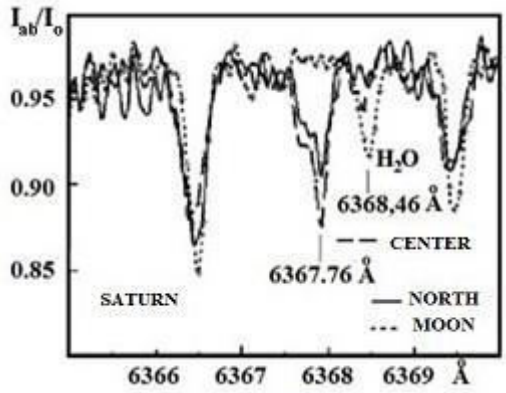

Fig.3. The spectra of Saturn and the Moon in the region of the molecular hydrogen line S(1) λ 6367.76Å (The solid line is the northern part, the dotted line is the central part of Saturn's disk; the points are the spectrum of the Moon).

The intensities of the quadrupole line of molecular hydrogen H_2 on Jupiter, S (0) 6435.03Å and S (1) 6367.76Å were determined along the meridian, i.e. in the different parts of the planet. After that, the rotational temperature for the observed details of Jupiter along the meridian was calculated from the intensity ratios S (0) 6435.03Å and S (1) 6367.76Å (Fig. 4). The results of our calculations in the central part of the disk of Jupiter coincide well with the results of the calculated temperature values (105-110 K) corresponding to a level of 150 mbar on Jupiter according to infrared observations Voyager 1-2 along the planetographic longitude L (Flasar F.M., 1986).

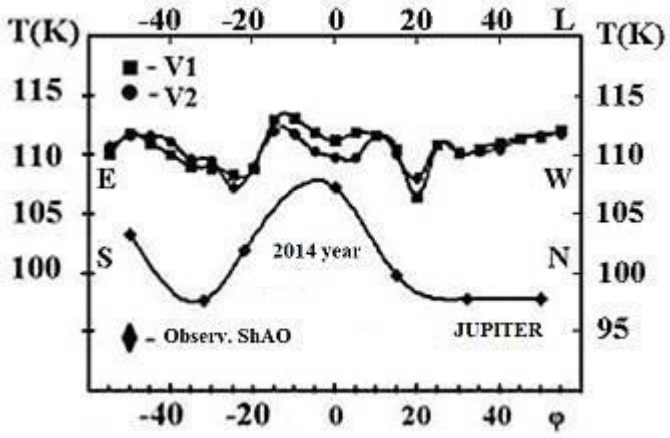

Fig.4. The calculated temperature values corresponding to a level of 150 mbar on Jupiter from the Voyager 1-2 observations along the planetographic longitude L (EW) (squares - V1-March 1979, circles -V2-July-1979). Based on the results of our observations, the rotational temperatures in different parts of the disk are calculated from the latitude φ of Jupiter (SN).

In the different parts on the disk of Jupiter, by taking into account the instrumental half-width, the pressure values in the depth, in which the lines were formed, were estimated by the half-widths of lines λ 6367.76Å and λ 6435.03Å in the band (4-0) of molecular hydrogen (Table 1). Clearly, in different details on the disk of Jupiter, as well as Saturn, the pressure values should be different. This is clearly seen from Table 1. The discrepancies in the pressures for the Jupiter atmosphere are due to the inaccuracy of the determination of the half-width of weak line S (0) 6435.03Å, which is not devoid of overlapping of the 6435.30Å ammonia line with the long-wavelength wing of molecular hydrogen.

As it is known, the observed course of molecular absorption along the Jupiter disk is well interpreted within the framework of a two-layer model of the absorption line (or band) formation, taking into account the role of multiple scattering and absorption inside an optically dense cloud layer. To determine the hydrogen content within the framework of the two-layer model of the atmosphere, the growth curve constructed by V.G. Teyfel (Teyfel V.G., 1980) was used. The necessary parameters were chosen from the results of studies of methane absorption bands (g_s=0.5; r_c =0.75; b^*=2.0, where g_s is the asymmetry parameter of the scattering indicatrix, r_c is the diffuse reflection coefficient in the continuous spectrum, $b^*=\sigma_{a0}H_0$; (H_0 - scale of heights), σa0 is the volume coefficient of aerosol scattering). Using this growth curve, according to the measured values of the line intensity S (1) λ 6367.76 Å, the concentration of molecular hydrogen in the overcloud atmosphere U (H_2), the amount of absorbing gas per average mean free path of photons between two scattering events in the cloud layer A_L and the specific gas content per unit length of free path w_s for the atmospheres of Jupiter and Saturn (Tables 1 and 2) were determined.

Table 1. Half-widths and equivalent widths of molecular hydrogen lines S(0), S(1); the calculated pressure values in the depth, in which the lines were formed in the Jovian atmosphere; content of H_2 – U (km·amagat, A_L (km·amagat) and $w_s \cdot 10^6$ (km·amagat)cm^{-1} (b=5) for various details of the planet disk.

Jupiter								
Details	S(1) Δλ (Å)	S(0) Δλ (Å)	P_1 (atm)	P_0 (atm)	W (мÅ)	A_L	U	$w_s \cdot 10^6$
NPR	0.16	0.26	0.343	0.546	10	3.02	15.1	7.55
NTrZ	0.16	0.12	0.34	0.25	9.6	2.87	14.33	7.16
NEB	0.21	0.131	0.45	0.275	11.8	3.76	18.82	9.41
EZ	0.15	0.09	0.32	0.19	15	5.27	26.34	13.2
GRS	0.12	0.235	0.257	0.49	10	3.02	15.1	7.55
STrZ	0.21	0.17	0.45	0.357	11	3.42	17.12	8.56
SPR	0.17	0.125	0.365	0.262	10.2	3.1	15.5	7.75
Center[*]	b=5					2.4±0.4	12±2	4±0.7
**Teyfel V.G. 1980*	b=2					5.8±1.0	12±2	3.9±0.7

Table 2. Half-widths of molecular hydrogen H_2 (4-0) S(0), S(1); calculated pressure values in the levels of their formation in the Saturn's atmosphere; content of H_2 – U (km·amagat, A_L (km·amagat) and $w_s \cdot 10^6$ (km·amagat)cm^{-1} for two details of the planet disk.

Saturn R = 56000								
Details	S(0) Δλ (Å)	P_0 (атм.)	S(1) Δλ (Å)	P_1 (atm.)	A_L	U	$w_s \cdot 10^6$	b =4.0
Central part	0.266	0.457	0.311	0.547	4.3	21.5	8.6	
North pole region	0.146	0.25	0.146	0.25	4.2	20.8	8.3	
Central part					9.6	19.1	19.1	b=1.5
North pole region					9.2	18.45	18.5	
Center [*]					6.4±2	25±9	8.5±2.8	b=4.0

It was interesting to compare the results of our observations with the results of calculations performed in the framework of the zonally symmetric linear radiation dynamic model developed in (Conrath B.J., Gierasch P.J. and Leroy S.S., 1990). Figure 5 shows the IRIS (*Infrared Interferometer Spectrometer and Radiometer*) data in comparison with the model calculations for Jupiter and Saturn. Attention is drawn to the good agreement of the seasonal effect of Saturn and the effects of the zonal jets of Jupiter. The poor agreement near the equator, especially for Saturn, is due to the failure of the linear model, and the results of our observations in 1971/74 also confirm the identification of the seasonal effect.

The averaged values of the rotational temperature, determined from the lines of molecular hydrogen, which are formed in the depth of the Jovian atmosphere, where the pressure varies between 0.2 ÷ 0.5 atm. correspond to a maximum of 110° K in the center of the planet's disk and less than 100° K in nearby poles. The determination of the temperatures for the Northern polar and central parts of the Saturn disc was carried out according to the observations of 2013-2015, which are in good agreement with the measurements of 1971-1974.

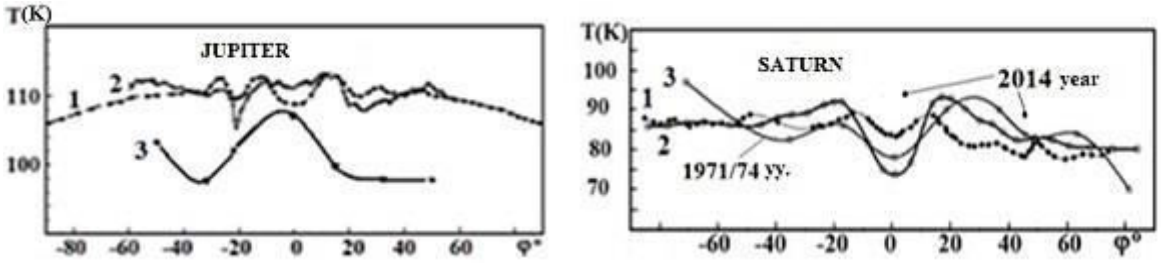

Fig.5. Comparison of IRIS data with model predictions for Jupiter and Saturn. These temperatures correspond to a level of 150 mbar. 1 - model calculations (Conrath B.J., Gierasch P.J. and Leroy S.S., 1990), 2 - IRIS data, 3 - our calculations.

On the basis of the observational data on the study of quadrupole lines H_2 (4-0) along different parts of the Jovian disk along its meridian, it was established that the pressure, temperature and quantity of molecular hydrogen do not obey any monotony. This behavior of the pressure and temperature values at the depth of the formation of molecular hydrogen lines may be due to distinguishing features of the thermal-infrared radiation of the planet.

3. On the thermal, infrared radiation of Jupiter and Saturn

Knowing of the physical features of the chemical composition of molecular hydrogen under the atmospheric conditions of giant planets can provide a better understanding of the energy balance of the planets and their atmospheric structures. Hydrogen, apparently, hides in itself many more secrets and riddles; and more secrets are hidden in the molecular hydrogen.

In the early twentieth century, Mecca (Mecke R., 1925) found that in the bands of molecules with identical nuclei in general, and in particular in H_2, the intensities of consecutive lines vary unevenly. More often there is a striking change of strong and weak lines. Without involvement of quantum mechanics, it is impossible to explain these observational facts.

As it is known, the total function of the system must be antisymmetric with respect to the permutation of two protons. In the case of molecular hydrogen, the total proton wave function can be represented as the product of the spatial wave function by the spin wave function. The latter can be symmetric or antisymmetric, depending on the arrangement of spin vectors of both electrons in parallel or antiparallel manner.

Lately, Heisenberg (Heisenberg W., 1926; Heisenberg W., 1927) and Hund (Hund F., 1927) later, explained this on the basis of specific quantum-mechanical symmetry conditions as follows: in the H_2 molecule, only transitions between the states with the same symmetry of spatial coordinates relative to the position of the nuclei are possible. For molecular hydrogen molecules, both eigenfunctions represent physically possible states and therefore, the molecular states must be divided into two types that practically do not combine with each other in a state of thermal equilibrium. The above studies allowed Dennison (Dennison D.M., 1927) to explain the special course of the curve of the rotational heat capacity of the molecular hydrogen at low temperatures discovered by Aiken as early as 1912 (Eucken A., 1912). Using more recent data in his calculations, Hori (Hori T., 1927) confirmed Dennison's ideas.

Under normal conditions, molecular hydrogen is a mixture of two isomers: ortho- and parahydrogen. In orthohydrogen (o-H_2), the magnetic moments of the nuclei (spins) have the same orientation, and in parahydrogen (p-H_2) they have an opposite orientation.

Hori (Hori T., 1927), on the basis of the moment of inertia of the hydrogen molecule, found that the experimental data are best satisfied when the para- and orthohydrogen

concentrations are related as 1:3. The usual hydrogen contains ~ 75% o-H_2 and ~ 25% p-H_2. Based on these considerations, it is possible to explain the temperature dependence of the isobaric rotational heat capacity of hydrogen containing orthohydrogen and parahydrogen in various proportions (Fig. 6). The same figure shows the temperature dependence of the equilibrium ortho fraction of hydrogen (dashed pink line).

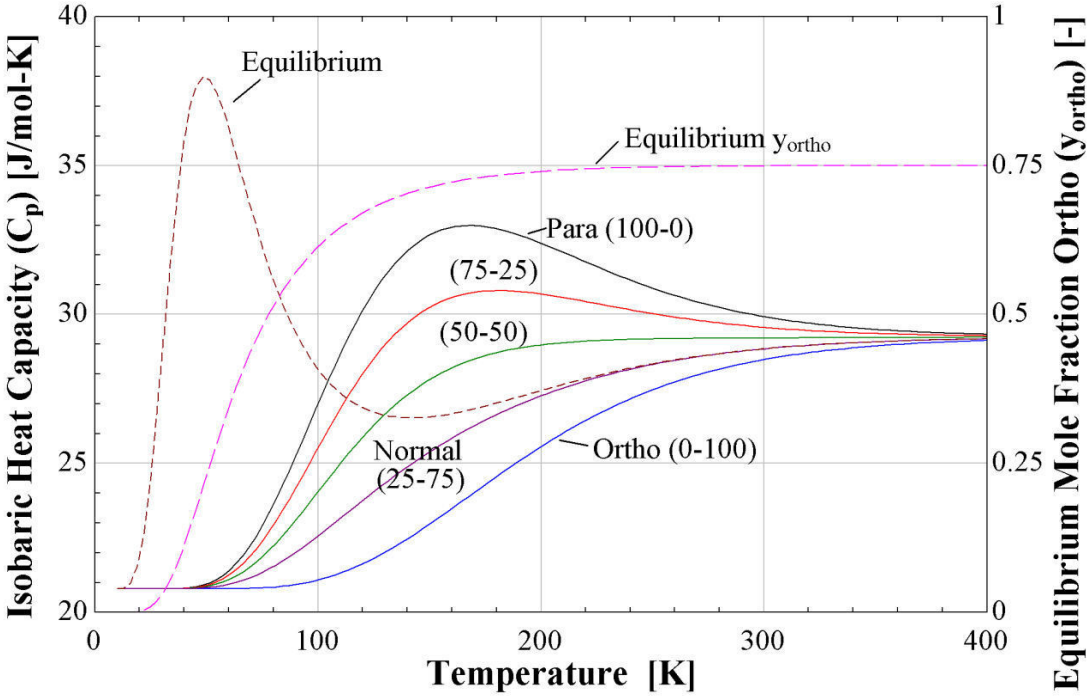

Figure 6. Isobaric Heat Capacities plotted versus temperature for various orthohydrogen-parahydrogen compositions. The equilibrium composition and heat capacity curves are also plotted to show the correlation between the change in composition and effective heat capacity (Bliesner R.M., 2013).

For the molecules of the same type, rotational states are possible only with odd quantum numbers (orthohydrogen), but for the molecules of another type, they are possible with even numbers (parahydrogen). In Fig. 7a, possible quadrupole transitions for hydrogen molecules are shown: for $\Delta J = 0$ the transitions form the Q-branch, for $\Delta J = +2$ they form the S-branch, and for $\Delta J = -2$ they form the O-branch in the spectra of H_2. Since the transitions between symmetric and antisymmetric states are extremely unlikely, then all molecules with symmetric states on cooling fall into state J = 0, and those molecules that were at antisymmetric state before cooling can only go to the lowest antisymmetric state, i.e. to the second rotational level – J = 1. When the temperature is lowered, the equilibrium is not established, but ratio (1 p-H_2 + 3 o-H_2) / 4 is maintained, so that ordinary hydrogen, which is cooled to low temperatures, is not in the state of the thermodynamic equilibrium. The p-H_2 molecules are collected in the zero rotational quantum state, and o-H_2 molecules in the first one (Fig. 7b).

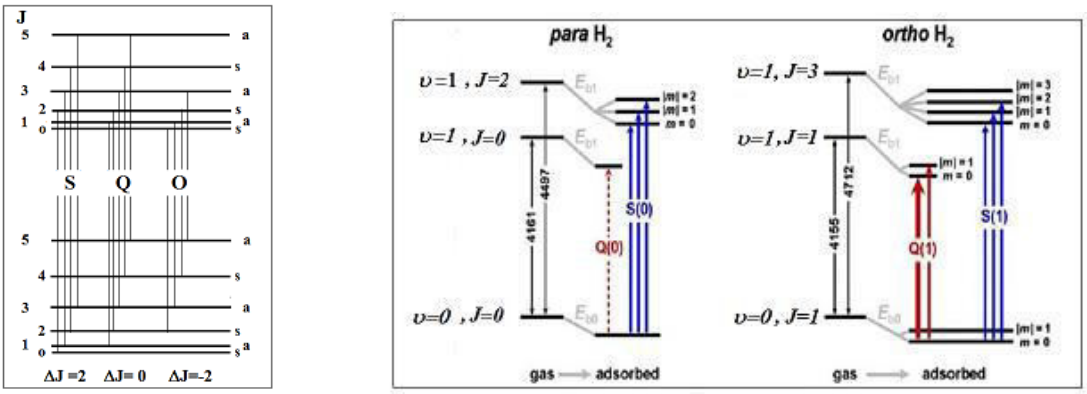

a) b)

Figure 7. Quadrupole transitions of H_2 between even and odd energy states correspond to: a) $\Delta J = +2$ – S-branch, $\Delta J = 0$ – Q-branch and $\Delta J = -2$ – O-branch; b) molecules with symmetrical quantum state transit to state J = 0 (p-H_2) upon cooling, and those molecules that were in antisymmetric state before cooling can only go to the lowest antisymmetric state, i.e. to the second rotational level – J=1 (o- H_2).

It is worth to note that if it is possible to classify the electronic terms of the band spectrum, then from the alternation of intensities, one can draw a conclusion about the statistics of the nuclei. For example, if for a symmetrical electronic term the lines with even J are weaker, then the nuclei obey Fermi statistics. This takes place, for example, for the H_2 molecule, meaning the protons satisfy the Pauli principle. On the contrary, Fermi and Razetti in the Raman rotational spectrum have established that the nitrogen nucleus obeys the Bose-Einstein statistics (Fermi E., Rasetti F., 1931).

When the spin of the nucleus is zero (as in the case of O_2 and He_2 molecules), alternation of intensities does not occur, and every second line falls completely (for both O_2 and He_2 all antisymmetric lines are absent). Therefore, Bose-Einstein statistics are valid for these nuclei.

It is known that giant planets emit more heat than they receive from the Sun. For example, the heat generated inside Jupiter is comparable with the heat it receives from the Sun and it is emitted into space in the form of infrared radiation (Fig. 8a). The interchange of the patterns of this radiation can be associated with the convection of warm and cold masses in the zones and belts of the disk of Jupiter (Fig. 8b).

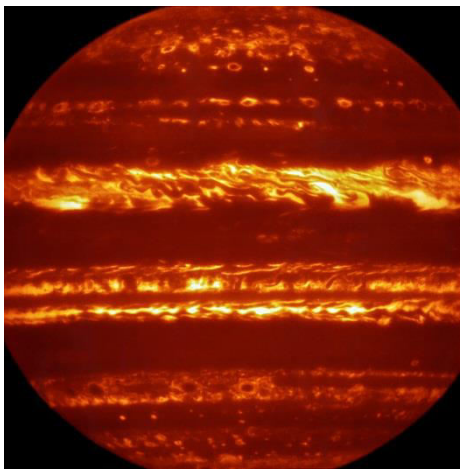

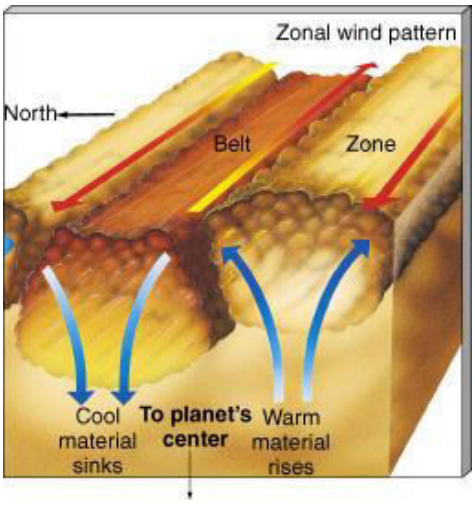

a) b)

Figure 8. a) Jupiter imaged using the VISIR instrument on the VLT ("Jupiter imaged") and b) Zones and belts on Jupiter ("Zones and belts") .

Note that none of the mechanisms proposed in the scientific literature can explain the origin of the source of this internal energy. In this paper, based on some preliminary calculations, another possible mechanism for the generation of heat in the interior of Jupiter and Saturn is proposed, namely the mechanism of energy generation during the conversion of orthohydrogen to parahydrogen.

It is known that the conversion of o-H_2 into p- H_2 is accompanied by the release of heat (~1400 J / mole). In the liquid phase of ortho-para H_2, conversion can occur at a noticeable rate, especially in the presence of a catalyst, and is accompanied by the release of heat. Thus, it could be expected that as a result of spontaneous establishment of equilibrium at low temperatures there will be a change in certain thermal properties of H_2 with time, and certainly this is an important factor in understanding the essence of the mechanism of release of internal energy in giant planets. This feature is also sensitive to the abundance of hydrogen, the ratio of ortho-para-hydrogen, vertical structure of the atmosphere, and also the dependence of the temperature and pressure profile in the atmospheres of the planets.

The release of surplus and various energies in various parts of the Jupiter disk can be caused by the spontaneous conversion of orthohydrogen to parahydrogen, occurring in the deep layers of Jupiter, in the region above liquid molecular hydrogen, even in the absence of a catalyst. The process of conversion, occurring in different belts, zones and in different depths, has different speeds and spatial scales, and also depends on the temperature, the amount of orthohydrogen.

Under high pressure, for example, in the bowels of Jupiter and Saturn, the physical characteristics of molecular hydrogen become unusually complex and unique. If we consider the vertical section of Jupiter and take into account that the main constituent of the mass of this planet is hydrogen and helium, we get the following picture: after the troposphere of Jupiter, with deepening into the depths of the planet, the pressure increases, the gas density increases and the temperature increases too. A further increase of pressure leads to the hydrogen liquefaction. In principle, under certain conditions, solid hydrogen may also occur. Under such extreme conditions, under the cloud layer of gas giants, metallic atomic hydrogen is formed, which will have zero electrical resistance.

The fact that liquid and solid hydrogen can be made metallic was predicted back in 1935. Physicists Wigner E. and Huntington H. B. J. (Wigner E, Huntington H. B. J., 1935) claimed that for the transition of hydrogen to the metallic state, a pressure of 250,000 atm. (25 GPa) would be required. In modern laboratory conditions, more than 1 TPa is obtained by dynamic methods. It is assumed that metallic hydrogen has superconducting properties at temperatures above room temperature. Therefore, the desire of several competing teams of physicists in obtaining this exotic substance in laboratory environment, under pressure, exceeding the normal atmospheric pressure from 10 thousand to 1.5 million times, is not surprising.

In some experiments, a rapid transition of hydrogen from a transparent state to a state of a shiny metal that reflected light was observed. Recent experiments have indicated that at sufficiently high pressures, before going into a metallic state, hydrogen begins to "darken", i.e. hydrogen loses its former transparency. This "dark" hydrogen is a transitional state between the gaseous and metallic forms of hydrogen, and it has very poor electrical conductivity (Dias R.P. and Silvera I.F.,2017).

From the point of view of the energy band structure, gaseous, liquid and solid hydrogen are dielectrics and, as it is known, are transparent in the optical range. Such a change in the optical properties of hydrogen under high pressures indicates that the energy gap between the

conduction band and the valence band has decreased, i.e. hydrogen passed from the dielectric state to the semiconductor one. With a further increase in pressure, the distance between the nuclei becomes much smaller than the Bohr radius and becomes comparable to the de Broglie wavelength of the electrons. In this case, the binding force of the electron with the nucleus becomes non-localized, the electrons weakly bind to protons and form a free electron gas in the same way as in metals (Nellis W.J., 2000). The discovery of a new form of hydrogen has two important implications for the field of planetary science. First, the high thermal conductivity of such a form of hydrogen can serve as an explanation for how heat easily penetrates from the core region of giant planets into its outer layers and then leaves the planet, radiating into the abyss of outer space. And secondly, the electrical properties and conductivity of the "dark" hydrogen can explain some of the subtleties of the formation of magnetic fields of gas giant planets. Some theoretical works indicate that in principle, under physical conditions in the bowels of Jupiter and Saturn, a state of high-temperature superconductivity can be realized, which is the source of a powerful magnetic field.

4. Conclusion

On the basis of the observational data on the study of quadrupole lines H_2 (4-0) along different parts of the Jovian disk along its meridian, it was established that the pressure, temperature and quantity of molecular hydrogen do not obey any monotony. The observed temperature differences and the content of molecular hydrogen are accompanied by IR emission in the details of Jupiter. This behavior of the pressure and temperature values at the depth of the formation of molecular hydrogen lines may be due to various features of the thermal radiation of the planet coming from the lower layers, i.e. the release of energy during the conversion of hydrogen over the liquid layer. The release of energy in various parts of the Jupiter disk can be caused by a weak spontaneous conversion of orthohydrogen to parahydrogen, occurring in the deep layers of Jupiter, as a thin layer above the liquid molecular hydrogen, even in the absence of a catalyst (the catalyst accelerates this process). The process of the conversion, occurring in different belts, zones and in different depths, has different speeds and spatial scales and depends on the temperature and the amount of orthohydrogen.

References

Slipher V.M. 1909. The Spectrum of the Major Planets // Lowell. Observ. Bull., No. 42, pp. 231-238.

Slipher V.M. 1933. Spectrographic studies of the planets // Monthly Notices Roy. Astron. Soc. V. 93, pp.657-668.

Wildt R. 1932. Absorptions spektrum und Atmosphären der großen Planeten. (Note on the spectra of Jupiter and Saturn) // Veroff. Univ. Sternwarte Gottingen, N. 22. pp. 171-180.

Kuzmin A.D., Lasovsky B.Ya. 1971. Measurement of Uranus radio emission at 8.22 mm // Icarus, V. 14, №2, pp.196-197.

Adel A., Slipher V.M. 1934a. On the Identification of the Methane Bands in the Solar Spectra of the Major Planets Phys. Rev., V. 46, N.3, pp.240-241.

Adel A., Slipher V.M. 1934b. The Constitution of the Atmospheres of the Giant Planets, Phys. Rev.,V. 46, N.10, pp.902-906.

L.V. Ksanfomaliti, 2012. Solar system. (Ed. by V.G.Surdin), Fizmatlit: Moscow., p. 398.

Herzberg G.1938. On the possibility of detecting molecular hydrogen and nitrogen in planetary and stellar atmospheres by their rotation-vibration spectra. Ap.J., V. 87, pp. 428-437.

Herzberg G., 1952. Spectroscopic evidence of molecular hydrogen in the atmospheres of Uranus and Neptune, V. 115, N.3, pp.337-340.

Kuiper G.P., 1949. New absorptions in the Uranus atmosphere. V. 109, pp.540-541.

Kiess C.C., Corliss C.H. and Kiess H.K.1960. High-dispersion spectra of Jupiter //Ap.J., V.132, pp.221-231.

Spinrad H., Trafton L.M., 1963. High-dispersion spectra of outer planets: I. Jupiter in the visual and red // Icarus, V.2, N. 1, pp. 19-28.

Mikailov Kh.M., Khalilov, V.M., Alakbarov, I.A. 2005, Echelle-spectrometer of the focus Cassegrain of the 2-m telescope of ShAO. Circular of ShAO, V. 109, pp.21-29.

Mikailov Kh.M., Musayev F.A. and et all., ShaFES: Shamakhy fibre echelle spectrograph, 2017. V.12, N.1, pp.4-27.

Encrenaz T. and Owen T., 1973, New observations of the hydrogen quadrupole lines on Saturn and Uranus. Astron. and Astrophys., V.28, pp.119-124.

Smith W.H., Conner C.P., Simon J., Schempp W.V. and W.Macy, The H_2 4-0 S(0,1 and 2) quadrupole features in Jupiter). Icarus, 1989, V.81, pp.429-440.

Flasar F.M., Global dynamic sand thermal structure of Jupiter's atmosphere , Icarus, 1986 , V.65 , pp.280-303.

Teyfel V.G., 1980. Optical properties of the atmospheres of Jupiter and Saturn. Doctoral Thesis. Almata. p.530.

Conrath B.J., Gierasch P.J. and Leroy S.S., 1990 . Temperature and circulation in the stratosphere of the outer planets, Icarus, V.83, pp. 255-281.

Mecke R., 1925. Zur Struktur einer Klasse von Bandenspektra, Z. Physik. V. 31, pp.709-712.

Heisenberg W. , 1926. Mehrkörperproblem und Resonanz in der Quantenmechanik, Z. Physik. V 38, N. 6–7, pp.411-426.,

Heisenberg W., 1927. Mehrkörperprobleme und Resonanz in der Quantenmechanik. II Z. Physik. V.41, pp. 239-261.

Hund F., 1927. Zur Deutung der Molekelspektren. II, Zeitschrift für Physik, V.42. N. 2-3, pp. 93–120.

Dennison D.M., 1927. A note on the Spesific heat of the hydrogen molecule , Proc. Roy. Soc, Lond. , V. 115, pp. 483-.487

Eucken A, 1912. Die Molekularwarme *des Wasserstoffs bei tiefen Temperaturen, Sitz.ber. Preuss. Akad. Wiss. (Berlin), pp. 141-151.*

Hori T., 1927 , Über die Analyse des Wasserstoffbanden spektrums im äußersten Ultraviolett, Z.Physik, V.44, pp.834 -854.

Bliesner R.M., 2013. Parahydrogen-Orthohydrogen Conversion for Boil-off Reduction from Space Stage Fuel Systems. A thesis for the degree of Masters of Science. Washington State University School of Mechanical and Materials Engineering.

Fermi E., Rasetti F,1931. Über den Ramaneffekt des Steinsalzes. Zeitschrift für Physik, V. 71, N 9–10, pp 689-695.

Jupiter imaged using the VISIR instrument on the VLT. Retrieved from https://www.eso.org/public/images/eso1623a/

Zones and belts on Jupiter. Retrieved from https://www.harding.edu/lmurray/113_files/html/h_jovian/sld010.htm

Wigner E, Huntington H. B.J., 1935. On the Possibility of a Metallic Modification of Hydrogen. Journal of Chem. Phys.V. 3, pp.764-770.

Dias R.P. and Silvera I.F.,2017, Observation of the Wigner-Huntington transition to metallic hydrogen , Science ,V.355, N.6326. pp. 715-718 .

Nellis W.J., 2000. Metallization of fluid hydrogen at 140 GPa (1.4Mbar) by shock compression, High Pressure Research: An International Journal, V.16, N 5-6, pp.291-303.

PHOTOMETRY OF AN UNUSUAL SMALL DISTANT OBJECT 2016 ND21

Hromakina T. A.[1], Velichko S. F.[1]Belskaya I. N.[1], Krugly Yu. N.[1], SergeevA.V.[2,3]

[1]Institute of Astronomy, V.N. Karazin Kharkiv National University, Sumska str. 35, Kharkiv 61022, Ukraine;

[2]IC AMER, National Academy of Sciences of Ukraine, Akademika Zabolotnoho str. 27, 03680 Kyiv, Ukraine;

[3]Terskol Branch of INASAN, Russian Academy of Sciences, 81, Elbrus ave., ap. 33, Tyrnyauz, Kabardino-Balkaria Republic, 361623, Russian Federation.

E-mail: hromakina@astron.kharkov.ua

Abstract

We present the first-ever measurements of the surface colors and rotational properties of a recently discovered distant object in an unusual orbit 2016 ND21. In 2017, this object was close to its perihelion, which allowed us to observe it with a 2.0-m telescope at the Peak Terskol observatory. Broadband photometric observations of 2016 ND21 were carried out in October and December of 2017 in standard BVR filters of the Johnson-Cousins photometric system. During our observations, we did not detect any cometary activity. We found the rotational period of 17.53±0.02 hr, while another a little longer value of 17.65±0.02 hr is also possible. Assuming an equatorial aspect of observations, a peak-to-peak amplitude of A = 0.31±0.05 mag (or even higher since only one maximum and one minimum were well-measured) corresponds to an elongated body with an axis ratio a/b ~1.3. The lightcurve behavior indicates a complex, possibly non-convex, shape of this object. The visible absolute magnitude is H_V =12.4±0.1 mag, which was estimated by using the linear phase slope 0.04 mag/deg as the most probable value from our observations. This phase slope suggests a low-albedo surface of 2016 ND21. Assuming a surface albedo in the range of 0.04-0.10, the size of 2016 ND21 should be about 15-23 km. From our multi-color observations, we determined surface colors V-R = 0.69±0.04 mag, B-R = 1.79±0.08 mag, and B-V = 1.10±0.08 mag. The measured colors indicate an extremely red surface of this object. A very red surface is unusual

for comets, which is in agreement with the fact, that no cometary activity was detected for 2016 ND21. The B-R color is higher than the typical B-R colors of the red D-type asteroids, but it is consistent with colors of the red Centaurs and TNOs classified as RR type in TNOs classification. This result gives a first evidence of a possible outer belt origin of this small body.

Keywords: *Minor planet, photometry, lightcurve, rotational period, surface colors*

Introduction

Recently discovered small Solar system object 2016 ND21 has an unusual high-eccentric (e = 0.55) and highly inclined (i = 21.83 deg) orbit with a major semi-axis a = 8.45 AU. Following the classification described by Gladmanet al. (2008), this object with a perihelion q = 3.76 AU and a Tisserand parameter T_J=2.584 should be classified as a cometary body. However, the orbit's inclination of 2016 ND21 is too high for a Jupiter Family Comet member (e.g. Lowry et al. 2008), and no cometary activity was discovered for this object so far. Jupiter Family Comets, although being a dynamically distinct group, are similar to some Centaurs, small bodies orbiting between Jupiter and Neptune. The object 2016 ND21 cannot be classified as a Centaur because a perihelion of its orbit is in asteroid belt. In the Minor Planetary Center (MPC) catalog (https://minorplanetcenter.net/iau/lists/Unusual.html), 2016 ND21 is classified as a distant object with an unusual orbit. Its aphelion is Q=12.70 AU. There are only a few discovered objects of this kind, and one of them is 2008 SO218, that is considered to be in a retrograde resonance with Jupiter (Morais et al. 2013).The objects at such unusual orbits are believed to be captured by Jupiter and can originate from both, the inner or the outer parts of our Solar system. Studying the physical properties of these objects can shed a light on their origin. No size or albedo measurements are available for 2016 ND21. In this paper, we present the first-ever measurements of the surface colors and rotational properties of this object.

Observations and data reduction

The observations of 2016 ND21 were carried out during six nights in October and December of 2017 at the 2.0-m telescope of the Peak Terskol observatory. The telescope is equipped with a 2048 × 2048 CCD camera FLI PL-4301, that has a pixel scale 0.31arcsec per pixel, resulting in a field of view 10.7 × 10.7 arcmin.

Observations were performed in BVR filters of the standard Johnson-Cousins photometric system. At the moment of observation, the object was near its perihelion and had visible magnitude within the range 18-19 mag. During each observation run, we also acquired bias, dark, and flat-field images. Table 1 shows the observational circumstances, namely heliocentric (r) and geocentric (Δ) distances, Solar phase angle (α), mean values of reduced magnitudes in B, V, and R filters, and a total observing time (T_{obs}) in hours.

Table 1. Observational circumstances and measured reduced magnitudes in BVR filters for 2016 ND21

UT time	r, AU	Δ, AU	α, deg	B(1, α), mag	V(1, α), mag	R(1, α), mag	T_{obs}, hr
2017 10 12.80	3.770	2.993	10.65	-	-	-	2.4
2017 10 13.77	3.771	3.001	10.64	-	-	-	6.1
2017 10 20.66	3.775	3.065	11.79	-	12.790±0.03	12.023±0.03	1.0
2017 12 10.72	3.816	3.727	14.94	14.117±0.08	13.022±0.05	12.218±0.03	3.9
2017 12 12.76	3.818	3.756	14.91	14.258±0.08	13.190±0.04	12.437±0.04	2.9
2017 12 13.75	3.819	3.770	14.89	14.121±0.09	13.065±0.05	12.223±0.05	0.8

Data reduction was made using MaximDL software package in the standard way, which included bias and dark-field subtraction from the raw data and flat-field correction. Differential photometry was done using the ASTPHOT package that was developed at DLR by S. Mottola (Mottola et al. 1995).The accuracy of differential photometry was about 0.02-0.03 mag in V and R filters and

~0.07 in B filter. For two first nights in October, only differential photometry was performed. However, the same reference star was used to connect those two lightcurves. On October 20, December 12 and 13, the standard star GD246 from Landolt catalog (Landolt 1992) was observed, which allowed us to perform absolute calibrations for four out of six nights. The uncertainty of absolute photometry was 0.04 mag in V and R filters, and 0.08 mag for B filter. Thus, an absolute calibration and using the same reference stars for the differential photometry allowed us to exclude an arbitrary shift of the data while searching for the rotation period.

Results and discussion

We inspected the obtained images of 2016 ND21 on the existence of cometary coma by comparing its profile with those of the field stars. No broadening of the object's PFS that could suggest a cometary activity was detected.

The search for a rotational period was made following the Fourier analysis technique described in Harris& Lupishko (1989) and Magnusson (1990). The observations during two consistent nights on 12 and 13 of October revealed that the period should be longer than ~16 hr. Using all obtained data, we found the rotation period P = 17.53±0.02 hr. We also noted that another value of period 17.65±0.02 hr is also possible. The composite lightcurve with period P=17.53±0.02 hr is shown in Fig. 1. The estimated amplitude is A = 0.31±0.05 mag, but it can be even higher since two extrema of the lightcurve are not covered at their extreme values. The measured amplitude corresponds to an elongated body with an axis ratio a/b ~1.3, if we assume an equatorial aspect of observations and ellipsoidal shape. However, the lightcurve has a rather unusual behavior with a broad minimum and a sharp maximum, which suggest that 2016 ND21 have not a simple ellipsoidal shape, but rather a complex, possibly non-convex, one.

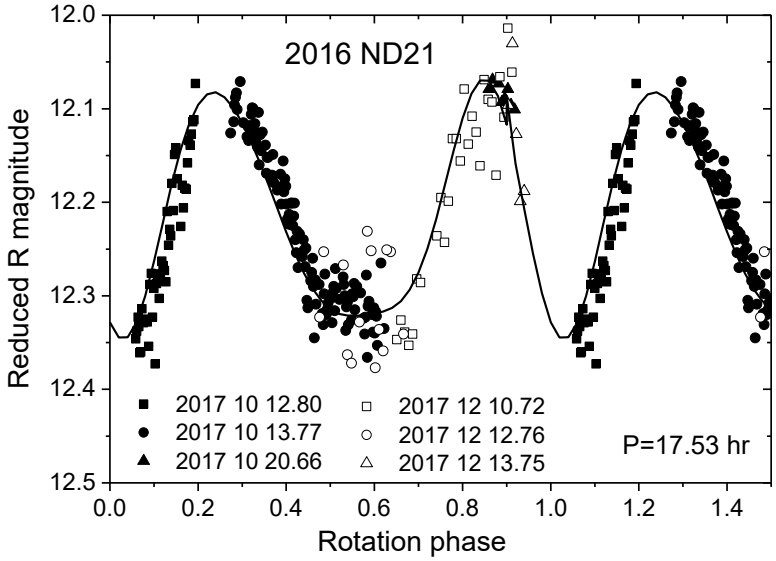

Fig. 1. Composite lightcurve of 2016 ND21 with rotational period 17.53 hr.

From our multi-color observations, we determined surface colors V-R = 0.69±0.04 mag, B-R = 1.79±0.08 mag, and B-V = 1.10±0.08 mag. The obtained colors reveal extremely red surface of this object. Comet nuclei tend to have more neutral colors (average V-R=0.49±0.12 mag compared to average V-R=0.59±0.08 mag for Trans-Neptunian objects (TNOs); Snodgrass et al. 2006), that according to Jewitt (2002) may be due to resurfacing caused by comet activity. In this regard, the absence of cometary activity of 2016 ND21 is in agreement with its very red surface. The B-R color is higher than a typical color of the red D-type asteroids (B-R = 1.22±0.09; Bus & Binzel 2002, Fornasier 2007), but falls within the color range of red Centaurs and TNOs classified as RR type in TNOs' classification (Barucci et al. 2005).We converted the measured colors of 2016 ND21 to spectral reflectance and compared them with the average spectra for D-asteroids and RR Centaurs and TNOs. Fig. 2 presents mean RR-type spectrum based on N=11 objects (Merlin et al. 2017) and mean D-type spectrum acquired using N=9 asteroids (Bus & Binzel 2002) in comparison with our data. A similarity of spectral slope of 2016 ND21 to red Centaurs and TNOs gives a first evidence of a possible outer belt origin of this object.

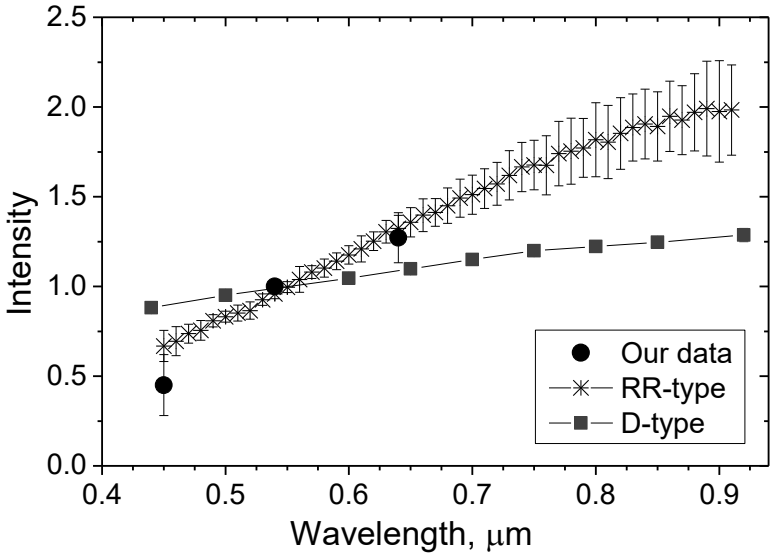

Fig. 2. Comparison of our data with mean RR-type (Merlin et al. 2017) and D-type (Bus & Binzel 2002) spectra.

Our data covered the phase angle range from 11.8 to 14.9 deg. We tried different phase slope coefficients while building the composite lightcurve and found that the most probable value is about 0.04 mag/deg, which is characteristic to a dark surface (see e. g. Belskaya & Shevchenko 2000). Using this phase coefficient and assuming linear phase-angle dependence, we estimated a value of visible absolute magnitude H_V=12.4±0.1 mag. This value is in a good agreement with that from MPC catalog (H_V ~12.3 mag). In assumption of a low albedo surface (0.04-0.1), the diameter of 2016 ND21 will be from ~15 km to ~23 km.

Conclusions

We report results of the first photometric investigation of the unusual distant object 2016 ND21. Although this object has a cometary orbit, as per our data it does not reveal any signs of cometary activity. Two values of rotational periods P = 17.53±0.02 hr and P = 17.65±0.02 hr were found, the former being more preferable. The unusual behavior of the lightcurve suggests a complex and possibly non-convex shape of 2016 ND21. Assuming an equatorial aspect of observations, the peak-to-peak lightcurve amplitude A=0.31 mag corresponds to an elongated body with axis ratio a/b ~1.3. The object 2016 ND21 has a very red surface similar to RR type in TNOs' classification, which suggests a possible outer belt origin of this small body. We defined its visible absolute magnitude

H_V =12.4±0.1 mag using the linear phase slope 0.04 mag/deg as the most probable value from our observations. The phase slope suggests a low-albedo surface of this object. In assumption of an albedo from 0.04 to 0.1, the size of 2016 ND21 should be within 15-23 km.

Thus, our BVR photometric observations of a small distant object 2016 ND21 at an unusual orbit suggest a very red dark surface similar to some red Centaurs and TNOs, elongated, most probably non-convex shape, and rather slow rotation.

References

1. Barucci M. A., Belskaya I. N., Fulchignoni M. Birlan M. (2005). Taxonomy of Centaurs and Trans-Neptunian objects. The Astronomical Journal, 130, 1291–1298. Doi: 10.1051/0004-6361/200913654
2. Belskaya I. N. and Shevchenko V. G. (2000). Opposition effect of asteroids. Icarus, 147, 94-105. doi:10.1006/icar.2000.6410
3. Bus, S.J., Binzel, R.P.(2002). Phase II of the Small Main-Belt Asteroid Spectroscopic Survey. A Feature-Based Taxonomy. Icarus, 158, 146-177. doi:10.1006/icar.2002.6856
4. Fornasier S., Dotto E., Hainaut O., et al. (2007). Visible spectroscopic and photometric survey of Jupiter Trojans: Final results on dynamical families. Icarus, 190, 622–642. doi:10.1016/j.icarus.2007.03.033
5. Gladman, B., Marsden, B. G., & Van Laerhoven C. (2008).Nomenclature in the Outer Solar System. The Solar System beyond Neptune, M. A. Barucci, H. Boehnhardt, D. P. Cruikshank, and A. Morbidelli (eds.). University of Arizona Press, Tucson. pp. 43–57.
6. Harris A. W. and Lupishko D. F. (1989). Photometric lightcurve observations and reduction techniques. In: Binzel, R.P., Gehrels, T., Matthews, M.S. (Eds.), Asteroids II. University of Arizona Press, Tucson, pp. 39–53.
7. Jewitt D. C. (2002). From Kuiper Belt object to cometary nucleus: The missing ultrared matter. Astron. J., 123, 1039–1049. doi:10.1086/338692

8. Landolt, A. U. 1992. UBVRI photometric standard stars in the magnitude range 11.5–16.0 around the celestial equator. Astron. J. 104, 340– 371. doi:10.1086/116242
9. Lowry S., Fitzsimmons A., Lamy P., Weissman P. (2008). Kuiper Belt Objects in the Planetary Region: The Jupiter-Family Comets. The Solar System beyond Neptune, M. A. Barucci, H. Boehnhardt, D. P. Cruikshank, and A. Morbidelli (eds.). University of Arizona Press, Tucson. pp. 397-410.
10. Magnusson P. and Lagerkvist C.-I. (1990). Analysis of asteroid lightcurves. I. Data base and basic reduction. Astronomy & Astrophysics Supplement Series, 86, 45–51.
11. Merlin, F.; Hromakina, T.; Perna, D.; Hong, M. J.; Alvarez-Candal, A. (2017). Taxonomy of trans-Neptunian objects and Centaurs as seen from spectroscopy. Astronomy & Astrophysics, 604, 86-94. doi:10.1051/0004-6361/201730933
12. Morais M. H. M. and Namouni F. (2013). Asteroids in retrograde resonance with Jupiter and Saturn. Monthly Notices of the Royal Astronomical Society: Letters, 436, 30-34. doi:10.1093/mnrasl/slt106
13. Mottola, S., G. De Angelis, M. Di Martino, A. Erikson, G. Hahn, and G. Neukum G.(1995). The near-Earth objects follow-up program: First results. Icarus, 117, 62–70. doi:10.1006/icar.1995.1142
14. Snodgrass C., Lowry S. C.d Fitzsimmons A. (2006). Photometry of cometary nuclei: rotation rates, colours and a comparison with Kuiper Belt Objects. Monthly Notices of the Royal Astronomical Society, 373, 1590–1602. doi: 10.1111/j.1365-2966.2006.11121.x

Astronomy & Astrophysics (Caucasus) 4, (2018)

LUNI-SOLAR TIDAL SYNCHRONIZATION EXAMPLE AS A MODEL APPROACH FOR THE STUDY OF GEOPHYSICAL AND BIOLOGICAL PHENOMENA CORRELATION WITH ASTRONOMICAL CYCLES

Lev Gheonjian

Department of Electrical and Electronics Engineering, Ivane Javakhishvili Tbilisi State University, Tbilisi, Georgia
Email: levi.geonjiani@tsu.ge

Tamar Paatashvili

E. Kharadze Abastumani Astrophysical Observatory, Ilia State University, Tbilisi, Georgia
[1]Department of Electrical and Electronics Engineering, Ivane Javakhishvili Tbilisi State University, Tbilisi, Georgia
Email: tamari.paatashvili125@ens.tsu.edu.ge

Abstract

The model approach of relaxation oscillator synchronization was considered for the study of correlation of some geophysical and biological phenomena with astronomical cycles. In case of cyclical phenomena, it is sufficient to identify the physical variables of the interaction and show the ability of the phase self-tuning of the synchronized phenomenon or object. More complicated is a system of interacting events similar to relaxation oscillator storing the energy during the time and its discharge, i.e. an earthquake, an avalanche, sharp exacerbation of a disease, or an act of aggression, happens suddenly, when the load parameter reaches its critical value. Such a relaxation oscillation behavior often arises during the self-organized criticality processes.

It is shown that external periodical factor can synchronize relaxation oscillators discharge moments. The analyses demonstrate the "gaps" - the time intervals when discharges are absent, and also demonstrate that the width of the gap depends on stress (load) growth velocity. Strong, slowly growing synchronized oscillators demonstrate wider gaps; a fast growth gives narrow gaps or modulation of distribution. Astronomical periodicities, as global synchronizing periodical factors, may be determined by the analysis of discharges distributions.

The validity of approach was tested and confirmed with a laboratory experiment.

[1]PhD Student

The method was applied for the Caucasus strong earthquakes with $M>6.0$ and reveal a set of tidal components with a clear astronomical meaning – the positional relationship of the Sun, the Earth and the Moon and periodicities of their orbital movement.

Key words: *synchronization, tide, astronomical cycles, self-organized criticality***.**

1. Introduction

Our objective is to thoroughly understand the concept of synchronization and routine methodologies widely used in electrical engineering and apply it to the study of synchronization processes of some geophysical, biological and some social phenomena with astronomical cycles.

We consider the synchronization as the origin of frequency-phase dependence between physically slightly coupled periodic processes. Synchronization of oscillators is a ubiquitous phenomenon in many areas of science and engineering (Blechman, 1971; Pikovsky, Rosenblum and Kurth, 2003). A synchronization phenomenon depends on an intrinsic mechanism of oscillation as well as on the nature of coupling and it is thoroughly studied for a variety of oscillators. In case of cyclical phenomena, it is sufficient to identify the physical variables of the interaction and show the ability of the phase self-tuning of the synchronized phenomenon or object.

More complicated is a system of interacting events similar to relaxation oscillator storing the energy during dozens or hundreds of years, even for days or hours. Relaxation oscillators have the properties quite different from that of non-relaxation ones. Relaxation oscillators need only few or even one cycle to synchronize. Mathematical description of the relaxation oscillator synchronization process is simple, vivid, and was solved more than half a century ago in engineering (Meerovich and Zelichenko, 1954). One can consider some events as an analogue of nonlinear relaxation oscillator, storing the energy during tens or hundreds of years, even for days or hours. For example, “discharge” of stored earthquake energy happens suddenly, when tension in rocks exceeds friction resistance on the fault. We consider the synchronization of a series of relaxation processes by an external quasi-harmonic factor, as the origin of dependence between time series of events and a well-expressed phase of external periodic processes. Close to the breaking limit, the relaxator becomes sensitive even to weak external disturbances. The additional tension caused by varying external factors contributes to earlier discharge of the relaxation oscillator. In seismically active regions, varying external factors operate as synchronizers of earthquake release moments (Lursmanashvili et al., 2010). It should be mentioned that earthquakes as relaxation oscillators cower a wide dynamic range and different synchronizers may affect quakes of different energetic classes.

The methods detecting synchronizers solve event prediction problems. Synchronizers include global phenomena such as tides, a set of geophysical disturbances caused by solar activity and variations of Earth rotation rate. Tides, solar activity, as well as peculiarities of Earth orbital movement participate in Earth rotation.

There are at least three directions in which progress can be made using the proposed approach:

I. The first direction related to the synchronization of large-scale social phenomena is still waiting for its researcher. Although the task was formulated almost a century ago (Chizhevsky, 1924), apparently the possibility of its solution appeared only after understanding the fundamental phenomenon of self-organizing criticality (Bak et al., 1988, Bak 1996). We consider the possibility of synchronizing the processes of self-organizing criticality (Gheonjian et al., 2018b).

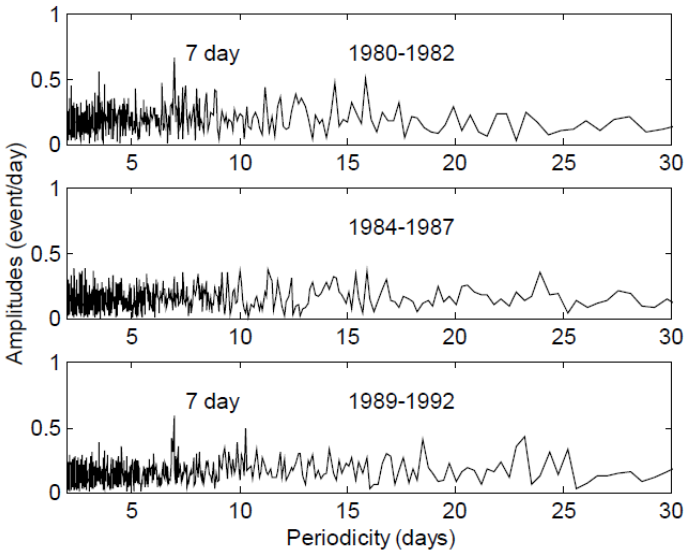

Fig. 1. About-weakly (circaseptan) resonance of human mortality from myocardial infarction with solar activity phase (1980-1982 and 1989-1992) caused by circaseptans of interplanetary magnetic field (Khomeriki et al., 1998)

II. The second direction relates to the synchronization of biological rhythms. Recently published comprehensive treatise of Otsuka et al. (2016) is a fundamental overview of all advances in this field of study. Detected about-weakly (circaseptan) resonance of human mortality from myocardial infarction with solar activity phase caused by circaseptans of interplanetary magnetic field (Khomeriki et al, 1998, see Fig. 1) should be highlighted in this review as a case of synchronization of the biological relaxation processes.

Our approach is fully applicable to this case and to all cases of exacerbations of the disease. In this publication, we present all the methodological considerations and approaches that allow us to reconsider many of the results presented in the book by Otsuka et al. (2016).

III. Luni-solar tide synchronization study example may be used as a model approach for the pointed problems of geophysical phenomena correlation study with global synchronizer astronomical cycles (Lursmanashvili et al., 2010). In this direction, as regards the field of seismology, it became possible to achieve a significant understanding of the processes taking place and to proceed with the implementation of other research instrumental support projects (Gheonjian et al., 2017a, 2017b, 2018a, 2018b).

The problem is very complicated. The lack of a clear understanding of the essence of the phenomenon often leads to contradictory results. As an example, some of researchers have found an external tidal astronomical synchronizing influence on earthquakes (Allen 1956; Hoffman 1961; Tamrazian 1968; Ryall et al. 1968; Lursmanashvili, 1973; Heaton 1975; Palumbo 1986; Dietrich,

1987; Weems and Perry 1989; Nikolaev, 1994; Lursmanashvili, 2001; Perfettini and Schmittbuhl, 2001; Custodio et al., 2002; Sobolev and Ponomarev, 2003; Scholz, 2003; Wang et al., 2004; Lursmanashvili et al., 2010, Metivier et al., 2009, Tanaka et al., 2010), others refuse it (Knopoff 1964; Simpson 1967; Shlien 1972; Vidale et al., 1998; Beeler and Lockner, 2003, Tanaka et al., 2006, Tormann et al., 2015).

There is a valid cause to further develop the concept to study this region as an object of nonlinear dynamics (Matcharashvili et al., 2000). Laboratory model experiments confirm the idea to apply the synchronization concept to seismicity (Chelidze and Lursmanashvili, 2003; Chelidze et al., 2005, 2006).

2. The model approach for revealing external periodical factors of relaxation oscillator synchronization

Let consider "gap" method (Lursmanashvili et al., 2010) for revealing external synchronizing periodical factor from analysis of relaxation oscillators discharges distributions.

We present a simple model describing the principles of relaxation oscillator synchronization approach used by us. Let the charge of the oscillator, or stress in the system $P(t)$ increase monotonically and undergo the influence of small external stress (or forcing) with amplitude, frequency and initial phase denoted as a, $\varpi = 2\pi / T$, φ, respectively. T is the period of external oscillating stress. The resulting stress may be represented as

$$P_c(t) = P(t) + a\sin(\varpi t + \varphi). \quad (1)$$

The discharge stage of oscillator cycle will start at the critical moment when the resulting stress will reach the breaking value of medium P_m, or

$$P_c(t) = P(t) + a\sin(\varpi t + \varphi) = P_m. \quad (2)$$

Assume that at the final stage of discharge preparation, from the time moment $t = t_0$ and corresponding stress P_0, the stress increases linearly as

$$P(t) = b(t - t_0). \quad (3)$$

As a result of this assumption, we obtain the following expression:

$$P_0 + b(t - t_0) + a\cos(\varpi t + \varphi) = P_m, \quad (4)$$

or the equation describing the relation between the time-dependent linearly increasing stress and harmonically oscillating external stress:

$$b(t - t_0) = P_m - P_0 - a\cos(\varpi t + \varphi). \quad (5)$$

The initial moment of energy integration process may be unknown. If we examine a set of *N* different start moments, separated by step ε, and, at least, covering the time interval equal to the period of external oscillating stress, we will obtain *N* equations

$$b(t - t_0 + \varepsilon n) = P_m - P_0 - a\cos(\varpi t + \varphi), \ n = 0,1,2,...N \quad (6)$$

and by solving them, we will be able to determine all possible time moments of discharges caused by external factor and positioned inside the time interval corresponding to the period of external factor. The distribution of these moments inside the period corresponding to external oscillator time parameters will represent the synchronizing properties of the phenomenon described by this model.

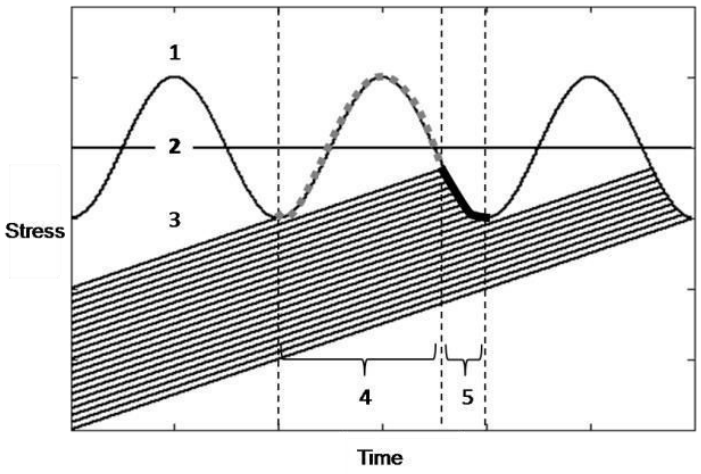

Fig. 2. The principle of discharge synchronization by external forcing: external synchronization of relaxator by quasi periodic modulation factor (1) of stress near the breaking limit value of charge process (2). Each relaxator (3) may exist and be charged inside time interval (4), and discharged in time interval (5).

As one can see, Fig. 2 shows the external oscillating stress represented by the right side of equation (6), and the family of lines represented by the left side. They correspond to linearly increasing stress processes started at different time moments in the past and progressing inside the time period of external stress near the final stage of relaxation oscillator evolution. It is obvious that the curve and line intersection moments correspond to possible discharge moments, in our cases – time moments of earthquakes, avalanches, social or biological catastrophes. One can obviously see the time "gap", or a set of time moments when discharges are prohibited. It is also obvious that the width of the gap depends on the stress growth velocity. In the general case, the width is determined by the velocity in relation to the external factor frequency. If one examines the distribution of catastrophes inside the period of external factor, it turns out that strong, slowly and longtime growing catastrophe triggered by a stable external factor, will demonstrate wider gaps. Fast growth causes narrow gaps or modulation of distribution. Therefore, an analysis of discharge time distributions inside the forcing periods for different frequencies and detection of gaps or modulation is the way to the discovery of external synchronizing factors, which trigger discharges.

Fig. 3 demonstrates the distribution of discharge time moments inside the period of forcing and the corresponding solutions of equations. Let us introduce normalized variable $\tau = t/T$ and examine the distribution of roots of equation (6). The equation will be transformed to a simple form

$$A(\tau + n/N) = C - \cos 2\pi\tau, \ \ n = 0,1,2,...N, \tag{7}$$

where $A = b/a\varpi$ is the relative velocity of stress growth and $C = (P_m - P_0)/a$ is the constant determining the relative breaking point of relaxation oscillator.

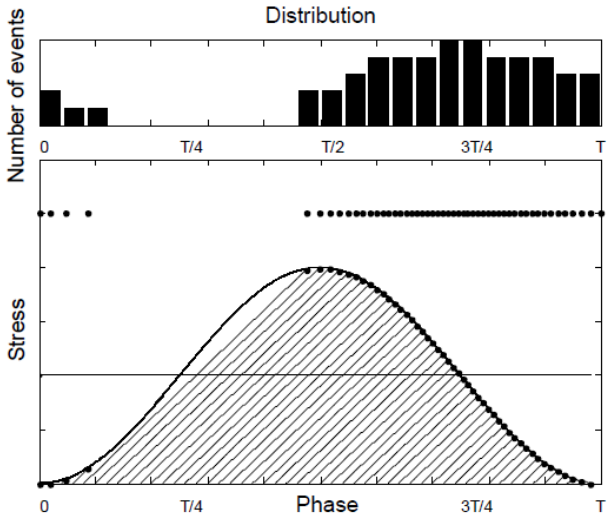

Fig. 3. Distribution of relaxation oscillator's discharge moments inside forcing period T and the corresponding solutions of equations

Parameter *A* determines the inclination of lines represented in Fig. 4. The figure illustrates four synchronization cases with different values of *A* and corresponding distributions. The increase of *A* causes a decrease of the width of gap where oscillator discharges are forbidden and causes a change of the corresponding distribution form, but the information on synchronizing factor is retained even in the case when the gap vanishes.

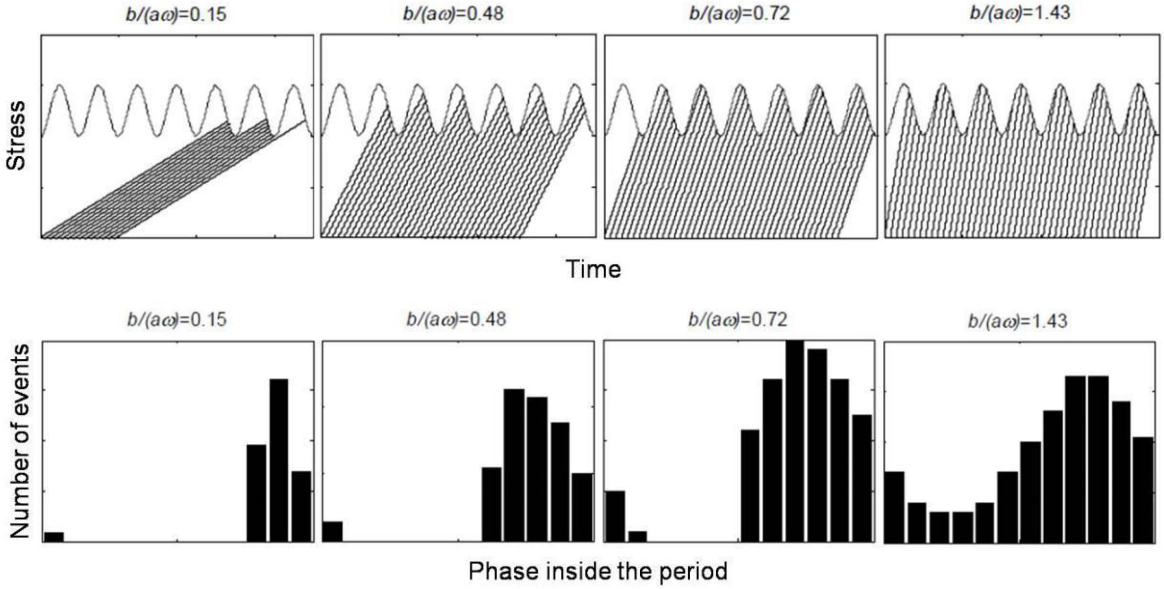

Fig. 4. Four relaxation oscillator synchronization cases with different values of relative velocity parameter A and oscillator discharge time moment distribution inside the period of external synchronizing harmonic factor.

The presented model shows the way to study and discover external factors synchronizing discharges. It is useful to examine the general diagnostic diagram, representing the roots of equation (7) for a set of values of parameter *A*. This diagram, shown in Fig. 5, demonstrates all the above-

mentioned properties of synchronization. The increase of A causes deterioration of the synchronization conditions. The gap area of the diagram – the root-free area decreases to zero, and for $A>1$ a discharge may occur for any value of phase. In this case, the information on external synchronizing factor remains in the roots' density variation and the minimum of density corresponds to the value of phase equal to $\pi/2$.

It should be mentioned that when we applying this approach in seismology, the seismoactive region should be examined as a set of relaxation oscillators with different physical properties being on different stages of evolution. The set of external harmonics, in reality quasi-harmonic synchronizers, is complicated too.

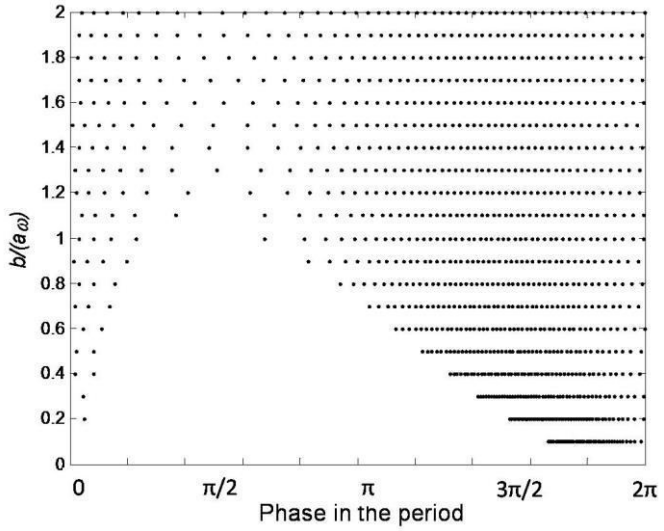

Fig. 5. Diagnostic diagram of relaxation oscillator synchronization.

The detection of external synchronizing demands careful discrimination and processing of data. The approach for the statistical estimation of the reliability of detected gaps in discharge time moment distributions, or their modulation, should be examined and proved as the necessary condition permitting to use the developed model.

Our case is typical for the application of approach, which uses binomial distribution. Expression (8) determines the probability to obtain ν equal results in the set of n probations:

$$P(\nu,n)=\frac{n!}{\nu!(n-\nu)!}p^{\nu}q^{n-\nu} \qquad (8),$$

where p is the probability to obtain the desired result in one probation, and $q=1-p$ is the probability to obtain undesirable result. If the relative gap width inside the period is $\Delta T/T$, one can estimate the probabilities to hit in gap and outside the gap. The corresponding probabilities for one probation are $\Delta T/T$ and $1-\Delta T/T$. If we examine the case of accidental gap existence, it means that for all n probations we obtain equal results for hitting in $1-\Delta T/T$ width interval. This means that $n=\nu$ and expression (8) becomes simpler:

$$P(n)=(1-\Delta T/T)^{n} \qquad (9)$$

For example, if $n=30$ and $\Delta T/T$ is equal to 0.1, 0.2 and 0.3, the corresponding probabilities of accidental appearance of gaps are 0.04, 0.001 and 0.00002. In this way, the gap method proves the

reliability of the developed synchronization. The appearance of enough wide gaps reliably reveals the existence of external synchronizing factor.

3. Testing the synchronization model approach in laboratory experiment

All these considerations and the validity of "gap" method to discover external synchronizing factors are tested in the model laboratory experiments (Chelidze and Lursmanashvili, 2003). It is well known that the slider-spring system displays stick-slip behavior. The goal of experiment was to prove the possibility of a nonlinear control of slip.

We also consider the possibility of synchronizing the processes of self-organizing criticality in laboratory experiment with rotating cylinder partially filled with sand (Gheonjian et al., 2018b).Our model and laboratory device is as simple as the models and experiments of self-organizing criticality (Bak, 1988; 1996) using the sand. In some experiments the criticality was studied with the help of a granular structure placed in a rotating cylinder (Feder, 1995; Jaeger and Nagel, 1992; Bretz et al., 1992).This approach is acceptable for us, because the modulation of a critical state can be carried out by modulating cylinder rotation speed.

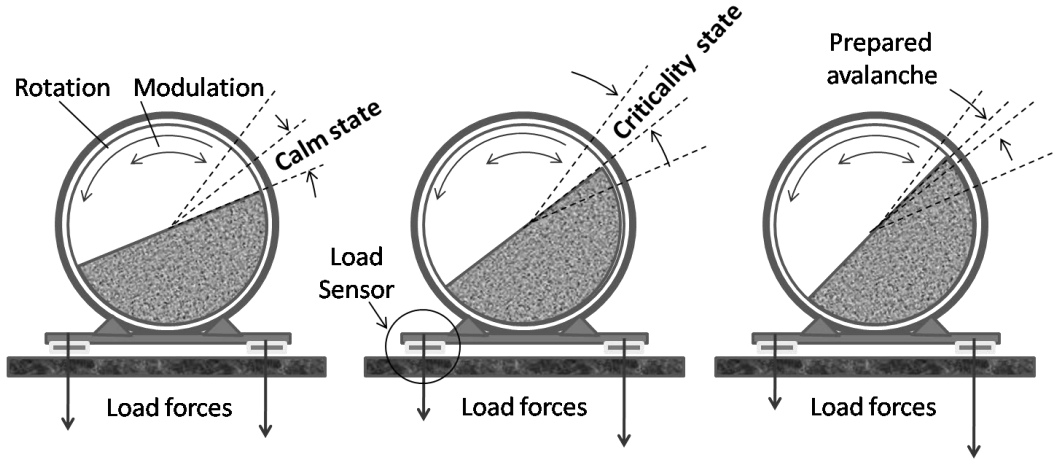

Fig. 6. Sand avalanche laboratory model for self-organized criticality parametric modulation study. Left figure state: a calm state of sand; load sensors signals difference increases with rotation and is modulated by a variable speed of rotation. Central figure: the sand reached the critical state; load forces difference corresponds to the experiment start, time series magnitude minimum value. Right figure: a self-organized criticality state; the avalanche grows and prepares for destruction; load forces difference reflects the growth process and avalanche mass.

Three different states of Fig. 6 represent our model of experiment (Gheonjian et al. 2018b). Left picture corresponds to the calm state of sand; load sensors signals difference increases with rotation and is modulated by a variable speed of rotation. Central picture corresponds to the sand having reached the critical state; load forces difference corresponds to the experiment start and time series minimum value. Right picture corresponds to the self-organized criticality state - the avalanche grows and prepares for destruction; the load forces difference reflects the growth process and avalanche mass.

In our experiment (see Fig. 7) the cylinder with sand has the diameter equal to 190 mm. Its

thickness is equal to 50 mm. The sand mass is 600 gram. To perform the rotation, cylinder has a 215-mm-diameter wheel with a friction coupling with a stepper motor. The contact is made by means of a rubber ring on the axis of the motor. The ring is in contact with the surface of the wheel.

The example of experiment time series without rotation modulation is represented in Fig. 8. Sand avalanches are discharges of different weights relaxators. Their distribution form corresponds to self-organized criticality and distribution characteristic to earthquake Gutenberg-Richter law.

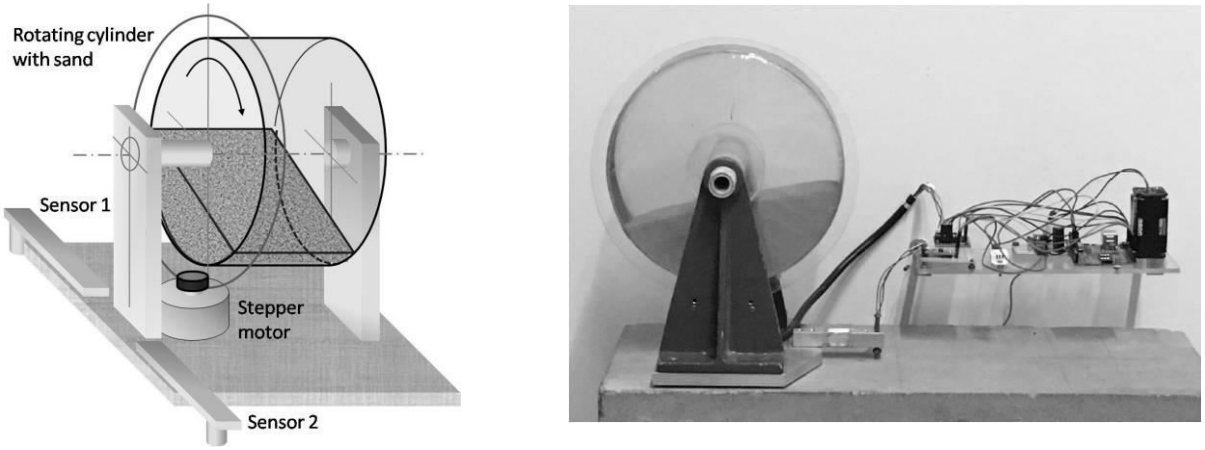

Fig. 7. Schematic representation and laboratory model. The inner surface is covered by sandpaper to exclude sand slipping. The cylinder with sand is driven by a stepper motor with a frictional transmission modulating the rotational speed of the cylinder.

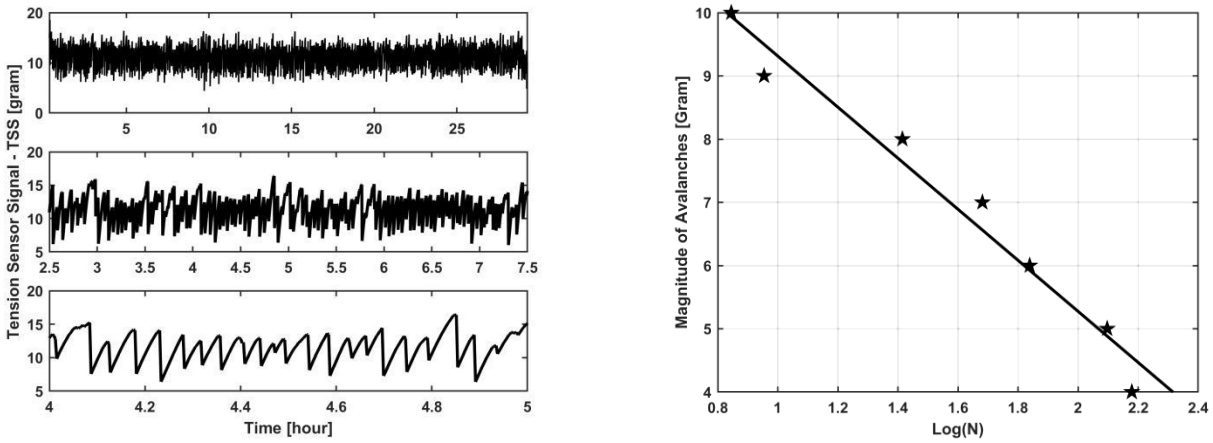

Fig. 8. Example of experiment time series without rotation modulation and corresponding distribution of avalanches characteristic similar to earthquake Gutenberg-Richter law (Gheonjian et al. 2018b).

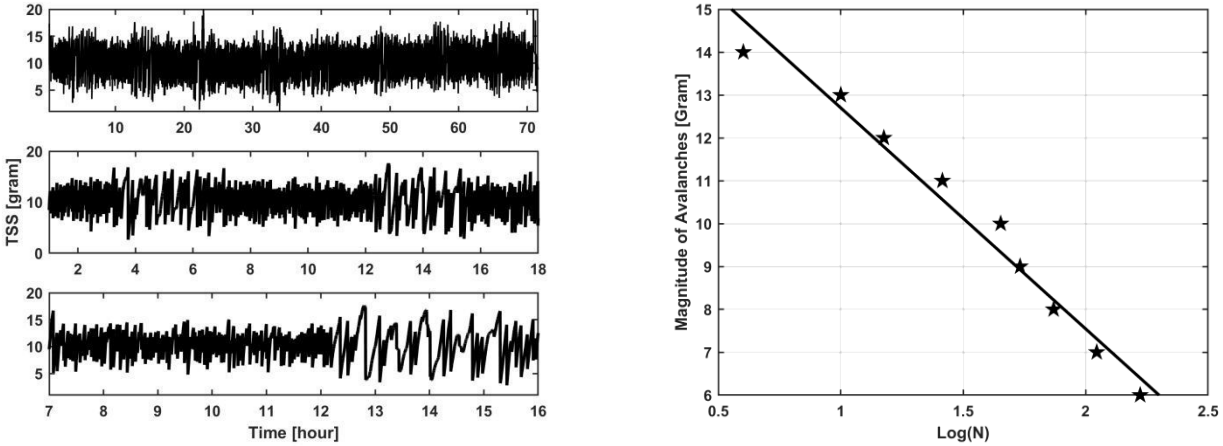

Fig. 9. Example of experiment time series with rotation modulation and corresponding distribution of avalanches characteristic similar to earthquake Gutenberg-Richter law (Gheonjian et al. 2018b).

The stepper motor rotates with velocity 1 step per 12 seconds. In the experiment modification without modulation, one revolution of the cylinder takes place in 6 hours. In experiments with modulation, we obtained a modulation period of 9 hours. This periodicity is represented in time series in Fig. 9. In experiment with modulation of cylinder rotation we also see the characteristic distribution of masses, but speed slowing contributes to the appearance of more massive avalanches.

In this modification of experiment one can obviously see the existence of avalanche triggering synchronization mechanism. The process represented in Fig. 10 is in full accordance with concept represented in Fig. 2.

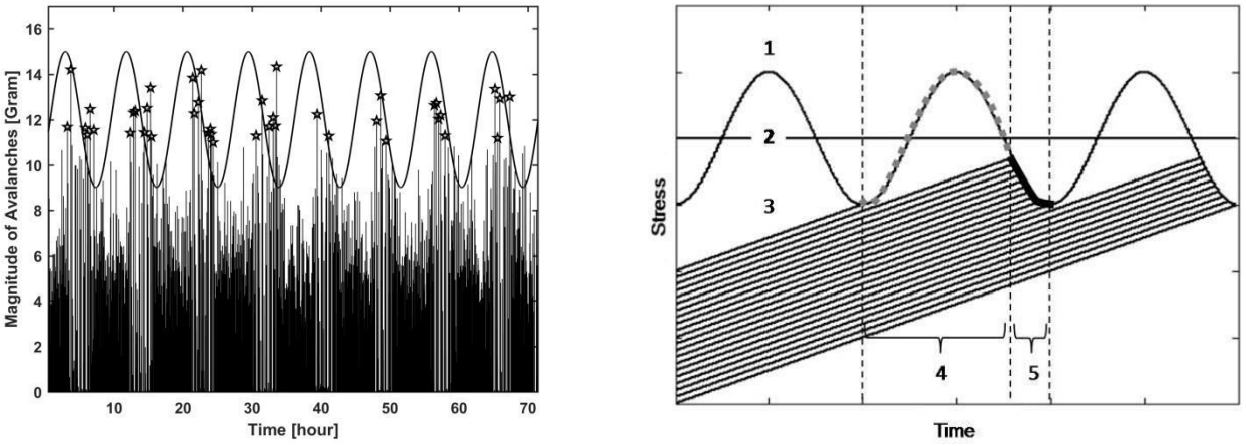

Fig. 10. The evidence of avalanche triggering synchronization mechanism existence. Experiment results correspond to basic considerations presented in section 2.

The experiment indicates the existence of a class of phenomena of self-organized criticality with parametric modulation of criticality conditions. Our laboratory model clearly demonstrates the existence of a specific class of phenomena of self-organizing criticality whose behavior can be partly predicted if the phenomenon of modulation exists and if the frequency of modulation of the physical variable responsible for the critical state is known.

The synchronization and triggering factor was not taken into account earlier in the study of self-organized criticality dynamics.

4. Example of application of the model approach - luni-solar tidal synchronization of strong Caucasus earthquakes

Investigations conducted during the last 30-40 years demonstrate some very deep, fundamental regularity in the statistics of time and space distribution of earthquakes that lead to the conclusion to study the earthquake phenomenon as a system-defined complex of connected and interacting events (Knopoff, 1996). The external synchronization influence phenomena come to light by the retro-statistical processing of earthquake catalogue.

The investigation of synchronizing effect of external factors in a certain region requires development of special methods, because catalogue data of earthquakes are presented as unequally-spaced sequences of phenomena. One of these methods, the "gap" method, has been represented above (Lursmanashvili, 2010). From the point of view of energy, earthquake phenomena cover quite a wide dynamic range. Within this range, different factors should affect phenomena that belong to different energetic classes. In order to investigate the influence of external factors, the gap method was applied to the catalogue of Caucasus earthquakes. The results pointed to a set of regularities for strong earthquakes - the earthquakes with $M>6$ that occurred during last 100 years (Lursmanashvili, 2001; 1973). Thirty strong earthquakes became sensitive indicators of tectonic activity of the Caucasus. Investigations lead to the following conclusions that make it possible to apply the gap approach to analysis of seismic processes in the Caucasus: the Caucasus reveals strong regularities in recurrence of $M>6$ earthquakes; the spectrum of recurrence of earthquakes contains 19 components, which have clear astronomical and geophysical sense (Lursmanashvili, 2001; Lursmanashvili et al., 2010); spectral distribution of time series of such earthquakes clearly indicated the fact that the release mechanism of tectonically prepared strong earthquakes depends on tidal phenomena - on positional relationship of Sun, Earth and the Moon and periodicities of their orbital movement. Table 1 presents the information on 9 components with a clear astronomical sense (Lursmanashvili, 2001).

The parameter "Gap width" represents the estimate of the period significance. The sense of this parameter is described above. Spectral components of the set of 30 earthquakes with high precision manifest values of astronomical periods represented by Table 1 and Table 2. The probability of accidental distribution of 30 time moments of earthquakes in such a way is practically zero.

Table 1.

Information on spectral components with a clear astronomical sense				
Period (days)	Gap width ($\Delta T/T\%$)	Astronomical sense	Frequency formula	Comments
27.30	34.2	Lunar sidereal month	s	Rotation frequency of: Moon –s, Perigee– p, Earth – h,
13.65	25.2	1/2 of Lunar sidereal month	$2s$	
27.54	27.9	Lunar anomalistic month	s-p	
29.51	30.0	Lunar synodical month	s-h	
347.93	31.6	Eclipse year	h+N	

173.56	25.7	1/2 of Eclipse year	*2(h+N)*	Ascending Node – *N*.
411.18	30.2	Sun crosses the perigee of Lunar orbit – full moon cycle	*h-p*	
3177.00	21.5	Lunar orbit perigee revolution period	*p*	
1588.80	29.8	1/2 of Lunar orbit perigee revolution period	*2p*	

Table 2.

Period (days)	Gap width ($\Delta T/T\%$)	Frequency calculation formula	Comments
39.58	24.9	*s-Me*	Rotation frequency of: Moon – *s*, Earth – *h*, Mercury – *Me*, Venus – *V*, Mars –*Ma*, Jupiter – *J*, Saturn - *St*, Uranus – *U*.
43.92	28.3	*2Me*	
44.41	27.1	*(s-h)-Me*	
175.14	30.1	*(Me-V)-(h-Ma)-(J-U)*	
181.60	25.7	*(Me-V)-(h-Ma)-(J-St)*	
184.73	25.8	*(Me-V)-(h-Ma)-J*	
606.86	32.3	*(V-h)-(St-U)*	
635.38	29.8	*(V-h)-(J-St)*	
662.83	23.2	*(V-h)-(J-U)*	
674.43	20.0	*(V-h)-J*	

As another evidence of tidal synchronization of earthquakes, we also present in Figs. 11 and 12 two distributions demonstrating distinct gaps corresponding to synchronization with long periods. The first is the distribution of angular distances of the Sun from Ascending Node on the celestial sphere for the time moments of strong earthquakes; the second is the distribution of angular distances of the Sun from perigee on the celestial sphere for the time moments of the same earthquakes. They demonstrate the causal relationship of the Caucasus strong earthquakes with tides. The gap method reveals the 346-day period, which corresponds to astronomical Dragon Year - the period between two transits of the Sun across the node of lunar orbit. Fig. 11 demonstrates the distribution inside this period. Fig. 12 demonstrates the distribution inside the revealed synchronization period corresponding to 411 days. With this period, the Sun crosses the perigee of the lunar orbit.

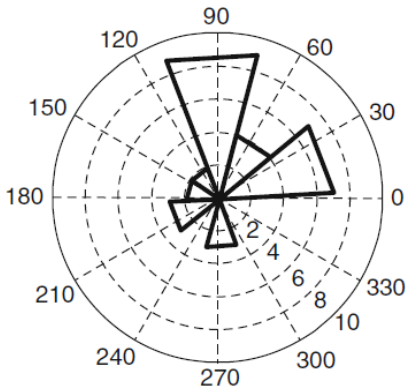

Fig. 11. The distribution of angular

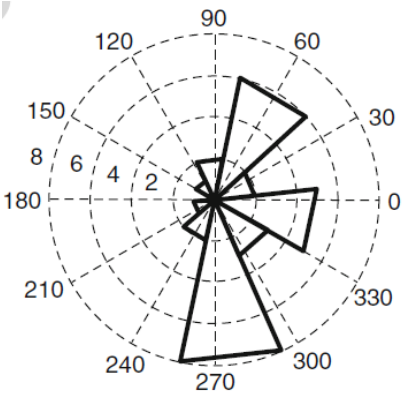

Fig. 12. The distribution of angular

distances of the Sun from Ascending Node on celestial sphere for strong earthquake time moments reveals 346 day period, corresponding to astronomical Dragon Year

distances of the Sun from perigee reveals synchronization period corresponding to 411 days. The Sun crosses the perigee of Lunar orbit with this period

It is important to note that the spectrum of investigated phenomena gives a possibility to reconstruct time series well suited for prediction, i.e. gives possibilities to solve the inverse problem. With the help of time characteristics of revealed external factors, the time intervals when influence of exogenous factors increases (in other words the intervals of increased probability of release of prepared earthquakes) can be explicitly determined. During the last century, there were many (about 100) time intervals with high probability of strong earthquakes, and only 30 strong events occurred in these intervals. We guess that in the remaining cases, epicenters were not prepared tectonically.

In Table 1 and 2 we have used Brown's tables, choosing the following parameters as fundamental arguments: τ - is the lunar time ($\tau = H + 180°$, where H is the hour angle of the moon), s - is the average longitude of the moon, p - is the longitude of the moon's perigee, t - is solar time, h - is the mean longitude of the Sun, $N' = -N$ is the longitude of the lunar node with the opposite sign, p_s is the longitude of the perihelion (Melkhior, 1976).

Any tidal wave may be described by the linear combination of mentioned six frequencies: $a\tau + bs + ch + dp + eN' + fp_s$, where $a = 1$ for tesseral diurnal waves and $-4 < b, c, d, e, f < 4$.

A very rational and convenient symbol designation for standardization and analysis of numerous tidal waves was introduced by Doodson: $a; b+5; c+5; d+5; e+5; f+5$. For instance, the tidal wave $\tau - 2s + 2h - p$ must be written by the procedure presented in Table 3 as combination 137455. The shift of 5 is chosen to represent the number in digits from 1 to 9.

Table 3.

Linear combination member	$a\tau$	bs	ch	dp	eN'	fp_s
Doodson number member	a	$b+5$	$c+5$	$d+5$	$e+5$	$f+5$
Numbers for wave $\tau - 2s + 2h - p$	1	-2+5	2+5	-1+5	0+5	0+5
Calculated Doodson number member	1	3	7	4	5	5
Doodson number	137455					

Astronomers more often use the Delaunay arguments (l, l', D, F, Ω) presented in Table 4.

Table 4.

Delaunay arguments	Period (day)	Meaning of argument
$l = s - p$	27.55	Mean anomaly of the Moon
$l' = h - p_s$	365	Mean anomaly of the Sun
$D = s - h$	29.5	Mean elongation of the Moon from the Sun
$F = s - N$	27.21	Mean elongation of the Moon from ascending node
$\Omega = -N$	6798	Mean longitude of the ascending node of the Moon

Modern measurements of the rotation of the Earth and the movement of its poles have reached such accuracy that for model creation it is necessary to take the influence of the planets of the solar

system into account. Each of the luni-solar terms in the nutation series is characterized by a set of five integers N_j, which determines the argument for the term as a linear combination of the five Fundamental Arguments F_j, namely the Delaunay variables (l, l', D, F, Ω) (Petit and Luzum 2010):

$$ARGUMENT = \Sigma_{j=1}^{5} N_j F_j .$$

Planetary nutation terms change the argument:

$$ARGUMENT = \Sigma_{j=1}^{14} N_j F_j .$$

Terms from F_6 to F_{13} be the mean longitudes of the planets including the Earth (L_{Me}, L_{Ve}, L_E, L_{Ma}, L_J, L_{Sa}, L_U, L_{Ne}) and F_{14} is the general precession in longitude P_A (Petit and Luzum, 2010). As we see, celestial mechanics describes the very small contribution in precession-nutation caused by planets (IAU 2006/2000A precession-nutation model). It is very important that our analysis reveals a set of combination frequencies pointing possible planetary influence. Table 2 represents these planetary frequencies.

The presence of so many long-periodical tidal components derived in Caucasus strong earthquakes time series confirm our hypothesis about tidal synchronization of Caucasus seismicity.

The frequency calculation formulas are derived by the use of algorithm similar to that used by Melkhior (1976) for decoding the spectrum of Luni-Solar tides. It seems that the fact of the sensitivity to this very small influence may be a reflection of complicated resonant phenomena in the Solar system (Grebennikov and Ryabov, 1978). The explanation and discussion of this result is beyond the objectives of this paper, but it possibly points out that the synchronization mechanism is tightly connected with the variations in the Earth's rotation axis.

As pointed out in section 2, an increase of parameter A determining the relative velocities of synchronization process, causes a decrease of the width of gap where the oscillator discharges are forbidden and causes a change of corresponding distribution form. The information on synchronizing factor persists in the corresponding histogram even in the case when the gap vanishes and may be used for the study of weak earthquakes synchronization. If one examines the values of possible external synchronizing periods with a sufficiently small step, it is possible to obtain the whole family of possible histograms. The study of their forms provides a possibility to discriminate histograms that are different from accidental and close to harmonicor pulse form. The difference from the accidental distribution may be determined by χ^2 criterion. The harmonic or pulse form may be modeled and fitted to the histogram by selection of its parameters and calculation of covariance as the measure of model and histogram similarity. The obtained phase and covariance values determine the amplitude and therefore all model parameters of the histogram representing the distribution inside the period of required external forcing.

This approach was tested by the use of Caucasus earthquakes data. We select the time interval from 1962 to 1987. During this period, the observational network of seismographs operated in Georgia was unified and equipped with homogeneous instrumental system. The objective was to study a possible tidal influence on weak earthquakes in the Caucasus region.

We selected two sets of events: 102 earthquakes with $M>4.7$ and 62 earthquakes with $M>5.0$. These sets are optimal for the study. There is sufficient amount of data and the energy growth velocity optimal for tidal influence study in the range of periods from 25 to 30 days. Four Lunar months –

synodical, sidereal, anomalistic and draconic, with the corresponding periods of 29.53, 27.32, 27.55 and 27.21 days, represent the tide components in the selected period range.

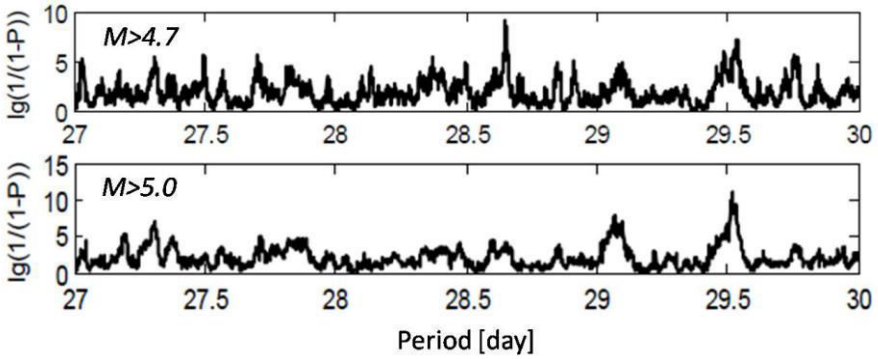

Fig. 13. Modified estimation of the non-randomness obtained by χ^2 criterion for Caucasian earthquakes of magnitude *M>4.7* and *M>5.0*. The increase of *M* separates the periods related to the tides and reveals the synchronization better.

The results are presented in Fig. 13 for *M>4.7* and *M>5.0*. The figure represents modified estimation of the non-randomness obtained by χ^2 criterion. For nonrandom periods, the usual estimation P gives values close to 1, and their perception is not convenient. We use the value $1/(1-P)$ - modification which represents the result more distinctly. It points to the number of random distributions, in which the given distribution may appear accidentally only once.

The logarithmic scale of $1/(1-P)$ represents the result better. For example, for the 29.53 day period, we have the value of estimation parameter equal to 6. It means that in million accidental distributions, a distribution corresponding to the synodical tide period is obtained only once. This statistical approach provides the compliance of synchronization model with the statistical requirements of data processing for the case of gap absence.

Some gaps and the corresponding periods in diagrams of Fig. 13 are not related to the tides. The increase of *M* and the estimation of the non-randomness obtained by χ^2 criterion separate the periods related to the tides. It is clear that the quakes of *M>5.0* better reveal the tidal synchronization.

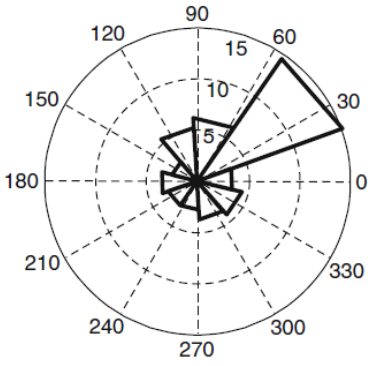

Fig. 14. The distribution of angular distances between the Moon and the Sun very distinctly reveals the earthquakes synchronization tidal period corresponding to 29.53 days

The period of 29.53 corresponds to the period of lunar phase recurrence, or to the period of highest tide recurrence, which is the sum of Lunar and Solar tidal waves. One can determine the phase of tide with maximal frequency of earthquakes. The distribution of angular distances between the

Moon and the Sun, corresponding to earthquakes moments and expressed in celestial coordinates, is presented in Fig. 14. The figure demonstrates 2-5 day shift from the new moon moment.

To extend the time and spatial intervals of the study, we performed similar analysis for 62 strong $M \geq 6$ earthquakes of Caucasus from 1640 to 2013. Earthquakes were selected from different catalogs. Phenomena of old, noninstrumental epoch were selected if they were present in at least two independent catalogs. Their spatial and time distribution is presented on Fig. 15. It should be noted that seismic process in Caucasus looks like natural rock disruption experiment, in which the Eurasian tectonic plate and the Arabian tectonic plate continuously compress the geological system of Caucasus. The result of this disruption is a network of seismically active faults.

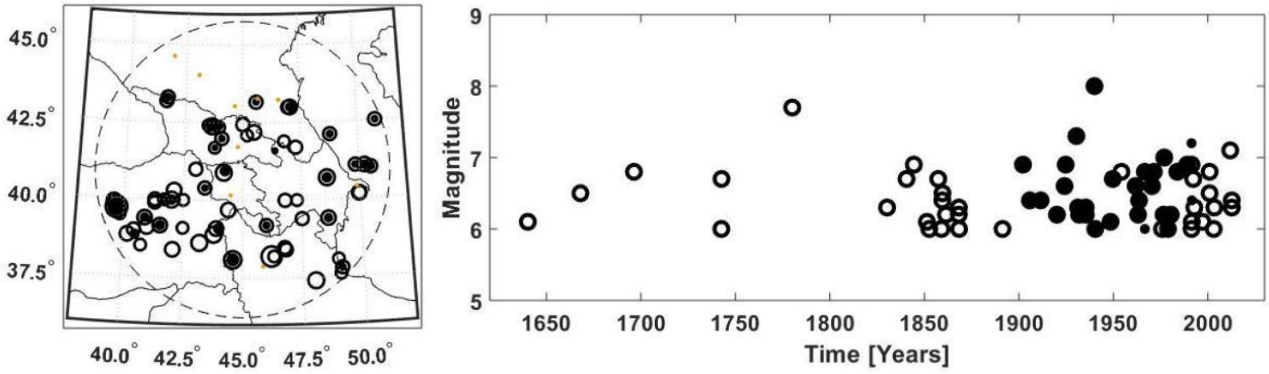

Fig. 15. Spatial and time distribution of $M \geq 6$ Caucasus earthquakes from 1640 to 2013 year. The location fits into a circle with a radius of 530 km. Black circles on diagrams correspond to the set of XX century 30 quakes.

The final result of the study of tidal synchronization of earthquakes triggering time moments of strong earthquakes of Caucasus region is presented in Fig. 16. This analysis confirmed earlier finding periodicities and reveal even more tidal components.

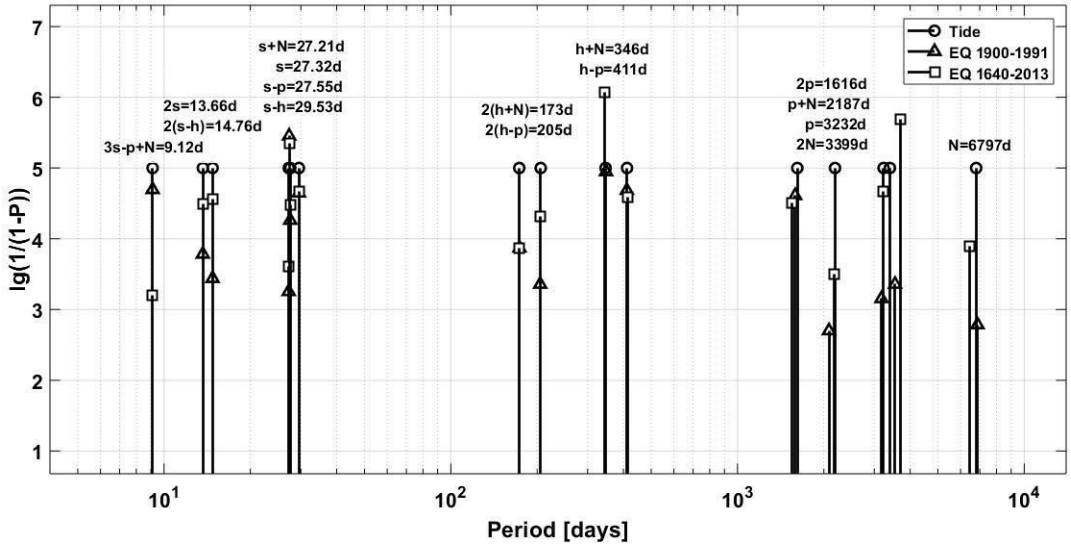

Fig. 16. The final result of tidal synchronization study for 62 strong $M \geq 6$ earthquakes occurred in Caucasus region from 1640 to 2013 year.

5. Discussion on luni-solar tidal synchronization of strong Caucasus earthquakes

The discovery of synchronization of Caucasus earthquakes caused by tides testifies the tidal triggering and the effectiveness of the used method. In discussion of tidal triggering, we should point to all difficulties and remember that tidal impact in geographical point *X* with latitude φ is determined by complicated gravitational potential *W(X)*.

Gravitational potential *W(X)* represents the set of spherical harmonics corresponding to different types of tidal impact:

$$W(X)=\frac{3}{4}G\mu\frac{r^2}{c^2}((\cos^2\varphi\cos^2\delta\cos 2H+\sin 2\varphi\sin 2\delta\cos H+3(\sin^2\varphi-\frac{1}{3})(\sin^2\delta-\frac{1}{3})). \quad (10)$$

G is the gravitational constant, μ is the mass of tide-making body (the Moon or the Sun), *r* is the distance from *X* to the center of the Earth, *c* is the distance between the Earth and the tidal body centers, and δ and *H* are the declination and hour angle. The first term describes the semidiurnal sectorial tidal wave, the second term describes the diurnal tesserial, and the third term describes the long period zonal wave.

The Lunar tide is approximately twice stronger than the solar tide. In any geographical point, we have a complicated picture as the sum of two components with different values of δ and *H*. The tidal force projections on vertical and two horizontal directions may be calculated as:

$$F_V=\frac{3}{2}G\mu M\frac{r}{c^3}\left(\cos^2\varphi\cos^2\delta\cos 2H+\sin 2\varphi\sin 2\delta\cos H+3(\sin^2\varphi-\frac{1}{3})(\sin^2\delta-\frac{1}{3})\right)$$

$$F_{NS}=-\frac{3}{4}G\mu M\frac{r}{c^3}\left(\sin 2\varphi\cos^2\delta\cos 2H-2\sin 2\delta\cos 2\varphi\cos H-3\sin 2\varphi(\sin^2\delta-\frac{1}{3})\right). \quad (11)$$

$$F_{EW}=\frac{3}{2}G\mu M\frac{r}{c^3}\left(\cos^2\delta\cos\varphi\sin 2H+\sin 2\delta\sin\varphi\sin H\right)$$

M is the mass of the Earth.

Long-period tidal waves modulate the short-period ones. The interaction of waves also complicates the tidal impact picture. There is one important consideration (Kartvelishvili K. and Kartvelishvili N., 1996) concerning the time of maximal tidal impact on the seismic focus - the tidal impact depends on the mutual directions of tidal force and stress vector in the epicenter of the earthquake under preparation, and the time of tide maximum may differ from the time of maximal impact. Some epicenters may be less sensitive or even insensitive to tidal impact. The fact that we reveal tidal synchronization also points out that we have a regular tendency in distribution of earthquakes mechanisms.

If we consider only tidal forces, formula (5) may be written as:

$$b_i(t-t_0)=P_{mi}-P_{0i}-F_L(t)\cos\gamma_{iL}-F_S(t)\cos\gamma_{iS},\ i=1,2,...,N, \quad (12)$$

where *N* is the number of developing sources, b_i the stress linear increase velocity in i-th epicenter, $P_{mi}-P_{0i}=C_i$ the stress necessary for this epicenter discharge and accumulated from the time moment t_0. $F_L(t)$ and $F_S(t)$ are the modules of Lunar and Solar tidal forces, and γ_{iL} and γ_{iS} determine mutual disposition of tidal and stress vectors.

As we have mentioned above, the epicenters with low stress accumulation velocity, low values of b_i coefficients in the system of equations (12), better "respond" to the external forcing.

The time moments of earthquakes and the corresponding values calculated for tidal components are known. The tidal impact on seismic region will be revealed at maximal values of tidal forces and their sum, and as better as close to each other are the directions of stresses responsible for earthquakes.

The triggering effect of earth tides is different in case of zonal, tesseral and sectorial tides and also significantly depends on latitude. The results of calculations carried out by using theoretical models show that only the horizontal shear stress produced by earth tides are able to influence the outbreak of earthquake (Varga and Grafarend, 2018).

6. Conclusions

This specific, luni-solar tide synchronization example is offered as a model approach to problems in the study of the correlation of some geophysical, biological and social phenomena with astronomical cycles. It is shown that external periodical factor can synchronize the relaxation oscillators discharge moments.

Astronomical synchronizing periodicities, as global periodical factors, may be determined by the analysis of distributions for all virtual forcing periods and detection of typical characteristic forms. Analyses will reveal the "gaps" - time intervals when discharges are absent, and also will demonstrate that the width of the gap depends on the stress (load) growth velocity. The strong, slowly growing synchronized oscillators demonstrate wider gaps; fast growth gives narrow gaps or modulation of distribution.

The validity of approach was tested and confirmed by model laboratory experiments, which demonstrate the existence of specific family of self-organized criticality phenomena with more predictable behavior.

The method was successfully applied to Caucasus earthquakes with $M>6$ and reveal a set of components with a clear astronomical meaning: the positional relationship of the Sun, the Earth and the Moon and periodicities of their orbital movement.

The analysis of earthquakes time series by presented approach and determination of external synchronization impact gives the possibility to estimate the background for long-term prediction of time intervals, in which the probability of earthquake occurrence in the Caucasus region is relatively high. Similar investigations for other seismic regions will be very useful to create a general picture of earth seismicity as synchronized response on tidal and other astronomical cycles.

References

1. Allen M., The lunar triggering of earthquakes in southern California. Bull. Seism. Soc. Am., Vol. 26, 1936, pp. 147-157.
2. Bak P., Tang C., Wiesenfeld K., Self-organized criticality, Phys. Rev. A, Vol. 38, July 1988, pp. 364-374.
3. Bak P., How Nature Works, Springer, New York, 1996, 226 p.
4. Beeler N., Lockner D., Why earthquakes correlate weakly with the solid Earth tides: Effects of periodic stress on the rate and probability of earthquake occurrence, J. Geophys. Res., B108, 2003, pp. 2391–2405.
5. Blechman I., Synchronization of Dynamical Systems, Moscow, 1971, 896 p.
6. Bretz M., Cunningham J., Kurczynsky P., Nori E., Imaging of avalanches in granular materials, Physical Review Letters, Vol. 69 , 1992, pp. 2431-2434.
7. Chelidze T., Lursmanashvili O., Electromagnetic and mechanical control of slip: laboratory experiments with slider system, Nonlin. Proc. Geophys., 20, 2003, pp. 1–8.
8. Chelidze T., Matsharashvili T., Gogiashvili J., Lursmanashvili O., Devidze M., Phase synchronization of slip in laboratory slider system, Nonlin. Proc. Geophys., 12, 2005, pp. 163-170.
9. Chelidze T., Matsharashvili T., Gogiashvili J., Lursmanashvili O., Devidze M., Electromagnetic Synchronization of Slip, Nonlinear Dynamics, Vol. 44, 2006, pp. 293-298.
10. Chizhevsky A., Physical Factors of the Historical Process, Kaluga, 1924, 72 p.
11. Custodio S., Fonseca J., Faria B., d'Oreye N., Tidal modulation of volcanic tremor in Fogo Island, Cape Verde, European Seismological Commission XXVIII Assembly Abstracts, Genoa, 2002, p. 236.
12. Dieterich J., Nucleation and triggering of earthquake slip: Effect of periodic stresses, Tectonophysics, 144, 1987, pp. 127–139.
13. Feder J., The evidence for Self-Organized Criticality in sand pile dynamics, Fractals, Vol. 3, No.3, 1995, pp. 431-443.
14. Heaton T., Tidal triggering of earthquakes. Geoph. J. I., Vol. 43, 1975, pp. 307-326.
15. Hoffman R., Aftershock energy release versus tidal effects, Hebgen Lake earthquakes, Montana. US. Geol. Survey Prof. Paper, 424-C, 1961, pp. 267-270.
16. Gheonjian L., Paatashvili T., Kapanadze G, Bebiava L., Kereselidze R., Rikadze A., Samkharadze D., Tsotskolauri P., Buzaladze I., Dighmelishvili T., Dolidze G., Evajian S., Gachechiladze S., Giorgobiani L., Kuprashvili I., Lomidze G., Oragvelidze M., Rakviashvili Sh., Tkhinvaleli A., Ubiria I., Tbilisi State University Extremely Low Frequency Radiation Research Net (ELFTSU Net): the First Measurements at Station Locations, XXIIth IEEE International Seminar/Workshop on Direct and Inverse Problems of Electromagnetic and Acoustic Wave Theory (DIPED), September 25-28, 2017, Dnipro, Ukraine, 2017a, pp. 169-173.
17. Gheonjian L., Paatashvili T., Kapanadze G.,ELF radio emission associated with strong M6.0 earthquake, XXIIth IEEE International Seminar/Workshop on Direct and Inverse Problems of Electromagnetic and Acoustic Wave Theory (DIPED), September 25-28, 2017, Dnipro, Ukraine, 2017b, pp. 29-30.
18. Gheonjian L., Paatashvili T., Oragvelidze M., Tsotskolauri P., Tbilisi State University Extremely Low Frequency Radiation Research Net (ELFTSU Net): the Concept and Structure of ELF Observation Station. XXIIIth IEEE International Seminar/Workshop on Direct and Inverse Problems

of Electromagnetic and Acoustic Wave Theory (DIPED), September 24-27, 2018, Tbilisi, Georgia, 2018a, pp. 213-216.
19. Gheonjian L., Paatashvili T., Oragvelidze M., Tsotskolauri P.,Tbilisi State University Extremely Low Frequency Radiation Research Net (ELFTSU Net): Earthquake Triggering and Synchronization Concept for the Net Operation. XXIIIth IEEE International Seminar/Workshop on Direct and Inverse Problems of Electromagnetic and Acoustic Wave Theory (DIPED), September 24-27, 2018, Tbilisi, Georgia, 2018b, pp. 217-221.
20. Grebennikov E., Ryabov Y., Resonances and small denominators in celestial mechanics. Nauka, 1978, 126 p.
21. IAU 2006/2000A precession-nutation model.ftp://tai.bipm.org/iers/conv2010/chapter5/tab5.2b.txt
22. Jaeger H., Nagel S., Physics of the granular state, Science, Vol. 255, 1992, pp.1523-1531.
23. Kartvelishvili K., Kartvelishvili N., Tidal triggering of earthquakes. Journal of Georgian Geophysical Society, Issue (A), Solid Earth, Vol. 2. 1996, pp. 81-86.
24. Khomeriki O., Paatashvili T., Gheonjian L., Kapanadze N., Invia N., The Influence of 7-day Variations of Interplanetary Magnetic Field on the Frequency of Myocardial Infarctions. Bull. Georgian Academy of Sciences, Vol. 158, No1, 1998, pp. 123-126.
25. Knopoff L., Earth tides as triggering mechanism for earthquakes. Bull. Seism. Soc. Am., Vol. 54, 1964, pp. 1865-1870.
26. Knopoff L., Earthquake prediction: The scientific Challenge. Proc. Nat. Acad. Sci. USA, Vol. 93, 1996, pp. 3719-3720.
27. Lursmanashvili O., Paatashvili T., Gheonjian L., Detecting quasi-harmonic factors synchronizing relaxation processes: application to seismology, in Synchronization and triggering. From fracture to Earthquake Processes, Springer, 2010, pp. 305-322.
28. Lursmanashvili O., On the periodicity of Caucasus strong earthquakes, Izvestiya Akademii Nauk SSSR, Fizika Zemli, No 2, 1973, pp. 80-86.
29. Lursmanashvili O., Role of exogenous factors in initiation of Caucasus earthquakes. Journal of the Georgian Geophysical Society, Issue (A), Physics of Solid Earth, Vol. 6. 2001, pp. 22-27.
30. Meerovich L., Zelichenko L. Impulse technique. Moscow, 1954, 600 p.
31. Matcharashvili T., Chelidze T., Javakhishvil Z., Nonlinear analysis of magnitude and interevent time interval sequences for earthquakes of the Caucasian region, Nonlin. Proc. Geophys., Vol. 7, 2000, pp. 9-19.
32. Melkhior P.The Physics and Dynamics of Planets. Mir, Moscow, 1976, 483 p.
33. Metivier, L., de Viron, O., Conrad, C., Renault, S., Diament, M., Patau G. Evidence of earthquake triggering by the solid earth tides, Earth and Planetary Science Letters, 278, 2009, pp. 370-375.
34. Nikolaev A. (Ed.), Induced Seismicity, Moscow, "Nauka", 1994, 220 p.
35. Otsuka K., Cornelissen G., Halberg F. Chronomics and Continuous Blood Pressure Monitoring. Vascular Chronomics: From 7-Day/24-Hour to Lifelong Monitoring. Springer, 2016, 934 p.
36. Perfettini H., Schmittbuhl J., Periodic loading on a creeping fault: Implications for tides,Geophys. Res. Lett., Vol. 28, 2001, pp. 435–438.
37. Petit G., Luzum B., (eds.), 2010, IERS Conventions (2010), IERS Technical Note 36, BKG, Frankfurt am Main, available at http://www.iers.org/TN36

38. Pikovsky A., Rosenblum M., Kurth J., Synchronization: Universal Concept in Nonlinear Science, Cambridge University Press, Cambridge, 2003, 411 p.
39. Palumbo A., Lunar and solar tidal components in the occurrence of earthquakes in Italy.Geophys. J. I., Vol. 84, No 1, 1986, pp. 93-99.
40. Ryall A., Van Wormer J., Jones A., Triggering of microearthquakes by earth tides, and other features of the Truckee, California earthquake sequences of September 1966. Bull. Seism. Soc. Am. 58,1968, pp. 215-248.
41. Scholz C., Good tidings, Nature, 425 (6959), 2003, pp. 670–671.
42. Shlien S., Earthquake-tide correlation. Geoph. J. I., Vol. 28, No 1, 1972, pp. 27-34.
43. Simpson J., Earth tides as a triggering mechanism for earthquakes. Earth. Planet. Sci. Lett., Vol. 2, 1967, pp. 473-478.
44. Sobolev G., Ponomarev A., Physics of Earthquakes and Precursors, Nauka, 2003, 270 p.
45. Tanaka S., Sato H., Matsumura S., Ohtake M., Tidal triggering of earthquakes in the subducting Philippine sea plate beneath the locked zone of the plate interface in the Tokai region, Tectonophysics, 417, 2006, pp. 69-80.
46. Tanaka S., Tidal triggering of earthquakes precursory to the recent Sumatra megathrust earthquakes of 26 December 2004 (Mw 9.0), 28 March 2005 (Mw 8.6), and 12 September 2007 (Mw 8.5), Geophys. Res. Lett., 37, 2010, L02301, DOI:10.1029/2009GL041581.
47. Tamrazian G., Principal regularities in the distribution of major earthquakes relative to solar and lunar tides and other cosmic sources. Icarus 9, 1968, pp. 574-592.
48. Tormann T., Enescu B., Woessner J., Wiemer S., Randomness of megathrust earthquakes implied by rapid stress recovery after the Japan earthquake. Nature Geoscience, 8, 2, 2015, 152-158.
49. Varga P., Grafarend E., Influence of Tidal Forces on the Triggering of Seismic Events. Pure Appl. Geophys. 2018, 175: 1649. https://doi.org/10.1007/s00024-017-1563-5.
50. Vidale J., Agnew D., Johnston M., Oppenheimer D., Absence of earthquake correlation with earth tides: an indication of high preseismic fault stress rate, J. Geophys. Res., 103, 1998, pp. 24.567–24.572.
51. Wang Y., Mora P., Yin C., Place D. Statistical tests of load/unload response ratio signals by lattice solid model, Pure Appl. Geophys., 161, 2004, pp. 1829–1839.
52. Weems R., Perry W., Strong correlation of major earthquakes with solid-earth tides in part of the eastern United States. Geology, Vol. 17, 1989, pp. 661-664.

Astronomy & Astrophysics (Caucasus) 4, (2018)

Multiparameter atlas of the Moon

O.Kvaratskhelia[2], R.Chigladze[1,2]

[1]Samtskhe-Javakheti State University,

[2]E.Kharadze Abastumani Astrophysical Observatory, Ilia State University

E-mail :kvara otar.@mail.ru

E-mail:revazchigladze@yahoo.com

Abstract

The Moon, because of the absence of the atmosphere, preserves the signs of the initial stage of the Solar System evolution. This is the major cause of the planetary scientists' interest in the Moon. Optical measurements of the Moon surface in remote geology are the main source of information and they were relevant even in the epoch of interstellar flights. Observations of the Moon from the Earth are more affordable and regular and are less expensive as compared to the observations made from spacecrafts. As the practice evidences, the investigations made from the Earth and from the spacecrafts specify and supplement each other. Now, as there is a pause in the Moon explorations by means of spacecrafts, hte optical observations from the Earth, as the only means to study the Moon surface, are even more topical.

Key words:Moon,Albedo,Polarization,Color Index

1. Introduction

The first steps in the study of the Moon were the Moon explorations by means of manned spacecrafts started in the 1970s. The next step in studying the Moon must be manned expeditions, which will create first temporary bases on the Moon followed by the permanent bases. The problem of the Moon management by a human is associated with two objectives: first, living conditions must be created for the astronauts working at bases and second, the staging ground must be developed for the space flights of the second stage. The astronomers can participate in implementing the first objective. In particular, they can identify the location suitable to create the base on the Moon making it possible to create living conditions for the astronauts – the location rich in oxygen, hydrogen and Helium-3 isotope, as in the possible source of energy. In order to realize this objective, average sizes the regolith particles of the Moon must be studied. The identification of the Moon's regions by identifying the possible distribution of the fine fractions in them is necessary and topical, because as the analysis of the ground brought from the Moon has shown, the fine structures with the sizes of their particles of less than 45μm, contain 80% of the hydrogen and Helium-3. It is surprising, but it is a fact that the Moon surface deprived of the atmosphere can be a source of oxygen. The compounds of the three principal Moon minerals contain up to 40% of oxygen. The most suitable material to produce oxygen is ilmenite ($FeTiO_2$). The content of titanium dioxide (TiO_2) in the Moon ground is up to 20%. Our goal is to identify such regions.

In the final run, the locations most suitable to build the Moon base are those with a fine ground containing a large amount of titanium dioxide. The primary goal is to study the looseness and maturity of the ground, while another objective is associated with the chemical and mineralogical zoning of the Moon surface.

Of the polarimetric parameters, the correlations between the main phase-polarization P(α) and spectrum-polarization P(λ) parameters and their associations with other parameters of the light reflected from the Moon surface are studied.

Our goal is to identify the typical regions by considering the mentioned parameters and regions similar to the landing regions of "Apollo" and "Luna" series spacecrafts and evaluate their distribution on the Moon surface. The publication of the multiparameter atlas of the Moon is dedicated to these issues.

The Atlas had been developed for decades based on the material observed on the Moon at: Abastumani Astrophysical Observatory [1,4,8,11], Institute of Astronomy of Kharkiv (Ukraine) [2,3,7,10] and Meudon Observatory (France) [6].

The table is given: Crater name, Latitude, Longitude, Diameter, polarization(min,max), Color Index, Albedo (λ=6200Å) and m is an Albedo (λ=5500Å).

1. ANALYSIS AND CONCLUSIONS:

In accordance with P_{min}

Crater	Latitude	Longitude	Diameter km	Polarization		Color Index [2,7]	Albedo [3,7]	m [5,7]
				min	max			
Tycho	43.31° S	11.36° W	86	0.60	9.00	1.22	15.20	18.60
Proclus	16.1° N	46.8° E	28	0.62	5.20	1.22	12.40	15.70
Aristarchus	23.7° N	47.4° W	40	0.66		1.19	12.40	13.50
Copernicus	9.62° N	20.08° W	93	0.74	4.00	1.26	18.50	16.60
Anaxagoras	73.48° N	10.17° W	51.9	0.74		1.29	20.20	17.30
Crater North from Tycho	41.5°S	10°W	12	0.75		1.22	18.50	9.70
Creter Weast from Cyrillus	11.5° S	21.8° E	28	0.80		1.20	18.50	18.60
Petavius	25.3° S	60.4° E	177	0.80		1.29	12.40	16.90
Crater, North-West from Petavius	20°S	57.5°E	5	0.80		1.29	9.70	17.30

Theophilus	11.4° S	26.4° E	100	0.82	4.70	1.11	17.20	17.30
Cyrillus	13.2° S	24° E	98	0.85	3.80	1.11	18.50	19.80
Kepler	8.1° N	38° W	32	0.85	3.90	1.22	17.20	11.70
Dionysius	2.8° N	17.3° E	18	0.86		1.19	12.40	12.50
Crater South from Tycho	46°S	11.5°W	12	0.86		1.24	20.20	16.90
Hercules	46.7° N	39.1° E	69	0.88		1.24	13.30	13.50
Dzhapiashvili	7.5° N	56.5° E	48	1.20	18.0	1.32	13.30	14.1
Creter1 Weast from Alfraganus	1.7° S	19.3° E	28	0.92		1.15	12.40	13.50
Creter2 Weast from Alfraganus	6° S	18.3° E	28	0.92		1.19	17.20	18.60
Region North-West of Furnerius	33.3°S	57°E	28	0.93		1.26	17.20	17.30
Endymion	53.6° N	56.5° E	125	0.93		1.19	12.40	14.10
Crater North from Tycho	39.5°S	7°W	12	0.94		1.20	20.20	17.30
Mare Nubium	21.3° S	16.6° W	715	0.94		1.24	8.40	8.90
Crater North from Hind	7.3°S	8.3°E	5	0.96		1.20	15.20	14.10
Godin	1.8° N	10.2° E	35	0.97		1.19	15.20	15.70
Scoresby	77.7° N	14.1° E	56	0.97		1.22	20.20	16.90
Pickering	2.88° S	6.99° E	15	1.00		1.17	15.20	15.70
Eratosthenes	14.47°N	11.32° W	59	1.00		1.20	11.60	11.40
Messier	1.9°S	47.6°E	9 × 11	1.00		1.22	8.80	9.70
Alpetragius	16° S	4.5° W	40	1.00		1.24	12.40	12.50
Creter Weast from Theophilus	10.5° S	23.5° E	28	1.01		1.22	17.20	15.70
Menelaus	16.3°N	16° E	27	1.01		1.19	14.20	13.50
Vaisala	25.9° N	47.8° W	8	1.01		1.20	11.60	12.50
Catharina	18° S	23.6° E	100	1.01	4.20	1.22	17.20	17.30
Clavius	58.4° S	14.4° W	231	1.01		1.24	18.50	19.80

Reiner	7° N	54.9° W	30	1.03		1.18	9.00	8.20
Crater South from Deslandres	37°S	4°W	12	1.03		1.20	23.20	18.60
Rosse	17.8°S	35°E	12	1.05		1.26	10.90	11.70
Plinius	15.4° N	23.7° E	43	1.05		1.06	12.40	11.40
Apollo 12 landing area	3.01° S	23.42° W	28	1.05		1.19	9.70	10.90
Herodotus	23.2° N	49.7° W	35	1.05		1.22	15.20	11.40
Macrobius	21.3° N	46.0° E	64	1.05		1.22	15.20	13.50
Region between Proclus and Macrobius	18.2°N	46.4°E	28	1.05		1.26	17.20	17.30
Triesnecker	4.18° N	3.6° E	26	1.06		1.17	17.20	14.10
Flamsteed	4.5° S	44.3° W	21	1.07		1.09	9.70	8.20
Mare Undarum	6.8° N	68.4° E	243	1.07		1.24	8.80	9.70
Mare Imbrium	32.8° N	15.6° W	1145	1.07		1.2	7.80	10.20
Mare Crisium	17° N	59.1° E	555	1.07	8.80	1.19	8.60	9.70
Fra Mauro	6° S	17° W	95	1.07		1.22	13.30	12.50
Langrenus	8.9° S	60.9° E	132	1.07		1.32	8.60	16.60
Crater South from Crozier	14°S	51.5°E	12	1.08		1.32	13.30	15.10
Messala	39.2° N	59.9° E	125	1.08		1.19	14.20	15.10
Crater North-West from Tycho	38.3°S	16°W	12	1.08		1.24	18.50	15.70
Crater North-West from Tycho	36°S	15°W	12	1.08		1.24	20.20	16.90
Mare Frigoris North-East region	56° N	28° E	28	1.09		1.29	10.90	10.90
Posidonius	31.8° N	29.9° E	95	1.09	5.20	1.22	12.40	13.50
Apollo 14 landing area	3.64° S	17.47° W	28	1.10		1.19	11.60	12.50
Manilius	14.5° N	9.1° E	39	1.10		1.21	15.20	13.50

Arzachel	18.2° S	1.9° W	96	1.10		1.24	14.20	15.70
Eudoxus	44.3° N	16.3° E	67	1.10	8.0	1.26	15.20	15.10
Hooke	18.3°N	53.5°E	18	1.11		1.20	9.00	9.70
Mare Humorum	24.4° S	38.6° W	389	1.11		1.18	8.00	8.20
Oceanus Procellarum	18.4° N	57.4° W	2592	1.11		1.18	7.60	7.00
Bessel	21.8° N	17.9° E	16	1.11		1.18	9.30	9.70
Aristillus	33.7°N	1°E	55	1.11	8.90	1.19	11.60	11.70
Apollo 15 landing area	26.13° N	3.63° E	12	1.11		1.20	16.20	8.90
Alphonsus	13.4° S	2.8° W	119	1.11	6.60	1.24	14.20	14.10
Mare Serenitatis (S-W from Bessel)	19° N	17° E	28	1.12		1.19	8.40	8.90
Lansberg	0.3° S	26.6° W	39	1.12		1.19	9.30	10.90
T. Mayer	15.6° N	29.1° W	33	1.12		1.20	14.20	11.40
Mare Fecunditatis	7.8°S	51.3°E	840	1.12		1.22	8.60	9.70
Mare Fecunditatis (S W region)	8°S	49°E	28	1.12		1.24	9.70	9.70
Crater East from Clavius	59°S	5°W	28	1.12		1.26	17.20	17.30
Bullialdus	20.7° S	22.2° W	61	1.13		1.19	12.40	12.50
Picard	14.57°N	54.72°E	23	1.13		1.19	9.30	9.70
Apollo 17 landing area	20.19°N	30.77° E	28	1.14		1.18	11.60	11.40
Burg	45° N	28.2° E	40	1.14		1.29	14.20	11.40
Cleomedes	27.7° N	55.5° E	126	1.14		1.21	12.40	12.50
Region between Aristoteles and Eudoxus	46.7° N	17° E	28	1.15	12.50	1.29	15.20	12.50
Crater East from Horrocks	4.0°S	7.5°E	5	1.16		1.22	15.20	14.10
Geminus	31.5° N	56.7° E	86	1.16		1.17	15.20	15.20

Mare Imbrium (North from Autolycus)	32° N	1.3° E	28	1.16		1.20	12.40	12.50
Apollo 16 landing area	8.97° S	15.5° E	28	1.16		1.20	12.40	12.50
Purbach	25.5° S	1.9° W	118	1.16		1.22	13.30	13.50
Mare Crisium (North from Picard)	16.2° S	53.7° E	28	1.16		1.36	9.70	13.50
Meton	73.8° N	19.2° E	122	1.16		1.22	18.50	16.90
Harpalus	52.6° N	43.4° W	39	1.16		1.29	9.30	10.20
Aristoteles	50.2° N	17.4° E	87	1.16		1.32	15.20	15.70
Plato	51.6° N	9.3° W	109	1.16	9.00	1.38	12.40	10.20
Mare Tranquillitatis	8.5° N	31.4° E	873	1.17		1.09	7.40	8.90
Luna 24 landing area	12.71°N	62.21° E	28	1.17		1.20	8.80	11.40
Ptolemaeus	9.2° S	1.8° W	153	1.17	9.30	1.21	13.30	12.50
Janssen	44.96° S	40.82° E	190	1.17		1.26	13.30	16.60
Crater North-East from Horrocks	3.0°S	7.0°E	5	1.18		1.22	15.20	15.70
Pitatus	29.8° S	13.5° W	34.1	1.18		1.20	11.60	10.20
Crater South from Baily	48.4°N	31.3°E	12	1.19		1.32	9.60	11.70
Marius	11.9° N	50.8° W	41	1.19		1.20	9.00	7.50
Schickard	44.4° S	54.6° W	227	1.19		1.24	16.20	10.20
Crater North-East from Maginus	48.7°S	1.5°W	12	1.19		1.24	18.50	19.80
Fracastorius	21.2° S	33° E	124	1.19	5.00	1.26	10.30	13.50
Gutenberg	8.6° S	41.2° E	74	1.19		1.26	15.20	15.10
Apollo 11 landing area	0.67° N	23.47° E	28	1.20		1.13	8.60	8.90
Crater East from	10.3°S	11°W	28	1.20		1.15	8.40	9.70

Guericke								
Archimedes	29.7° N	4° W	83	1.20	9.10	1.20	10.30	10.20
Lambert	25.8° N	21° W	30	1.20		1.20	8.40	9.70
Timocharis	26.7° N	13.1° W	34.1	1.20		1.22	9.30	11.40
Autolycus	30.7° N	1.5° E	39	1.20	9.0	1.22	12.40	11.40
Crater North from Jacobi	53.5°S	11°E	12	1.21		1.36	16.20	16.90
Luna 20 landing area	3.53° N	56.55° E	28	1.21		1.19	7.80	8.90
Reinhold	3.3° N	22.8° W	48	1.21		1.19	13.30	10.90
Euler	23.3° N	29.2° W	28	1.21		1.24	12.40	10.20
Bianchini	48.7° N	34.3° W	38	1.21		1.32	15.20	11.70
Crater South from Ritchey	12.3°S	9.2°E	12	1.22		1.24	9.30	12.50
Mare Nectaris	15.2° S	34.6° E	340	1.22	7.60	1.24	9.70	11.40
Montes Pyrenaeus	15.6° S	41.2° E	167	1.22		1.32	12.40	16.90
Sinus Medii	2.4° N	1.7° E	335	1.23		1.18	10.90	11.70
Mare Fecunditatis (South region)	18°S	53°E	28	1.24		1.36	12.40	12.50
Letronne	10.6° S	42.4° W	120	1.24		1.17	8.40	8.20
Luna 16 landing area	0.68° S	56.3° E	28	1.25		1.18	7.60	8.90
Billy	13.8° N	50.1 W	45	1.25		1.20	9.30	7.50
Furnerius	36.3° S	60.4° E	125	1.25		1.29	17.20	17.30
Crater West from Timaeus	63°N	7.5°W	28	1.25		1.29	16.20	19.80
Seleucus	21° N	66.6° W	61	1.26		1.18	9.70	8.20
Region East of Endymion	56° N	63° E	28	1.27		1.17	14.20	14.20
Ross	11.7° N	21.7° E	24	1.28		1.09	15.20	7.50
Mare Frigoris	56° N	1.4° E	1446	1.30		1.18	13.30	13.50
Grimaldi	5.2° S	68.6° W	173.49	1.30		1.19	15.20	8.90

Bonpland	8.3° S	17.4° W	60	1.30		1.24	14.20	13.50
Maurolycus	41.8° S	14° E	114	1.30		1.24	17.20	17.30
Mairan	41.6° N	43.4° W	40	1.30		1.29	15.20	14.10
Eddington	21.5° N	71.8° W	125	1.31		1.19	9.30	8.20
Montes Apenninus	18.9° N	3.7° W	5.4	1.31		1.22	12.40	13.50
Mare Serenitatis	28° N	17.5° E	674	1.32		1.10	12.40	9.70
Hooke	41.2° N	54.9° E	139	1.32		1.22	15.20	15.70
Crater East from Piccolomini	30.7°S	36°E	28	1.33		1.36	15.20	16.90
Piccolomini	29.7° S	32.3° E	88	1.33		1.29	15.20	16.90
Region East of Mare Crisium	22° N	73° E	28	1.34		1.22	9.00	14.10
Region North of Petavius	21.3°S	62.5°E	28	1.36		1.29	9.30	14.10
Region East of Langrenus	9° S	66.5° E	28	1.37		1.32	12.40	14.10
Crater North from Plato	55°N	8.3°W	28	1.37		1.40	15.20	13.50
Crater North from Manilius	17.5°N	11.3°E	12	1.38		1.18	8.40	10.90
Lehmann	40° S	56° W	53	1.38		1.24	14.20	11.40
Crater North from Mare Serenitatis	39° S	17.2° E	28	1.39		1.26	14.20	16.60

In accordance with P_{max}

Crater	Latitude	Longitude	Diameter	Polarization		Color Index [2,7]	Albedo [3,7]	m [5,7]
				min	max			
Cyrillus	13.2° S	24° E	98	0.85	3.80	1.11	18.50	19.80
Kepler	8.1° N	38° W	32	0.85	3.90	1.22	17.20	11.70
Copernicus	9.62° N	20.08° W	93	0.74	4.00	1.26	18.50	16.60
Catharina	18° S	23.6° E	100	1.01	4.20	1.22	17.20	17.30
Theophilus	11.4° S	26.4° E	100	0.82	4.70	1.11	17.20	17.30
Fracastorius	21.2° S	33° E	124	1.19	5.00	1.26	10.30	13.50
Posidonius	31.8° N	29.9° E	95	1.09	5.20	1.22	12.40	13.50
Proclus	16.1° N	46.8° E	28	0.62	5.20	1.22	12.40	15.70
Alphonsus	13.4° S	2.8° W	119	1.11	6.60	1.24	14.20	14.10
Mare Nectaris	15.2° S	34.6° E	340	1.22	7.60	1.24	9.70	11.40
Eudoxus	44.3° N	16.3° E	67	1.10	8.00	1.26	15.20	15.10
Mare Crisium	17° N	59.1° E	555	1.07	8.80	1.19	8.60	9.70
Aristillus	33.7°N	1°E	55	1.11	8.90	1.19	11.60	11.70
Autolycus	30.7° N	1.5° E	39	1.20	9.00	1.22	12.40	11.40
Tycho	43.31° S	11.36° W	86	0.60	9.00	1.22	15.20	18.60
Plato	51.6° N	9.3° W	109	1.16	9.00	1.38	12.40	10.20
Archimedes	29.7° N	4° W	83	1.20	9.10	1.20	10.30	10.20
Ptolemaeus	9.2° S	1.8° W	153	1.17	9.30	1.21	13.30	12.50
Region between Aristoteles and Eudoxus	46.7° N	17° E	28	1.15	12.50	1.29	15.20	12.50
Dzhapiashvili	7.5° N	56.5° E	48	1.20	18.0	1.32	13.30	14.1

In accordance with COLOR INDEX

Crater	Latitude	Longitude	Diameter	Polarization		Color Index [2,7]	Albedo [3,7]	m [5,7]
				min	max			
Plinius	15.4° N	23.7° E	43	1.05		1.06	12.40	11.40
Flamsteed	4.5° S	44.3° W	21	1.07		1.09	9.70	8.20
Mare Tranquillitatis	8.5° N	31.4° E	873	1.17		1.09	7.40	8.90
Ross	11.7° N	21.7° E	24	1.28		1.09	15.20	7.50
Mare Serenitatis	28° N	17.5° E	674	1.32		1.10	12.40	9.70
Theophilus	11.4° S	26.4° E	100	0.82	4.70	1.11	17.20	17.30
Cyrillus	13.2° S	24° E	98	0.85	3.80	1.11	18.50	19.80
Apollo 11 landing area	0.67° N	23.47° E	28	1.20		1.13	8.60	8.90
Creter1 Weast from Alfraganus	1.7° S	19.3° E	28	0.92		1.15	12.40	13.50
Crater East from Guericke	10.3°S	11°W	28	1.20		1.15	8.40	9.70
Pickering	2.88° S	6.99° E	15	1.00		1.17	15.20	15.70
Triesnecker	4.18° N	3.6° E	26	1.06		1.17	17.20	14.10
Geminus	31.5° N	56.7° E	86	1.16		1.17	15.20	15.20
Letronne	10.6° S	42.4° W	120	1.24		1.17	8.40	8.20
Region East of Endymion	56° N	63° E	28	1.27		1.17	14.20	14.20
Reiner	7° N	54.9° W	30	1.03		1.18	9.00	8.20
Mare Humorum	24.4° S	38.6° W	389	1.11		1.18	8.00	8.20
Oceanus Procellarum	18.4° N	57.4° W	2592	1.11		1.18	7.60	7.00
Bessel	21.8° N	17.9° E	16	1.11		1.18	9.30	9.70
Apollo 17 landing area	20.19°N	30.77° E	28	1.14		1.18	11.60	11.40

Sinus Medii	2.4° N	1.7° E	335	1.23		1.18	10.90	11.70
Luna 16 landing area	0.68° S	56.3° E	28	1.25		1.18	7.60	8.90
Seleucus	21° N	66.6° W	61	1.26		1.18	9.70	8.20
Mare Frigoris	56° N	1.4° E	1446	1.30		1.18	13.30	13.50
Crater North from Manilius	17.5°N	11.3°E	12	1.38		1.18	8.40	10.90
Dionysius	2.8° N	17.3° E	18	0.86		1.19	12.40	12.50
Creter2 Weast from Alfraganus	6° S	18.3° E	28	0.92		1.19	17.20	18.60
Endymion	53.6° N	56.5° E	125	0.93		1.19	12.40	14.10
Godin	1.8° N	10.2° E	35	0.97		1.19	15.20	15.70
Menelaus	16.3°N	16° E	27	1.01		1.19	14.20	13.50
Apollo 12 landing area	3.01° S	23.42° W	28	1.05		1.19	9.70	10.90
Messala	39.2° N	59.9° E	125	1.08		1.19	14.20	15.10
Apollo 14 landing area	3.64° S	17.47° W	28	1.10		1.19	11.60	12.50
Grimaldi	5.2° S	68.6° W	173.49	1.30		1.19	15.20	8.90
Mare Serenitatis (S-W from Bessel)	19° N	17° E	28	1.12		1.19	8.40	8.90
Lansberg	0.3° S	26.6° W	39	1.12		1.19	9.30	10.90
Bullialdus	20.7° S	22.2° W	61	1.13		1.19	12.40	12.50
Picard	14.57°N	54.72°E	23	1.13		1.19	9.30	9.70
Aristillus	33.7°N	1°E	55	1.11	8.90	1.19	11.60	11.70
Aristarchus	23.7° N	47.4° W	40	0.66		1.19	12.40	13.50
Luna 20 landing area	3.53° N	56.55° E	28	1.21		1.19	7.80	8.90
Reinhold	3.3° N	22.8° W	48	1.21		1.19	13.30	10.90
Mare Crisium	17° N	59.1° E	555	1.07	8.80	1.19	8.60	9.70
Eddington	21.5° N	71.8° W	125	1.31		1.19	9.30	8.20
Creter Weast from Cyrillus	11.5° S	21.8° E	28	0.80		1.20	18.50	18.60

Crater North from Tycho	39.5°S	7°W	12	0.94		1.20	20.20	17.30
Crater North from Hind	7.3°S	8.3°E	5	0.96		1.20	15.20	14.10
Eratosthenes	14.47° N	11.32° W	59	1.00		1.20	11.60	11.40
Vaisala	25.9° N	47.8° W	8	1.01		1.20	11.60	12.50
Crater South from Deslandres	37°S	4°W	12	1.03		1.20	23.20	18.60
Mare Imbrium	32.8° N	15.6° W	1145	1.07		1.20	7.80	10.20
Hooke	18.3°N	53.5°E	18	1.11		1.20	9.00	9.70
Apollo 15 landing area	26.13° N	3.63° E	12	1.11		1.20	16.20	8.90
T. Mayer	15.6° N	29.1° W	33	1.12		1.20	14.20	11.40
Mare Imbrium (North from Autolycus)	32° N	1.3° E	28	1.16		1.20	12.40	12.50
Apollo 16 landing area	8.97° S	15.5° E	28	1.16		1.20	12.40	12.50
Luna 24 landing area	12.71°N	62.21° E	28	1.17		1.20	8.80	11.40
Pitatus	29.8° S	13.5° W	34.1	1.18		1.20	11.60	10.20
Marius	11.9° N	50.8° W	41	1.19		1.20	9.00	7.50
Lambert	25.8° N	21° W	30	1.20		1.20	8.40	9.70
Archimedes	29.7° N	4° W	83	1.20	9.10	1.20	10.30	10.20
Billy	13.8° N	50.1 W	45	1.25		1.20	9.30	7.50
Manilius	14.5° N	9.1° E	39	1.10		1.21	15.20	13.50
Cleomedes	27.7° N	55.5° E	126	1.14		1.21	12.40	12.50
Ptolemaeus	9.2° S	1.8° W	153	1.17	9.30	1.21	13.30	12.50
Proclus	16.1° N	46.8° E	28	0.62	5.20	1.22	12.40	15.70
Tycho	43.31° S	11.36° W	86	0.60	9.00	1.22	15.20	18.60
Catharina	18° S	23.6° E	100	1.01	4.20	1.22	17.20	17.30
Crater North	41.5°S	10°W	12	0.75		1.22	18.50	9.70

from Tycho								
Posidonius	31.8° N	29.9° E	95	1.09	5.20	1.22	12.40	13.50
Scoresby	77.7° N	14.1° E	56	0.97		1.22	20.20	16.90
Messier	1.9°S	47.6°E	9 × 11	1.00		1.22	8.80	9.70
Creter Weast from Theophilus	10.5° S	23.5° E	28	1.01		1.22	17.20	15.70
Macrobius	21.3° N	46.0° E	64	1.05		1.22	15.20	13.50
Fra Mauro	6° S	17° W	95	1.07		1.22	13.30	12.50
Kepler	8.1° N	38° W	32	0.85	3.90	1.22	17.20	11.70
Mare Fecunditatis	7.8°S	51.3°E	840	1.12		1.22	8.60	9.70
Herodotus	23.2° N	49.7° W	35	1.05		1.22	15.20	11.40
Crater East from Horrocks	4.0°S	7.5°E	5	1.16		1.22	15.20	14.10
Purbach	25.5° S	1.9° W	118	1.16		1.22	13.30	13.50
Meton	73.8° N	19.2° E	122	1.16		1.22	18.50	16.90
Crater North-East from Horrocks	3.0°S	7.0°E	5	1.18		1.22	15.20	15.70
Autolycus	30.7° N	1.5° E	39	1.20	9.0	1.22	12.40	11.40
Timocharis	26.7° N	13.1° W	34.1	1.20		1.22	9.30	11.40
Montes Apenninus	18.9° N	3.7° W	5.4	1.31		1.22	12.40	13.50
Hooke	41.2° N	54.9° E	139	1.32		1.22	15.20	15.70
Region East of Mare Crisium	22° N	73° E	28	1.34		1.22	9.00	14.10
Schickard	44.4° S	54.6° W	227	1.19		1.24	16.20	10.20
Crater South from Tycho	46°S	11.5°W	12	0.86		1.24	20.20	16.90
Hercules	46.7° N	39.1° E	69	0.88		1.24	13.30	13.50
Mare Nubium	21.3° S	16.6° W	715	0.94		1.24	8.40	8.90
Alpetragius	16° S	4.5° W	40	1.00		1.24	12.40	12.50
Clavius	58.4° S	14.4° W	231	1.01		1.24	18.50	19.80

Mare Undarum	6.8° N	68.4° E	243	1.07		1.24	8.80	9.70
Crater North-West from Tycho	38.3°S	16°W	12	1.08		1.24	18.50	15.70
Crater North-West from Tycho	36°S	15°W	12	1.08		1.24	20.20	16.90
Arzachel	18.2° S	1.9° W	96	1.10	13.20	1.24	14.20	15.70
Alphonsus	13.4° S	2.8° W	119	1.11	6.60	1.24	14.20	14.10
Mare Fecunditatis (S W region)	8°S	49°E	28	1.12		1.24	9.70	9.70
Crater North-East from Maginus	48.7°S	1.5°W	12	1.19		1.24	18.50	19.80
Euler	23.3° N	29.2° W	28	1.21		1.24	12.40	10.20
Crater South from Ritchey	12.3°S	9.2°E	12	1.22		1.24	9.30	12.50
Mare Nectaris	15.2° S	34.6° E	340	1.22	7.60	1.24	9.70	11.40
Bonpland	8.3° S	17.4° W	60	1.30		1.24	14.20	13.50
Maurolycus	41.8° S	14° E	114	1.30		1.24	17.20	17.30
Lehmann	40° S	56° W	53	1.38		1.24	14.20	11.40
Fracastorius	21.2° S	33° E	124	1.19	5.00	1.26	10.30	13.50
Region North-West of Furnerius	33.3°S	57°E	28	0.93		1.26	17.20	17.30
Rosse	17.8°S	35°E	12	1.05		1.26	10.90	11.70
Region between Proclus and Macrobius	18.2°N	46.4°E	28	1.05		1.26	17.20	17.30
Eudoxus	44.3° N	16.3° E	67	1.10	8.0	1.26	15.20	15.10
Crater East from Clavius	59°S	5°W	28	1.12		1.26	17.20	17.30
Janssen	44.96° S	40.82° E	190	1.17		1.26	13.30	16.60
Gutenberg	8.6° S	41.2° E	74	1.19		1.26	15.20	15.10
Copernicus	9.62° N	20.08° W	93	0.74	4.00	1.26	18.50	16.60
Crater North	39° S	17.2° E	28	1.39		1.26	14.20	16.60

from Mare Serenitatis								
Anaxagoras	73.48°N	10.17° W	51.9	0.74		1.29	20.20	17.30
Petavius	25.3° S	60.4° E	177	0.80		1.29	12.40	16.90
Crater, North-West from Petavius	20°S	57.5°E	5	0.80		1.29	9.70	17.30
Region between Aristoteles and Eudoxus	46.7° N	17° E	28	1.15	12.50	1.29	15.20	12.50
Mare Frigoris North-East region	56° N	28° E	28	1.09		1.29	10.90	10.90
Burg	45° N	28.2° E	40	1.14		1.29	14.20	11.40
Harpalus	52.6° N	43.4° W	39	1.16		1.29	9.30	10.20
Furnerius	36.3° S	60.4° E	125	1.25		1.29	17.20	17.30
Crater West from Timaeus	63°N	7.5°W	28	1.25		1.29	16.20	19.80
Mairan	41.6° N	43.4° W	40	1.30		1.29	15.20	14.10
Piccolomini	29.7° S	32.3° E	88	1.33		1.29	15.20	16.90
Region North of Petavius	21.3°S	62.5°E	28	1.36		1.29	9.30	14.10
Langrenus	8.9° S	60.9° E	132	1.07		1.32	8.60	16.60
Crater South from Crozier	14°S	51.5°E	12	1.08		1.32	13.30	15.10
Aristoteles	50.2° N	17.4° E	87	1.16		1.32	15.20	15.70
Crater South from Baily	48.4°N	31.3°E	12	1.19		1.32	9.60	11.70
Bianchini	48.7° N	34.3° W	38	1.21		1.32	15.20	11.70
Montes Pyrenaeus	15.6° S	41.2° E	167	1.22		1.32	12.40	16.90
Region East of Langrenus	9° S	66.5° E	28	1.37		1.32	12.40	14.10
Dzhapiashvili	7.5° N	56.5° E	48	1.20	18.0	1.32	13.30	14.1
Mare Crisium (North from	16.2° S	53.7° E	28	1.16		1.36	9.70	13.50

Picard)								
Crater North from Jacobi	53.5°S	11°E	12	1.21		1.36	16.20	16.90
Mare Fecunditatis (South region)	18°S	53°E	28	1.24		1.36	12.40	12.50
Crater East from Piccolomini	30.7°S	36°E	28	1.33		1.36	15.20	16.90
Plato	51.6° N	9.3° W	109	1.16	9.00	1.38	12.40	10.20
Crater North from Plato	55°N	8.3°W	28	1.37		1.40	15.20	13.50

In accordance with ALBEDO

Crater	Latitude	Longitude	Diameter	Polarization		Color Index [2,7]	Albedo [3,7]	m [5,7]
				min	max			
Mare Tranquillitatis	8.5° N	31.4° E	873	1.17		1.09	7.40	8.90
Oceanus Procellarum	18.4° N	57.4° W	2592	1.11		1.18	7.60	7.00
Luna 16 landing area	0.68° S	56.3° E	28	1.25		1.18	7.60	8.90
Luna 20 landing area	3.53° N	56.55° E	28	1.21		1.19	7.80	8.90
Mare Imbrium	32.8° N	15.6° W	1145	1.07		1.20	7.80	10.20
Mare Humorum	24.4° S	38.6° W	389	1.11		1.18	8.00	8.20
Crater East from Guericke	10.3°S	11°W	28	1.20		1.15	8.40	9.70
Letronne	10.6° S	42.4° W	120	1.24		1.17	8.40	8.20
Crater North from Manilius	17.5°N	11.3°E	12	1.38		1.18	8.40	10.90
Mare Serenitatis (S-W from Bessel)	19° N	17° E	28	1.12		1.19	8.40	8.90
Lambert	25.8° N	21° W	30	1.20		1.20	8.40	9.70
Mare Nubium	21.3° S	16.6° W	715	0.94		1.24	8.40	8.90

Apollo 11 landing area	0.67° N	23.47° E	28	1.20		1.13	8.60	8.90
Mare Crisium	17° N	59.1° E	555	1.07	8.80	1.19	8.60	9.70
Mare Fecunditatis	7.8°S	51.3°E	840	1.12		1.22	8.60	9.70
Langrenus	8.9° S	60.9° E	132	1.07		1.32	8.60	16.60
Luna 24 landing area	12.71°N	62.21° E	28	1.17		1.20	8.80	11.40
Messier	1.9°S	47.6°E	9 × 11	1.00		1.22	8.80	9.70
Mare Undarum	6.8° N	68.4° E	243	1.07		1.24	8.80	9.70
Reiner	7° N	54.9° W	30	1.03		1.18	9.00	8.20
Hooke	18.3°N	53.5°E	18	1.11		1.20	9.00	9.70
Marius	11.9° N	50.8° W	41	1.19		1.20	9.00	7.50
Region East of Mare Crisium	22° N	73° E	28	1.34		1.22	9.00	14.10
Bessel	21.8° N	17.9° E	16	1.11		1.18	9.30	9.70
Lansberg	0.3° S	26.6° W	39	1.12		1.19	9.30	10.90
Picard	14.57°N	54.72°E	23	1.13		1.19	9.30	9.70
Eddington	21.5° N	71.8° W	125	1.31		1.19	9.30	8.20
Billy	13.8° N	50.1 W	45	1.25		1.20	9.30	7.50
Timocharis	26.7° N	13.1° W	34.1	1.20		1.22	9.30	11.40
Crater South from Ritchey	12.3°S	9.2°E	12	1.22		1.24	9.30	12.50
Harpalus	52.6° N	43.4° W	39	1.16		1.29	9.30	10.20
Region North of Petavius	21.3°S	62.5°E	28	1.36		1.29	9.30	14.10
Crater South from Baily	48.4°N	31.3°E	12	1.19		1.32	9.60	11.70
Flamsteed	4.5° S	44.3° W	21	1.07		1.09	9.70	8.20
Seleucus	21° N	66.6° W	61	1.26		1.18	9.70	8.20
Apollo 12 landing area	3.01° S	23.42° W	28	1.05		1.19	9.70	10.90
Mare Fecunditatis (S W region)	8°S	49°E	28	1.12		1.24	9.70	9.70

Mare Nectaris	15.2° S	34.6° E	340	1.22	7.60	1.24	9.70	11.40
Crater, North-West from Petavius	20°S	57.5°E	5	0.80		1.29	9.70	17.30
Mare Crisium (North from Picard)	16.2° S	53.7° E	28	1.16		1.36	9.70	13.50
Archimedes	29.7° N	4° W	83	1.20	9.10	1.20	10.30	10.20
Fracastorius	21.2° S	33° E	124	1.19	5.00	1.26	10.30	13.50
Sinus Medii	2.4° N	1.7° E	335	1.23		1.18	10.90	11.70
Rosse	17.8°S	35°E	12	1.05		1.26	10.90	11.70
Mare Frigoris North-East region	56° N	28° E	28	1.09		1.29	10.90	10.90
Apollo 17 landing area	20.19°N	30.77° E	28	1.14		1.18	11.60	11.40
Apollo 14 landing area	3.64° S	17.47° W	28	1.10		1.19	11.60	12.50
Aristillus	33.7°N	1°E	55	1.11	8.90	1.19	11.60	11.70
Eratosthenes	14.47° N	11.32° W	59	1.00		1.20	11.60	11.40
Vaisala	25.9° N	47.8° W	8	1.01		1.20	11.60	12.50
Pitatus	29.8° S	13.5° W	34.1	1.18		1.20	11.60	10.20
Plinius	15.4° N	23.7° E	43	1.05		1.06	12.40	11.40
Mare Serenitatis	28° N	17.5° E	674	1.32		1.10	12.40	9.70
Creter1 Weast from Alfraganus	1.7° S	19.3° E	28	0.92		1.15	12.40	13.50
Dionysius	2.8° N	17.3° E	18	0.86		1.19	12.40	12.50
Endymion	53.6° N	56.5° E	125	0.93		1.19	12.40	14.10
Bullialdus	20.7° S	22.2° W	61	1.13		1.19	12.40	12.50
Aristarchus	23.7° N	47.4° W	40	0.66		1.19	12.40	13.50
Mare Imbrium (North from Autolycus)	32° N	1.3° E	28	1.16		1.20	12.40	12.50
Apollo 16 landing area	8.97° S	15.5° E	28	1.16		1.20	12.40	12.50

Cleomedes	27.7° N	55.5° E	126	1.14		1.21	12.40	12.50
Proclus	16.1° N	46.8° E	28	0.62	5.20	1.22	12.40	15.70
Posidonius	31.8° N	29.9° E	95	1.09	5.20	1.22	12.40	13.50
Autolycus	30.7° N	1.5° E	39	1.20	9.0	1.22	12.40	11.40
Montes Apenninus	18.9° N	3.7° W	5,4	1.31		1.22	12.40	13.50
Alpetragius	16° S	4.5° W	40	1.00		1.24	12.40	12.50
Euler	23.3° N	29.2° W	28	1.21		1.24	12.40	10.20
Petavius	25.3° S	60.4° E	177	0.80		1.29	12.40	16.90
Montes Pyrenaeus	15.6° S	41.2° E	167	1.22		1.32	12.40	16.90
Region East of Langrenus	9° S	66.5° E	28	1.37		1.32	12.40	14.10
Mare Fecunditatis (South region)	18°S	53°E	28	1.24		1.36	12.40	12.50
Plato	51.6° N	9.3° W	109	1.16	9.00	1.38	12.40	10.20
Mare Frigoris	56° N	1.4° E	1446	1.30		1.18	13.30	13.50
Reinhold	3.3° N	22.8° W	48	1.21		1.19	13.30	10.90
Ptolemaeus	9.2° S	1.8° W	153	1.17	9.30	1.21	13.30	12.50
Fra Mauro	6° S	17° W	95	1.07		1.22	13.30	12.50
Purbach	25.5° S	1.9° W	118	1.16		1.22	13.30	13.50
Hercules	46.7° N	39.1° E	69	0.88		1.24	13.30	13.50
Janssen	44.96° S	40.82° E	190	1.17		1.26	13.30	16.60
Dzhapiashvili	7.5° N	56.5° E	48	1.20	18.0	1.32	13.30	14.1
Crater South from Crozier	14°S	51.5°E	12	1.08		1.32	13.30	15.10
Region East of Endymion	56° N	63° E	28	1.27		1.17	14.20	14.20
Menelaus	16.3°N	16° E	27	1.01		1.19	14.20	13.50
Messala	39.2° N	59.9° E	125	1.08		1.19	14.20	15.10
T. Mayer	15.6° N	29.1° W	33	1.12		1.20	14.20	11.40
Arzachel	18.2° S	1.9° W	96	1.10		1.24	14.20	15.70
Alphonsus	13.4° S	2.8° W	119	1.11	6.60	1.24	14.20	14.10

Bonpland	8.3° S	17.4° W	60	1.30		1.24	14.20	13.50
Lehmann	40° S	56° W	53	1.38		1.24	14.20	11.40
Crater North from Mare Serenitatis	39° S	17.2° E	28	1.39		1.26	14.20	16.60
Burg	45° N	28.2° E	40	1.14		1.29	14.20	11.40
Ross	11.7° N	21.7° E	24	1.28		1.09	15.20	7.50
Pickering	2.88° S	6.99° E	15	1.00		1.17	15.20	15.70
Geminus	31.5° N	56.7° E	86	1.16		1.17	15.20	15.20
Godin	1.8° N	10.2° E	35	0.97		1.19	15.20	15.70
Grimaldi	5.2° S	68.6° W	173.49	1.30		1.19	15.20	8.90
Crater North from Hind	7.3°S	8.3°E	5	0.96		1.20	15.20	14.10
Manilius	14.5° N	9.1° E	39	1.10		1.21	15.20	13.50
Tycho	43.31° S	11.36° W	86	0.60	9.00	1.22	15.20	18.60
Macrobius	21.3° N	46.0° E	64	1.05		1.22	15.20	13.50
Herodotus	23.2° N	49.7° W	35	1.05		1.22	15.20	11.40
Crater East from Horrocks	4.0°S	7.5°E	5	1.16		1.22	15.20	14.10
Crater North-East from Horrocks	3.0°S	7.0°E	5	1.18		1.22	15.20	15.70
Hooke	41.2° N	54.9° E	139	1.32		1.22	15.20	15.70
Eudoxus	44.3° N	16.3° E	67	1.10	8.0	1.26	15.20	15.10
Gutenberg	8.6° S	41.2° E	74	1.19		1.26	15.20	15.10
Region between Aristoteles and Eudoxus	46.7° N	17° E	28	1.15	12.50	1.29	15.20	12.50
Mairan	41.6° N	43.4° W	40	1.30		1.29	15.20	14.10
Piccolomini	29.7° S	32.3° E	88	1.33		1.29	15.20	16.90
Aristoteles	50.2° N	17.4° E	87	1.16		1.32	15.20	15.70
Bianchini	48.7° N	34.3° W	38	1.21		1.32	15.20	11.70
Crater East from Piccolomini	30.7°S	36°E	28	1.33		1.36	15.20	16.90

Crater North from Plato	55°N	8.3°W	28	1.37		1.40	15.20	13.50
Apollo 15 landing area	26.13° N	3.63° E	12	1.11		1.20	16.20	8.90
Schickard	44.4° S	54.6° W	227	1.19		1.24	16.20	10.20
Crater West from Timaeus	63°N	7.5°W	28	1.25		1.29	16.20	19.80
Crater North from Jacobi	53.5°S	11°E	12	1.21		1.36	16.20	16.90
Theophilus	11.4° S	26.4° E	100	0.82	4.70	1.11	17.20	17.30
Triesnecker	4.18° N	3.6° E	26	1.06		1.17	17.20	14.10
Creter2 Weast from Alfraganus	6° S	18.3° E	28	0.92		1.19	17.20	18.60
Catharina	18° S	23.6° E	100	1.01	4.20	1.22	17.20	17.30
Creter Weast from Theophilus	10.5° S	23.5° E	28	1.01		1.22	17.20	15.70
Kepler	8.1° N	38° W	32	0.85	3.90	1.22	17.20	11.70
Maurolycus	41.8° S	14° E	114	1.30		1.24	17.20	17.30
Region North-West of Furnerius	33.3°S	57°E	28	0.93		1.26	17.20	17.30
Region between Proclus and Macrobius	18.2°N	46.4°E	28	1.05		1.26	17.20	17.30
Crater East from Clavius	59°S	5°W	28	1.12		1.26	17.20	17.30
Furnerius	36.3° S	60.4° E	125	1.25		1.29	17.20	17.30
Cyrillus	13.2° S	24° E	98	0.85	3.80	1.11	18.50	19.80
Creter Weast from Cyrillus	11.5° S	21.8° E	28	0.80		1.20	18.50	18.60
Crater North from Tycho	41.5°S	10°W	12	0.75		1.22	18.50	9.70
Meton	73.8° N	19.2° E	122	1.16		1.22	18.50	16.90
Clavius	58.4° S	14.4° W	231	1.01		1.24	18.50	19.80
Crater North-West from Tycho	38.3°S	16°W	12	1.08		1.24	18.50	15.70

Crater North-East from Maginus	48.7°S	1.5°W	12	1.19		1.24	18.50	19.80
Copernicus	9.62° N	20.08° W	93	0.74	4.00	1.26	18.50	16.60
Crater North from Tycho	39.5°S	7°W	12	0.94		1.20	20.20	17.30
Scoresby	77.7° N	14.1° E	56	0.97		1.22	20.20	16.90
Crater South from Tycho	46°S	11.5°W	12	0.86		1.24	20.20	16.90
Crater North-West from Tycho	36°S	15°W	12	1.08		1.24	20.20	16.90
Anaxagoras	73.48° N	10.17° W	51.9	0.74		1.29	20.20	17.30
Crater South from Deslandres	37°S	4°W	12	1.03		1.20	23.20	18.60

In accordance with m

Crater	Latitude	Longitude	Diameter	Polarization		Color Index [2,7]	Albedo [3,7]	m [5,7]
				min	max			
Oceanus Procellarum	18.4° N	57.4° W	2592	1.11		1.18	7.60	7.00
Marius	11.9° N	50.8° W	41	1.19		1.20	9.00	7.50
Billy	13.8° N	50.1 W	45	1.25		1.20	9.30	7.50
Ross	11.7° N	21.7° E	24	1.28		1.09	15.20	7.50
Mare Humorum	24.4° S	38.6° W	389	1.11		1.18	8.00	8.20
Letronne	10.6° S	42.4° W	120	1.24		1.17	8.40	8.20
Reiner	7° N	54.9° W	30	1.03		1.18	9.00	8.20
Eddington	21.5° N	71.8° W	125	1.31		1.19	9.30	8.20

Flamsteed	4.5° S	44.3° W	21	1.07		1.09	9.70	8.20
Seleucus	21° N	66.6° W	61	1.26		1.18	9.70	8.20
Mare Tranquillitatis	8.5° N	31.4° E	873	1.17		1.09	7.40	8.90
Luna 16 landing area	0.68° S	56.3° E	28	1.25		1.18	7.60	8.90
Luna 20 landing area	3.53° N	56.55° E	28	1.21		1.19	7.80	8.90
Mare Serenitatis (S-W from Bessel)	19° N	17° E	28	1.12		1.19	8.40	8.90
Mare Nubium	21.3° S	16.6° W	715	0.94		1.24	8.40	8.90
Apollo 11 landing area	0.67° N	23.47° E	28	1.20		1.13	8.60	8.90
Grimaldi	5.2° S	68.6° W	173.49	1.30		1.19	15.20	8.90
Apollo 15 landing area	26.13° N	3.63° E	12	1.11		1.20	16.20	8.90
Crater East from Guericke	10.3°S	11°W	28	1.20		1.15	8.40	9.70
Lambert	25.8° N	21° W	30	1.20		1.20	8.40	9.70
Mare Crisium	17° N	59.1° E	555	1.07	8.80	1.19	8.60	9.70
Mare Fecunditatis	7.8°S	51.3°E	840	1.12		1.22	8.60	9.70
Messier	1.9°S	47.6°E	9 × 11	1.00		1.22	8.80	9.70
Mare Undarum	6.8° N	68.4° E	243	1.07		1.24	8.80	9.70
Hooke	18.3°N	53.5°E	18	1.11		1.20	9.00	9.70
Bessel	21.8° N	17.9° E	16	1.11		1.18	9.30	9.70
Picard	14.57°	54.72°E	23	1.1		1.19	9.30	9.70

	N			3				
Mare Fecunditatis (S W region)	8°S	49°E	28	1.12		1.24	9.70	9.70
Mare Serenitatis	28° N	17.5° E	674	1.32		1.10	12.40	9.70
Crater North from Tycho	41.5°S	10°W	12	0.75		1.22	18.50	9.70
Mare Imbrium	32.8° N	15.6° W	1145	1.07		1.20	7.80	10.20
Harpalus	52.6° N	43.4° W	39	1.16		1.29	9.30	10.20
Archimedes	29.7° N	4° W	83	1.20	9.10	1.20	10.30	10.20
Pitatus	29.8° S	13.5° W	34.1	1.18		1.20	11.60	10.20
Euler	23.3° N	29.2° W	28	1.21		1.24	12.40	10.20
Plato	51.6° N	9.3° W	109	1.16	9.00	1.38	12.40	10.20
Schickard	44.4° S	54.6° W	227	1.19		1.24	16.20	10.20
Crater North from Manilius	17.5°N	11.3°E	12	1.38		1.18	8.40	10.90
Lansberg	0.3° S	26.6° W	39	1.12		1.19	9.30	10.90
Apollo 12 landing area	3.01° S	23.42° W	28	1.05		1.19	9.70	10.90
Mare Frigoris North-East region	56° N	28° E	28	1.09		1.29	10.90	10.90
Reinhold	3.3° N	22.8° W	48	1.21		1.19	13.30	10.90
Luna 24 landing area	12.71° N	62.21° E	28	1.17		1.20	8.80	11.40
Timocharis	26.7° N	13.1° W	34.1	1.20		1.22	9.30	11.40
Mare Nectaris	15.2° S	34.6° E	340	1.22	7.60	1.24	9.70	11.40

Apollo 17 landing area	20.19° N	30.77° E	28	1.14		1.18	11.60	11.40
Eratosthenes	14.47° N	11.32° W	59	1.00		1.20	11.60	11.40
Plinius	15.4° N	23.7° E	43	1.05		1.06	12.40	11.40
Autolycus	30.7° N	1.5° E	39	1.20	9.0	1.22	12.40	11.40
T. Mayer	15.6° N	29.1° W	33	1.12		1.20	14.20	11.40
Lehmann	40° S	56° W	53	1.38		1.24	14.20	11.40
Burg	45° N	28.2° E	40	1.14		1.29	14.20	11.40
Herodotus	23.2° N	49.7° W	35	1.05		1.22	15.20	11.40
Crater South from Baily	48.4°N	31.3°E	12	1.19		1.32	9.60	11.70
Sinus Medii	2.4° N	1.7° E	335	1.23		1.18	10.90	11.70
Rosse	17.8°S	35°E	12	1.05		1.26	10.90	11.70
Aristillus	33.7°N	1°E	55	1.11	8.90	1.19	11.60	11.70
Bianchini	48.7° N	34.3° W	38	1.21		1.32	15.20	11.70
Kepler	8.1° N	38° W	32	0.85	3.90	1.22	17.20	11.70
Crater South from Ritchey	12.3°S	9.2°E	12	1.22		1.24	9.30	12.50
Apollo 14 landing area	3.64° S	17.47° W	28	1.10		1.19	11.60	12.50
Vaisala	25.9° N	47.8° W	8	1.01		1.20	11.60	12.50
Dionysius	2.8° N	17.3° E	18	0.86		1.19	12.40	12.50
Bullialdus	20.7° S	22.2° W	61	1.13		1.19	12.40	12.50

Mare Imbrium (North from Autolycus)	32° N	1.3° E	28	1.16		1.20	12.40	12.50
Apollo 16 landing area	8.97° S	15.5° E	28	1.16		1.20	12.40	12.50
Cleomedes	27.7° N	55.5° E	126	1.14		1.21	12.40	12.50
Alpetragius	16° S	4.5° W	40	1.00		1.24	12.40	12.50
Mare Fecunditatis (South region)	18°S	53°E	28	1.24		1.36	12.40	12.50
Ptolemaeus	9.2° S	1.8° W	153	1.17	9.30	1.21	13.30	12.50
Fra Mauro	6° S	17° W	95	1.07		1.22	13.30	12.50
Region between Aristoteles and Eudoxus	46.7° N	17° E	28	1.15	12.50	1.29	15.20	12.50
Mare Crisium (North from Picard)	16.2° S	53.7° E	28	1.16		1.36	9.70	13.50
Fracastorius	21.2° S	33° E	124	1.19	5.00	1.26	10.30	13.50
Creter1 Weast from Alfraganus	1.7° S	19.3° E	28	0.92		1.15	12.40	13.50
Aristarchus	23.7° N	47.4° W	40	0.66		1.19	12.40	13.50
Posidonius	31.8° N	29.9° E	95	1.09	5.20	1.22	12.40	13.50
Montes Apenninus	18.9° N	3.7° W	5400 metres	1.31		1.22	12.40	13.50
Mare Frigoris	56° N	1.4° E	1446	1.30		1.18	13.30	13.50
Purbach	25.5° S	1.9° W	118	1.16		1.22	13.30	13.50
Hercules	46.7° N	39.1° E	69	0.88		1.24	13.30	13.50
Menelaus	16.3°N	16° E	27	1.0		1.19	14.20	13.5

				1				0
Bonpland	8.3° S	17.4° W	60	1.30		1.24	14.20	13.50
Manilius	14.5° N	9.1° E	39	1.10		1.21	15.20	13.50
Macrobius	21.3° N	46.0° E	64	1.05		1.22	15.20	13.50
Crater North from Plato	55°N	8.3°W	28	1.37		1.40	15.20	13.50
Dzhapiashvili	7.5° N	56.5° E	48	1.20	18.0	1.32	13.30	14.1
Region East of Mare Crisium	22° N	73° E	28	1.34		1.22	9.00	14.10
Region North of Petavius	21.3°S	62.5°E	28	1.36		1.29	9.30	14.10
Endymion	53.6° N	56.5° E	125	0.93		1.19	12.40	14.10
Region East of Langrenus	9° S	66.5° E	28	1.37		1.32	12.40	14.10
Alphonsus	13.4° S	2.8° W	119	1.11	6.60	1.24	14.20	14.10
Crater North from Hind	7.3°S	8.3°E	5	0.96		1.20	15.20	14.10
Crater East from Horrocks	4.0°S	7.5°E	5	1.16		1.22	15.20	14.10
Mairan	41.6° N	43.4° W	40	1.30		1.29	15.20	14.10
Triesnecker	4.18° N	3.6° E	26	1.06		1.17	17.20	14.10
Region East of Endymion	56° N	63° E	28	1.27		1.17	14.20	14.20
Crater South from Crozier	14°S	51.5°E	12	1.08		1.32	13.30	15.10
Messala	39.2° N	59.9° E	125	1.08		1.19	14.20	15.10
Eudoxus	44.3° N	16.3° E	67	1.10	8.0	1.26	15.20	15.10
Gutenberg	8.6° S	41.2° E	74	1.1		1.26	15.20	15.1

				9				0
Geminus	31.5° N	56.7° E	86	1.16		1.17	15.20	15.20
Proclus	16.1° N	46.8° E	28	0.62	5.20	1.22	12.40	15.70
Arzachel	18.2° S	1.9° W	96	1.10		1.24	14.20	15.70
Pickering	2.88° S	6.99° E	15	1.00		1.17	15.20	15.70
Godin	1.8° N	10.2° E	35	0.97		1.19	15.20	15.70
Crater North-East from Horrocks	3.0°S	7.0°E	5	1.18		1.22	15.20	15.70
Hooke	41.2° N	54.9° E	139	1.32		1.22	15.20	15.70
Aristoteles	50.2° N	17.4° E	87	1.16		1.32	15.20	15.70
Creter Weast from Theophilus	10.5° S	23.5° E	28	1.01		1.22	17.20	15.70
Crater North-West from Tycho	38.3°S	16°W	12	1.08		1.24	18.50	15.70
Langrenus	8.9° S	60.9° E	132	1.07		1.32	8.60	16.60
Janssen	44.96° S	40.82° E	190	1.17		1.26	13.30	16.60
Crater North from Mare Serenitatis	39° S	17.2° E	28	1.39		1.26	14.20	16.60
Copernicus	9.62° N	20.08° W	93	0.74	4.00	1.26	18.50	16.60
Petavius	25.3° S	60.4° E	177	0.80		1.29	12.40	16.90
Montes Pyrenaeus	15.6° S	41.2° E	167	1.22		1.32	12.40	16.90
Piccolomini	29.7° S	32.3° E	88	1.33		1.29	15.20	16.90
Crater East from	30.7°S	36°E	28	1.3		1.36	15.20	16.9

Piccolomini				3				0
Crater North from Jacobi	53.5°S	11°E	12	1.21		1.36	16.20	16.90
Meton	73.8° N	19.2° E	122	1.16		1.22	18.50	16.90
Scoresby	77.7° N	14.1° E	56	0.97		1.22	20.20	16.90
Crater South from Tycho	46°S	11.5°W	12	0.86		1.24	20.20	16.90
Crater North-West from Tycho	36°S	15°W	12	1.08		1.24	20.20	16.90
Crater, North-West from Petavius	20°S	57.5°E	5	0.80		1.29	9.70	17.30
Theophilus	11.4° S	26.4° E	100	0.82	4.70	1.11	17.20	17.30
Catharina	18° S	23.6° E	100	1.01	4.20	1.22	17.20	17.30
Maurolycus	41.8° S	14° E	114	1.30		1.24	17.20	17.30
Region North-West of Furnerius	33.3°S	57°E	28	0.93		1.26	17.20	17.30
Region between Proclus and Macrobius	18.2°N	46.4°E	28	1.05		1.26	17.20	17.30
Crater East from Clavius	59°S	5°W	28	1.12		1.26	17.20	17.30
Furnerius	36.3° S	60.4° E	125	1.25		1.29	17.20	17.30
Crater North from Tycho	39.5°S	7°W	12	0.94		1.20	20.20	17.30
Anaxagoras	73.48° N	10.17° W	51.9	0.74		1.29	20.20	17.30
Tycho	43.31° S	11.36° W	86	0.60	9.00	1.22	15.20	18.60
Creter2 Weast from Alfraganus	6° S	18.3° E	28	0.92		1.19	17.20	18.60

Creter Weast from Cyrillus	11.5° S	21.8° E	28	0.80		1.20	18.50	18.60
Crater South from Deslandres	37°S	4°W	12	1.03		1.20	23.20	18.60
Crater West from Timaeus	63°N	7.5°W	28	1.25		1.29	16.20	19.80
Cyrillus	13.2° S	24° E	98	0.85	3.80	1.11	18.50	19.80
Clavius	58.4° S	14.4° W	231	1.01		1.24	18.50	19.80
Crater North-East from Maginus	48.7°S	1.5°W	12	1.19		1.24	18.50	19.80

2. We found a program to search for similar craters (Prof.M. Mdivani).

 # When Confidence Probability the Equally 0.98

Mare Imbrium (North from Autolycus) similar Apollo 16 landing area

Bessel – Picard

 # When Confidence Probability the Equally 0.97

Picard – Hooke

Bessel – Picard

Mare Imbrium (North from Autolycus) - Apollo 16 landing area

 # When Confidence Probability the Equally 0.96

Mare Fecunditatis – Hooke

Bessel – Hooke

Picard – Hooke

Bessel – Picard

Aristillus - Apollo 17 landing area

Bullialdus – Cleomedes

Cleomedes - Mare Imbrium (North from Autolycus)

Cleomedes - Apollo 16 landing area

Mare Imbrium (North from Autolycus) - Apollo 16 landing area

Mare Nectaris – Timocharis

 # When Confidence Probability the Equally 0.95

Crater North-West from Tycho – Scoresby

Godin – Pickering

Catharina - Region between Proclus and Macrobius

Mare Undarum – Hooke

Mare Crisium – Hooke

Mare Fecunditatis – Hooke

Bessel – Hooke

Picard – Hooke

Bessel – Picard

Aristillus - Apollo 17 landing area

Lansberg - Luna 24 landing area

Bullialdus – Cleomedes

Bullialdus - Apollo 16 landing area

Bullialdus - Mare Imbrium (North from Autolycus)

Cleomedes - Mare Imbrium (North from Autolycus)

Cleomedes - Apollo 16 landing area

Mare Imbrium (North from Autolycus) - Apollo 16 landing area

Luna 24 landing area – Timocharis

Mare Nectaris – Timocharis

Luna 20 landing area - Luna 16 landing area

 # When Confidence Probability the Equally 0.93

Creter2 Weast from Alfraganus - Endymion

Crater North-West from Tycho – Scoresby

Godin – Pickering

Catharina - Region between Proclus and Macrobius

Roose - Mare Frigoris North-East region

Mare Undarum – Hooke

Mare Crisium – Hooke

Mare Fecunditatis – Hooke

Picard – Hooke

Mare Serenitatis (S-W from Bessel) – Hooke

Mare Fecunditatis (S W region) – Hooke

Bessel – Hooke

Bessel - Mare Crisium

Bessel – Picard

Bessel – Mare Fecunditatis

Mare Serenitatis (S-W from Bessel) - Mare Fecunditatis

Mare Serenitatis (S-W from Bessel) - Mare Humorum

Picard - Mare Humorum

Aristillus - Apollo 17 landing area

Lansberg - Luna 24 landing area

Bullialdus – Cleomedes

Bullialdus - Apollo 16 landing area

Bullialdus - Mare Imbrium (North from Autolycus)

Cleomedes - Mare Imbrium (North from Autolycus)

Cleomedes - Apollo 16 landing area

Mare Imbrium (North from Autolycus) - Apollo 16 landing area

Luna 24 landing area – Timocharis

Crater North-East from Horrocks – Gutenberg

Apollo 11 landing area – Crater East from Guericke

Apollo 11 landing area - Letronne

Crater East from Guericke - Luna 20 landing area

Lansberg - Luna 20 landing area

Mare Nectaris – Timocharis

Luna 20 landing area - Luna 16 landing area

Luna 20 landing area – Letronne

Billy – Seleucus

Dzhapiashvili - Purbach

And so on …

Based on laboratory measurements:

1. A conclusion is drawn that Pmin can be used as indicator of plutonic deposits [1,7,8,9,11]

Regarding this:

Highest content they: Crater North from Manilius, Lehmann, Crater North from Mare Serenitatis.

Lowest content They: Tycho, Proclus , Aristarchus.

2. A conclusion is drawn that Pmax can be used as indicator of ($FeO - TiO_2$). [6,7,8].

Regarding this:

Highest content they: Mare Nectaris , Dzhapiashvili, Mare Crisium.

Lowest content They : Proclus, Tycho, Catharina.

3. A conclusion is drawn that Color index can be used as indicator of ($MgO - TiO_2$) [6,7,10].

Regarding this:

Highest content they: Crater East from Piccolomini,Plato. Crater North from Plato.

Lowest content They: Plinius, Flamsteed, Mare Tranquillitatis.

4. A conclusion is drawn that Albedo can be used as indicator of (SiO_2 - Al_2O_3). [7,10].

Regarding this:

Highest content they: Crater North-West from Tycho, Anaxagoras, Crater South from Deslandres.

Lowest content They: Mare Tranquillitatis, Oceanus Procellarum, Luna 16 landing area.

References

1.Kvaratskhelia O., The distribution of negative polarization minima for separate Regions of the Lunar Surface. Biulletin Abasstumani Astropysical Observatory, 1986, 61, pp. 101-108

2. EvsjukovN ., Moon map Colourindexs, Kiev ,p. 1. 1973

3. Evsjukov N., Moon map Albedo, Kiev, p. 1. 1973

4. Dzhapiashvili, V., Korol, A., "Polarimetricheskii atlas luny", "Tbilisi: "Metsniereba", 1978., p. 44

5. Evsjukov N., Moon map Albedo(Pot.), Kiev, p. 1. 1973

6. Dolffus A, Icarus., 1975. 25, 416

7. ShkuratovYu.G., Moon. Kharkov, pp. 182, 2006

8. Kvaratskhelia O., Dissertation Thesis. Abastumani, 2006., 219

9. Kvaratskhelia O., International Scientific Conference ,,Problems of Modern Astrophysics" report ,,Spectropolarimetry of the Moon". Akhaltsikhe. 2015

10. Evsjukov N., Surkov Ju., Cnumak E., Astron. vest. 1991, 25, pp. 34-44

11. Kvaratskhelia O., Ivanidze R., Gigolashvili Sh., Spectropolarimetry of the Lunar Surface and Its Ground Samples. Astronomy & Astrophysics (Caucasus)1, 2016, pp. 49-52.

Data: Latitude, Longitude, Diameter, Moon fragment of taken

https://en.wikipedia.org/wiki/List_of_craters_on_the_Moon

https://en.wikipedia.org/wiki/List_of_maria_on_the_Moon

.

Key words

Albedo

Astronomical cycles

Color Index

Front and rear hemispheres

Formation of spectral lines

Galilean satellites

Jupiter

Lightcurve

Microturbulent velocity

Minor planet

Molecular hydrogen

Moon

Ortho- para-hydrogen

Photometry

Polarization

Polarization degree

Quadrupole lines

Rotational period

Saturn

Self-organized criticality

Solar prominences::

Surface colors

Synchronization

Tide

Author Index for Volume 4

Astronomy & Astrophysics (Caucasus)
Scientific paper Submission

The submitted article's technical parameters are the same as in the USA leading international scientific journals.After the positive review only astronomy and astrophysical original articles will be published in this journal.

The manuscript should be presented in A4 format. The size of the article ,including bibliography and other types of enclosure should not exceed 20 pages printed with 1interval and 12 sized font.

It is possible to submit the online version of the manuscript but is should be written only in English. (Text must be typed in Times New Roman, MS word or Pdf file)

The text should be written on the whole page and not separately on twocolumns,the same as in this journal.

Structure of the paper:

Title of the paper:

Author/authors:

Name of the author/authors,firstname,secondname, working place,country and online address must be presented below the manuscript title.

Abstract

The abstract must be informative.Shouldrepresent the content of the paper,describe the goal of the research,symmerize results of the survey and show its theoretical and practical importance.The abstract should not exceed more than 250words,nearly one page.

Key words: Authors should provide key words,which are relevant to the topic.Maxium amount of the words should be 8 . Use only commonly used shortenings .

Introduction: Authors should highlight the essence of the problem, their sub-aims,what is their hypothesis,importance of their paper and what have been done peviously in this field.

Methods: The article should be build methodologically correct way. It should reflect the usage of modern research methods.

Results: Results must be described clearly and briefly**.** Each illustration should have its inscription**.** Number the tables used in the text consistently.

Analysis: This paragraph should investigate the importance of the paper results.You should compare your result to the previous ones**.**

Conclusions: The main conclusion can be written in this paragraph**.**

Acknowledgment: At the end of the paper on the separate chapter you should express your gratitute to those people who helped you during the research.

Literature citation: Consider that every source you have used in this paper is also indicated in the bibliography or vice versa.

Sources Reference Style: The literature quoted in the scientific publication should be indicated with round brackets.(Sort version:name of the author and the rule of the article publication**.**

Reference: Nominated literature where the author's identity is indicated fully,the date of the publication and appropriate page should be arranged alphabetically.

It will be published twice in a year.

The paper should be send to the following e-mail address: astronomy@sjuni.edu.ge

CONTENTS

Publishing Groupi: **L. Gurgenidze**

L. Zedginidze

Correctional: **T. Dolidze**

SAMTSKHE-JAVAKHETI STATE

UNIVERSITY PRESS

Akhaltsike, Rustaveli Street #113

Tel.: 0(365)22-19-90, 591-41-12-78

E-mail: astronomy@sjuni.edu.ge